Achieving Single-Molecule Tracking in Bacteria During Real-Time Environmental Perturbations

by

Anna L. Calkins

A dissertation submitted in partial fulfillment
of the requirements for the degree of
Doctor of Philosophy
(Chemistry)
in The University of Michigan
2023

Doctoral Committee:

       Professor Julie S. Biteen, Chair
       Professor Ryan Bailey
       Professor Robert Kennedy
       Professor Maria Sandkvist

Anna L. Calkins

annalc@umich.edu

ORCID iD: 0000-0003-0130-296X

To my Dad, for everything you gave me.

ACKNOWLEDGEMENTS

Getting a Ph.D. was not something I dreamed about doing forever and certainly was not something I felt capable of doing. So, I think my first acknowledgement has to go three professors who convinced me I was capable and maybe even a good candidate for graduate school, Dr. Grace Stokes, Dr. Amelia Fuller, and Dr. Steven Suljak. Dr. Stokes, thank you for taking a chance on a overly excited sophomore TA to start your research lab. I will always be grateful for the time and energy you spent teaching me how to align a laser, write a research paper, and be an engaged, thoughtful, and collaborative scientist. Dr. Fuller, thank you for giving me my first job in science and giving me a safe space to get back on my feet and figure out what comes next. I was so prepared for graduate school because of the lessons you provided me while working in your labs. Dr. Suljak, thank you for introducing me to analytical chemistry. At the time, I did not know it was what I really wanted to study, but I do remember your class felt like a breath of fresh air in a sea of losing my place in science. Thank you for letting me pretend to be in your lab at my first ACS and always being supportive of continuing my education. While I am thanking teachers, I need to acknowledge Mr. Feebeck my first chemistry teacher who made the subject so fascinating and easy to learn. Thank you for encouraging me to pursue my interests, creating such an engaging class, and giving me excellent lab skills to jump off of.

During my Ph.D., I had the privilege of being guided by Professor Julie Biteen. Julie thank you for willingly jumping into the world of microfluidics with me, always asking me how I am doing before starting a meeting, and never letting me give up. I will forever

be grateful to have a boss who so deeply cares about me and is somehow more organized than I am. I also spent 5 years learning from lab mates around me and am grateful for the positive atmosphere in the Biteen lab. Stephen, Josh, Curly and Laurent, thank you for laying the groundwork for my endless microscopy education. Hannah and Aathmaja, thank you for answering every silly biology question I had and creating joy inside and outside the lab. Kate, David, Xiaofeng, Luis, and Dan thank you for making the hard lab days more fun and continuing the positive lab environment. Brooke, thank you for jumping into a brand new project with me and working hard to lay the ground work that became my dissertation. Lauren, Zechariah, Ziyuan, and Chris, thank you for your feedback, answers to every question under the sun, code and coding help, and Friday night happy hours throughout my time at Michigan.

Thank you to my committee: Professor Robert Kennedy who allowed me to rotate in his lab and learn all of the microfluidics fundamentals, Professor Maria Sandkvist for being interested in jumping on board at the last minute, Professor Kaushik Ragunathan for giving excellent biological feedback, and Professor Ryan Bailey for brainstorming about microfluidics and giving me access to his lab clean room without hesitation making much of my research possible. Thank you to Claire Cook, Dr. Emory Payne, Ashley Lenhart, Dr. Nico Mesyngier, Dr. Gloria Diaz, Dr. Saikat Biswas, and Dr. Jeremy Schroeder for your time, training, and willingness to answer all of my microfluidics questions. Thank you to Dr. Jorge Barreda, Shawn Wright, Kevin Owen, and Dr. Vishva Ray at the Lurie Nanofabrication facility for training me and continuing to brainstorm fabrication fixes when everything seemed to go wrong. Thank you to Professor Victor DiRita and Dr. Lucas Demy for your commitment to this collaboration and biological support. Lucas it was a pleasure working with you for so many years. Thank you to the many other microbiology collaborators I have worked with including Professor Joanna Slusky, Dr. Jimmy Budiardjo, Professor Anne Meyer, Professor Elio Abbondanzieri, and Professor Xindan Wang. As well as Dr. Lauren McCarthy who worked tirelessly over the past 6 months to get this last Dps

project off the ground.

I would not have survived my time here without the friendships I made outside of the lab. Claire and Ashley, thank you for 5 years of apple picking, game nights, tea, and friendship. I cannot wait to see what you all do next and so excited to be right there next to you. Kayla and Ruby, thank you for making a pandemic easier. I will never forget the two years we spent at sylvan house and all the campfires, family photos, and attempts to escape. Also, thank you to David, Tyler, Emory, Peter, Brady, Marina, and Josh for making the past 5 years more than just work.

My oldest friend Erin was never a scientist, but has spent many hours listening to me talk on and on about it. Thank you for always being there, hopping on a plane just to see me, and being the power to my brains even though you have plenty of your own. I am so grateful to have you walk with me this far and can't wait to see where we go next even if it continues to be across the country! Elizabeth Tidwell, I truly wouldn't be here without you. I am constantly in awe of your empathy, ability to love, and love of learning. I am forever grateful to a universe that brought us together and every day since. Thank you for your daily encouragement, hugs, fun facts, crazy stories, and being the best roommate ever!

Finally, I need to acknowledge the people who started this all, my parents. My mom is not here to witness this compilation of a lifetime of curiosity and hard work, but I know she would be proud of me. She worked so hard to make sure I had an excellent education and I would not be here without every piece of it. Thank you for leading my girl scout troops, enrolling me in every science camp you found, and being more excited about college then I was. I dedicated this dissertation to my Dad because he is the person who taught me to be curious. Thank you for every second you spent playing with dolls, camping in the pouring rain and snow fields, taking me to every museum, and not just answering my questions, but showing me how to answer them myself. This is for you!

TABLE OF CONTENTS

LIST OF FIGURES

LIST OF TABLES

Table

LIST OF ABBREVIATIONS

B. subtilis *Bacillus subtilis*

B. theta *Bacteroides thetaiotaomicron*

CtxAB cholera toxin

Cy3 Cyanine3

DMSO Dimethyl sulfoxide

Dps DNA-binding Protein from Starved cells

Dps-PAmC Dps-PAmCherry

dpspro *dps* promoter

DTT Dithiothreitol

E. coli *Escherichia coli*

EDTA Ethylenediaminetetraacetic acid

EMCCD electron multiplying charged-couple detector

GFP Green Fluorescent Protein

HDA Hi-Def Azure

HDMS hexamethyldisilizane

H$_2$O$_2$ hydrogen peroxide

IPA isopropanol

IPTG isopropyl-β-D-thiogalactopyranoside

K. pneumoniae *Klebsiella pneumoniae*

LB lysogeny broth

LNF Lurie Nanofabrication Facility

MLTAs membrane-localized transcription activators

MSD mean squared displacement

NA numerical aperture

OMPs Outer Membrane Proteins

PALM Photoactivated Localization Microscopy

PAmC PhotoActivatable mCherry

PBS phosphate buffer saline

PDMS Polydimethylsiloxane

PSF Point Spread Function

RIP regulated intramembrane proteolysis

RNAP RNA polymerase

SMALL-LABS Single-Molecule Accurate LocaLization by LocAl Background Subtraction

SMAUG Single-Molecule Analysis by Unsupervised Gibbs sampling

strp streptomycin

SMF single-molecule fluorescence

SMT single-molecule tracking

SPTs single-particle trajectories

TCP toxin-coregulated pilus

TcpP-PAmC TcpP-PAmCherry

toxTpro *toxT* promoter

V. cholerae *Vibrio cholerae*

WT wild-type

ABSTRACT

Bacteria have developed a variety of mechanisms to adapt to changes in the environment in ways that are often vital to their continued proliferation and survival. Single-molecule fluorescence (SMF) imaging and tracking have elucidated the complex mechanisms of these responses in a variety of bacteria. SMF encompasses a variety of techniques that overcome the diffraction limit of light by detecting and localizing single molecules. However, a technological gap remains: due to cell sample preparation limitations, all of the SMF experiments in live bacteria are performed at steady state such that all components have reached equilibrium. Therefore, this dissertation aims to address this gap in technology and access single-molecule dynamics during real-time changes by implementing two alternative sample preparations: microfluidic devices and chitosan-coated coverslips.

Chapter I provides background regarding bacteria adaptation to environment changes and in depth information regarding one example discussed throughout this dissertation, *Vibrio cholerae* (*V. cholerae*). It explores the optics principles of single-molecule imaging and how it improves the localization precision of optical imaging. As an example of diffraction-limited single-molecule imaging, Chapter II discusses imaging Colicin E1 in live *Escherichia coli* (*E. coli*) cells. Finally, Chapter I points out one key limitation of SMF in live bacteria cells: the available sample preparations, and indicates two new technologies that could provide solutions.

V. cholerae, the Gram-negative bacterium responsible for the human cholera disease, uses a membrane-localized transcription factor, TcpP, to regulate toxin and virulence factor production in response to changes in the environment. Chapter III describes SMF imag-

ing and tracking performed on TcpP-PAmCherry (TcpP-PAmC) in live *V. cholerae* cells at a virulence-inducing steady-state condition. The experiments discussed in Chapter III determined that TcpP and ToxR work cooperatively under steady-state conditions, but measurements of how these dynamical interactions change over the course of environmental perturbations were precluded by the traditional preparation of bacterial cells confined on agarose pads. This challenge leads to Chapter IV, which describes the first novel sample preparation method to address this gap: chitosan-coated coverslips. The chapter discusses the procedure of making chitosan-coated coverslips, confirms the suitability of these coverslips for experiments with live bacteria cells, and demonstrates that the TcpP-PAmC dynamics acquired in cells on chitosan match those acquired in Chapter III on traditional sample preparation. Additionally, a proof-of-concept experiment is detailed to display the ability to monitor changes in dynamics during real-time changes in the cell environment.

Chapter V describes the implementation of this new chitosan-coated coverslip method to examine the effect of pH changes on TcpP-PAmC dynamics with 5-minute temporal resolution. It discusses the importance of this method to unveil a new sequestering mechanism for *V. cholerae* toxin regulation. Then, Chapter VI describes the implementation of this new chitosan-coated coverslip method to examine short-term stress conditions in *E. coli* cells. Low concentrations of hydrogen peroxide (H_2O_2) are added to live cells immobilized on the coverslip while tracking an important DNA-binding protein, DNA-binding Protein from Starved cells (Dps). Changes in dynamics of Dps-PAmCherry (Dps-PAmC) occur almost immediately which would not be detectable using traditional sample preparation, further emphasizing the need for chitosan-coated coverslips.

As a second solution to the sample preparation limitations for fluorescence imaging in live bacteria, Chapter VII describes the development of a microfluidic device to immobilize bacteria cells even while flowing new media past the cells. It discusses the fabrication procedure for making the final device, important factors to consider when designing and fabricating a microfluidic device, and imaging and tracking single TcpP-PAmC molecules

in live *V. cholerae* cells in the device. Since the device does not work during environment changes yet, this chapter also proposes possible improvements and changes to achieve that ultimate goal.

Finally, Chapter VIII discusses future directions for studying the toxin regulation pathway in *V. cholerae* and other environment changes of interest. Possible applications for both the chitosan-coated coverslips and microfluidic devices are proposed. The chapter also discusses next steps for understanding the Dps-PAmC response during oxidative damage and other areas of *E. coli* stress response the new methods developed in this dissertation could impact. This dissertation collectively expands the SMF imaging toolbox for probing bacterial systems and extends the questions this technique is capable of exploring.

CHAPTER I

Introduction

Calkins, A.L.*, Demey, L.M.*, Karslake, J.D., Donarski, E.D., Biteen, J.S., and DiRita, V.J.

Calkins, A.L., Demey, L.M., Rosenthal, B.M., DiRita, V.J., and Biteen, J.S.

This dissertation discusses the expansion of the toolbox available for studying bacteria with new methods for preparing bacteria cells for single-molecule fluorescence (SMF) imaging. Scientists have worked to understand the intricate interactions of proteins inside bacteria cells since the invention of the microscope. Today, SMF imaging techniques are pushing the capabilities of the microscope and helping scientists find the answers to

many previously unanswerable questions about these systems [3, 4]. SMF encompasses a variety of techniques with the goal of overcoming the diffraction limit of light to localize single molecules. However, a technological gap remains: due to cell sample preparation limitations, all of the SMF experiments in live bacteria are performed at steady state such that all components have reached equilibrium. Bacteria constantly change their subcellular interactions in response to environment conditions, and real-time understanding of these changes will greatly benefit our ability to counteract the deadly diseases they cause. Therefore, my research is developing sample preparation platforms that allow for solution-based environment changes while performing SMF microscopy. I have developed two sample preparation strategies: a slide coating with chitosan and a microfluidic device. I have applied the chitosan-coated coverslip method to study two bacteria during real-time environment perturbation: *Vibrio cholerae* (*V. cholerae*) and *Escherichia coli* (*E. coli*). Ultimately, this method can be applied to many bacteria systems and allow biologists and microscopists alike to further understand these complex organisms.

1.1   Bacteria Adaptation

Behavior adaptation to environmental changes is vital to bacterial survival and proliferation. Bacteria have developed a variety of mechanisms to adapt to changes in the environment [5]. Environmental signals trigger changes in growth rate, cell secretions such as toxin and quorum-sensing agents, and nutrient storage [6–9]. There are many examples. *E. coli* uses DNA-binding proteins during environment stress to protect DNA and extend their life [8]. *Streptomyces* spp. bacteria activate proteins in the Pho box to regulate metabolism in response to changes in phosphate in their environment [9]. *Bacteroides thetaiotaomicron* (*B. theta*) activates different polysaccharide utilization loci in response to changes in food source [10]. *V. cholerae*, the focus of most of this dissertation, regulates toxin production in response to changes in pH, temperature, bile salts, and autoinducers [1, 11].

This toxin from *V. cholerae* infects millions of people each year predominantly in impoverished communities with poor access to clean water [12,13]. A few treatment options for the cholera disease exist including vaccines, antibiotic therapy, and oral rehydration therapy; however, ~100,000 human deaths occur annually [14–21]. The number of annual cholera infections is projected to continue to increase due to a growing prevalence of antibiotic-resistant *V. cholerae* like many other bacteria [22]. Additionally, the continued climate crisis has led to more outbreaks of cholera in areas affected by hurricanes and flooding. To address this growing global burden of cholera, development of alternative methods of treatment is needed which can be driven from new insight into the pathogenesis of *V. cholerae*. Bulk biochemical assays have identified the proteins responsible for regulation, TcpP and ToxR, [23–27] and showed that this regulation is highly altered by changing environmental conditions [6, 28–31]. However, the exact mechanisms for control employed by these proteins remains unknown. In this Dissertation, I implement SMF imaging to gain insight into these mechanisms and designed new sample preparation methods to implement SMF imaging during real-time environment changes.

SMF imaging is not only beneficial to answering the mechanistic questions about *V. cholerae*, but also widely applicable to many bacteria of interest. Studies on these environment change response pathways have been performed in vitro using a variety of bulk assays, but live-cell SMF imaging can provide more information on the mechanisms for the signaling pathways [32]. Additionally, studying these environment change response pathways during real-time environment changes is vital to establishing a comprehensive mechanism. Therefore, the new sample preparation methods for SMF imaging I develop in this Dissertation will lead to elucidating mechanisms for many important bacteria.

1.2   Optical Microscopy and Fluorescence

Optical and fluorescence microscopies can be used to study signaling pathways in bacteria [4]. The microscopy set-up used for the experiments in this dissertation is diagramed

in Fig. 1.1. Using white-light illumination and a 100x objective, bacteria cell morphology can be observed. A phase-contrast objective is used to phase shift the light waves, creating contrast from differences in the sample components' refractive indices: for instance, though cells and water are both weakly absorbing, their difference in refractive index enables high-contrast images in a phase-contrast microscope. Therefore, cells appear dark on the camera while water appears light, allowing for observation of these cells without staining. To see features inside the cell on the nanometer-scale, we need to differentiate the signal from the cell boundaries and increase the signal from the cell background.

By attaching a fluorescent molecule to a molecule of interest inside the cell, we can observe the position of the molecule in relationship to the cell. Since most biological molecules are not intrinsically fluorescent, these fluorescent markers can be organic dyes chemically bound to the molecule of interest or fluorescent proteins genetically encoded as a fusion to a protein of interest. Fluorescence occurs when a fluorophore (the fluorescent molecule) absorbs a photon (excitation) and releases a photon (emission) at a longer wavelength. Upon excitation, the fluorophore molecule is excited from the ground state, S_0, to a higher energy excited state, S_1. Internal conversion, a loss of energy through vibrational relaxation, brings the molecule to the lowest energy state of the S_1 state (Fig. 1.2a). When the molecule relaxes back down to the S_0 state, a photon is emitted at a longer wavelength. The difference between the maximal excitation wavelength and the maximal emission wavelength is the Stokes shift (Fig. 1.2b). Each fluorophore has a distinct excitation and emission spectra from other fluorophores [33]. This collection of photons from the fluorescent molecule can be distinguished from the background of the cell and correlated to the features seen from phase-contrast microscopy.

4
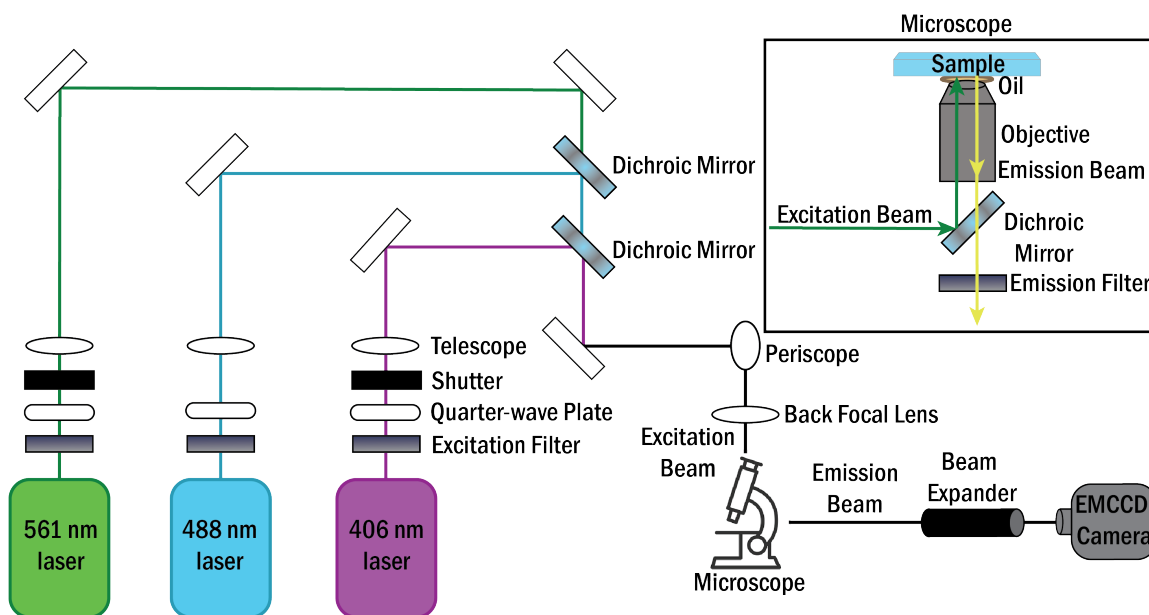
Figure 1.1: Fluorescence microscopy setup. Lasers are directed from source to microscope with a series of filters and mirrors. The microscope is in an inverted setup. The excitation path is filtered to ensure only the precise desired wavelength reaches the sample, and a quarter wave-plate produces a circularly polarized beam. Emission path is filtered to remove the excitation wavelength and ensure only the emission wavelength is directed to an electron multiplying charged-couple detector (EMCCD) camera for detection.
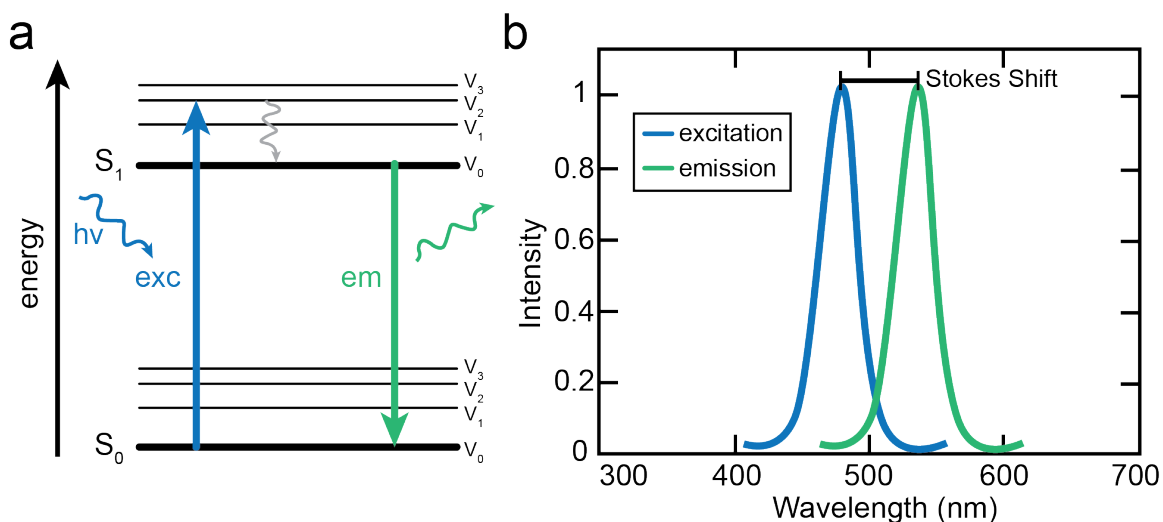
Figure 1.2: General overview of fluorescence. a) A simplified Jablonski diagram illustrates the phenomenon of fluorescence. An absorbed photon excites (exc) a molecule from the singlet ground state (S_0) to a singlet excited state (S_1). Emission (em) occurs after some non-radiative loss of vibrational energy and radiative relaxation back to S_0. b) Simplified fluorescence excitation (blue, left) and emission (green, right) spectra showing the Stokes shift.

1.3   Single-molecule Fluorescence Imaging

Optical microscopy methods are limited by the diffraction limit of light which depends on the magnification (100 x for experiments in this dissertation) and numerical aperture (NA) of the objective and the input light. The NA characterizes the range of angles over which the system can accept and emit light according to equation 1.1:

$$NA = n sin\theta \tag{1.1}$$

Here, n is the refractive index of the medium between the coverslip and objective and θ is one half of the objective's angular aperture. The objective used for the experiments described in this Dissertation has a NA of 1.4. The diffraction limit of light (the Rayleigh limit), d, is defined according to equation 1.2:

$$d = \frac{\lambda}{2NA} \tag{1.2}$$

Here, λ is the wavelength. This limitation is approximately 200 nm based on the experiment conditions used for the high-NA fluorescence microscope in this dissertation. Therefore, fluorescence microscopy alone cannot be used to resolve fine subcellular details at 1-2 nm [34]. One way to overcome this limitation is by detecting single molecules and then finding the sub-diffraction-limited center position of each molecule image (Point Spread Function (PSF)), for instance by fitting the PSF of each single molecule to a 2D Gaussian (Fig. 1.3a). This fitting results in localization precision of 10-40 nm rather than 200-300 nm. The localization precision depends inversely on the total number of detected photons, N, according to equation 1.3:

$$Localization\ precision \propto \frac{1}{\sqrt[2]{N}} \tag{1.3}$$

The localization precision can be improved by increasing the number of photons detected, so a high-quantum yield EMCCD camera is used for detection (Fig. 1.1). However, if two molecules are simultaneously detected too close together, below ~200 nm, this fitting method cannot distinguish their overlapping PSFs.

Achieving nanometer-scale microscopy in this wide-field microscope therefore requires the imaging of spatially isolated fluorescent molecules in each imaging frame. When the density of molecules is too high, Photoactivated Localization Microscopy (PALM) separates the emission from single molecules in time to resolve molecules previously unresolvable (Fig. 1.3b) [35]. Molecules of interest are tagged with a photoactivatable fluorescent molecule, such as PhotoActivatable mCherry (PAmC) [36], which through a conformational change is converted from a molecule not able to absorb the excitation light to a molecule able to absorb the excitation light. Fluorescent molecules stochastically convert upon absorbing light from a high-energy activation wavelength (406 nm) and then fluoresce when excited by a different lower-energy wavelength (561 nm). When the activation light is low in power, only a few molecules convert; therefore, these molecules do not overlap in any specific imaging frame and can be distinguished from one another when fitting for localization. Excited molecules eventually photobleach, photochemical alteration of a dye or a fluorophore molecule such that it is permanently unable to fluoresce and therefore only the background signal of the cell is detected. The activation, excitation, and then photobleaching process is repeated until a sufficient number of molecules have been localized in the cell (Fig. 1.3c).

1.4   Single-molecule Tracking

One major benefit of SMF imaging is the ability to image in live cells; therefore, molecules can be monitored during normal cell function. Because the cell is maintaining itself, the molecules being monitored bind to and unbind from their assigned targets. Molecule binding tends to slow molecular diffusion, so observing changes in the molecular diffusion
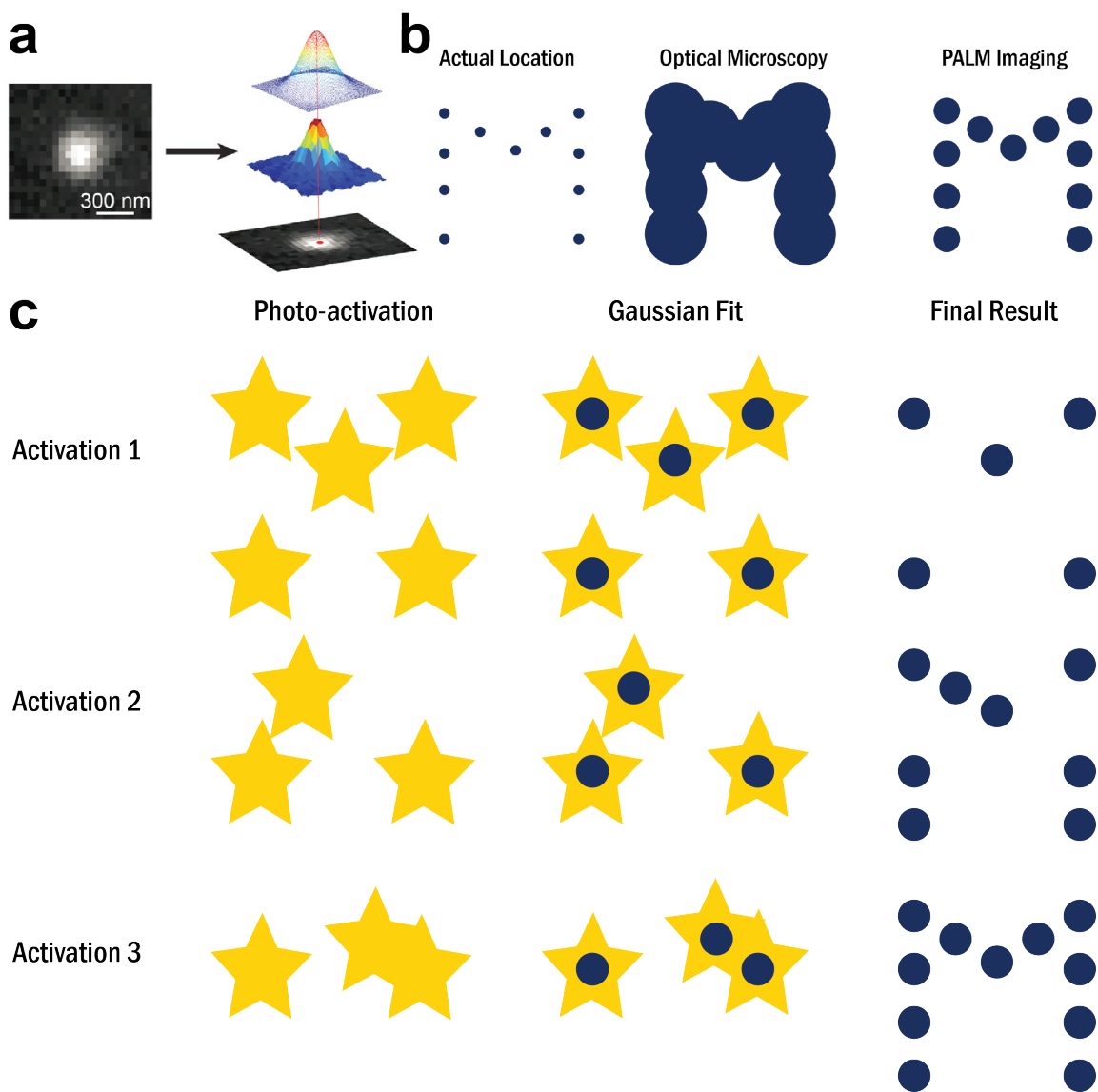
Figure 1.3: Super-resolution imaging. a) The PSF is fit to a 2D Gaussian function to precisely determine the center of the emission pattern and localize the molecule position. Reproduced from Tuson et al., reference 2. b) Optical microscopy is subject to diffraction and therefore molecules smaller than the wavelength of light appear larger than their true size. With PALM, some resolution can be recovered. c) Rounds of low-power activation from a 406-nm laser will photo-activate a few photoactivatable molecules at a time, separating their PSFs in time.

leads to insight into the biochemical function of the molecule of interest. Changes in diffusion of the molecule of interest can be detected using single-molecule tracking. In each frame of the movie, the molecule is localized in a new position. The distance between each localization is a step. The steps can be connected into a track describing the motion of the molecule during the time it was imaged in the living cell before photobleaching [37]. For the case of Brownian motion, this track can be related to the diffusion coefficient, D, of the molecule using equation 1.4:

$$\left\langle r^2(\tau) \right\rangle = 2nD\tau \tag{1.4}$$

where $\left\langle \left\langle r^2(\tau) \right\rangle \right.$ denotes the mean squared displacement (MSD) of the molecule during a given time interval, τ, and n denotes the dimensionality of the motion. All molecules analyzed in this dissertation were assumed to engage in Brownian motion consistent with equation 1.4.

Thousands of molecules from hundreds of cells are localized and tracked, leading to a distribution of diffusion coefficients from each data point. An average diffusion coefficient can be statistically quantified from this distribution. In reality, these molecules diffuse at multiple rates as they serve multiple biochemical functions, and each biochemical function is therefore characterized by a different average diffusion coefficient. Averaging the tracks to attain a single average diffusion coefficient greatly oversimplifies the data set. The data set can be fit to multiple diffusion coefficients representing individual diffusion states. Each biophysical state corresponds to a biochemical state for the molecule of interest. To fit these complex data sets a specific number of states must be chosen, introducing bias into the data interpretation. To address this problem, an analysis algorithm based on nonparametric Bayesian statistics was created: Single-Molecule Analysis by Unsupervised Gibbs sampling (SMAUG) [38]. SMAUG assigns the single-molecule displacements that make up a collection of trajectories into the most probable diffusion states, and it quantifies the weight fraction and average diffusion coefficient of each state using Gibbs

sampling in a Bayesian framework (Fig. 1.4).
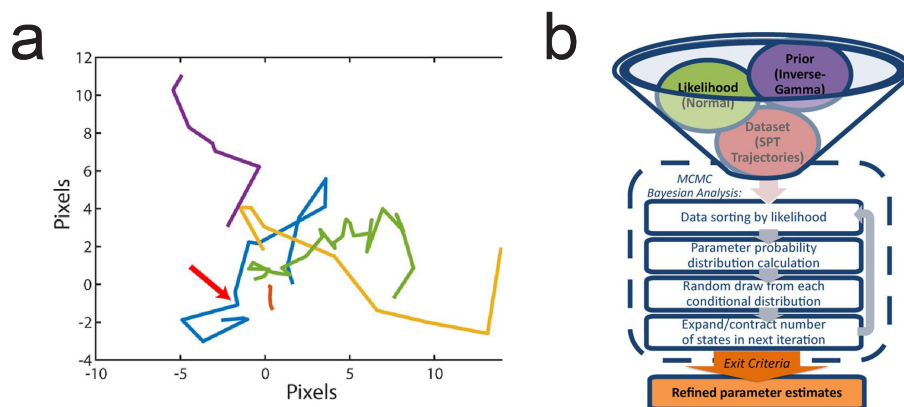
Figure 1.4: The Single-Molecule Analysis by Unsupervised Gibbs sampling (SMAUG) algorithm. a) A collection of five single-particle trajectories (SPTs) in an environment where single molecules can diffuse at different rates and transition from one state to another. The yellow trajectory has a large average diffusion coefficient, whereas the green trajectory has a small average diffusion coefficient. The red arrow along the blue trajectory marks a transition between states that is difficult to identify by eye. b) Graphical representation of the SMAUG algorithm, which combines the likelihood, prior, and dataset (top) into a Bayesian framework Markov Chain Monte Carlo algorithm that iterates through four steps to refine the parameter estimates (dashed line) until some exit criteria are satisfied. Reproduced from Karslake et al., reference [38].

1.5 Limitations of Single-molecule Imaging and Tracking

To accurately localize and track single molecules in live bacteria cells, the cells must be immobilized. To immobilize the cells while maintaining their access to important nutrients, cells are typically sandwiched between a pad of agarose gel in cell media and a glass coverslip [2, 39]. However, this confined geometry does not allow for changes to the cell environment after the initial sample preparation. Thus, conventional sample preparation methods are incompatible with registering the effect of real-time perturbations during live-cell single-molecule imaging and tracking.

Recent developments in two technologies—microfluidics and slide coatings—have enabled the ability to make real-time perturbations during single-molecule imaging experiments while maintaining the physiology of the bacterial cell [2] Microfluidics designs

have been developed for imaging and single-cell manipulations, including trapping bacteria cells, over the past two decades [40, 41]. For example, the "mother machine" traps bacteria to analyze cell lineages [42–44]. In this dissertation, I adapt this mother machine design to address the requirements of single-molecule imaging in bacteria cells, including decreasing the channel size and optimizing the connectivity between large and small channels. Furthermore, appropriately coated microscope coverslips immobilize bacteria cells without impeding access for real-time exchange of the cell media. Recently, preparation of bacteria on chitosan-coated slides has been shown to immobilize bacteria cells by charge-charge interactions with the acetylated side chains without altering cell growth or physiology [45, 46]. Chitosan slide coatings therefore represents a significant advantage relative to other slide coatings like poly-L-lysine, which can immobilize bacteria cells but which has been shown to increase the cell area and induce division defects [47–49]. Fluorescence imaging of bacteria mounted on chitosan-coated coverslips had been previously explored [45], but single molecules had not been imaged or tracked within bacteria cells immobilized in this way. While chitosan-coated coverslips offer a simple solution to change the environment during imaging, microfluidic devices would allow for more control.

These new technology advances open our ability for new experiments studying a variety of bacteria with single-molecule imaging and tracking during real-time environmental perturbations. I will describe their application to studying *V. cholerae* during real-time changes in pH and *E. coli* during real-time oxidative damage.

1.6   Dissertation Objectives

With the growing cases of bacterial outbreaks and antibiotic resistance, understanding the mechanisms employed by bacteria is of great importance. Optical and fluorescence imaging provide a large toolbox for exploring these mechanisms in live cells, but some limitations exist, including upon imaging during real-time environment perturbations, a

key factor in bacteria proliferation. As such, the aims of this dissertation are to design, evaluate, and implement new sample preparation methods to enable SMF imaging during real-time environment perturbations.

In Chapter II, I describe the use of diffraction-limited SMF microscopy in live *E. coli* cells to further probe the understanding of the Colicin E1 mechanism in conjunction with biochemical assays performed by others [50]. I found that ColE1-TR, a truncated protein lacking the cytotoxic domain, remains stalled on the outer membrane and does not fully translocate into cells. This stalling can be used to block the native TolC function as an antibiotic efflux pump.

In Chapter III, I track the membrane-bound transcription factor TcpP in live *V. cholerae* cells to gain a deeper understanding of its ability to regulate toxin production and its inter-action with its binding partner ToxR. These data refine the previous model of cooperativity between TcpP and ToxR in stimulating *toxT* expression [27,38] and demonstrate that TcpP locates the *toxT* promoter independently of ToxR [1]. This study was performed at a pH 6 to maintain steady state virulence inducing conditions, but leaves questions remaining about the TcpP mechanism, displaying the need for new methods for SMF imaging.

In Chapter IV, I discuss the development of a novel method for imaging live bacteria cells during real-time environment changes using chitosan-coated coverslips [2]. This new method addresses limitations in SMF imaging in live non-adherent cells such as bacteria. I use *V. cholerae* as a proof-of-concept system and validate our ability to detect cellular re-sponse to real-time environment changes by monitoring changes in subcellular diffusion states.

In Chapter V, I implement the new chitosan slide method to study the effects of pH on TcpP in live *V. cholerae* cells [2]. By changing the media of the sample on the microscope, we can monitor changes in diffusion with 5-minute temporal resolution. These changes in diffusion states give insight into the biochemical function of TcpP in regulating toxin production in *V. cholerae* in response to changes in pH.

In Chapter VI, I implement the new chitosan-coated coverslips method to study the effects of oxidative damage on DNA-binding Protein from Starved cells (Dps) in live *E. coli* cells. By comparing the changes in Dps dynamics after additions of hydrogen peroxide (H_2O_2) to after starvation, I begin to elucidate the various mechanisms Dps uses to respond to a variety of stressors. I display the need for faster temporal resolution to detect changes in dynamics not possible with traditional sample preparation.

In Chapter VII, I discuss the development of a microfluidic device as an additional more complex solution for imaging during real-time environment perturbations [2]. I describe the process of fabricating the functional device and common errors and roadblocks. I show data of single-molecule tracking in live bacteria cells in a microfluidic device for the first time. Additionally, I provide insight into potential solutions for improving the functionality of the device to perform the full desired experiments.

Finally, in Chapter VIII, I summarize the new methods developed for SMF imaging and tracking in live bacteria cells and the biological insights made into two sample systems, *V. cholerae* and *E. coli*. I provide recommendations for future applications of the methods and potential changes for applying the chitosan coated coverslips method to anerobic bacteria. The work presented in this dissertation broadly addresses the necessity for studying bacteria during environment changes and introduces how new sample preparation methods can enable this study.

Live-cell Imaging of Colicin E1 in *Escherichia coli*

This chapter describes Anna Calkins's contributions to work previously published in eLife.
I performed the experiments and analysis in Figures 2.2, 2.3, 2.4, and 2.5.

2.1 Introduction

Gram-negative bacteria such as *Escherichia coli* (*E. coli*) form concentric barriers to protect the cell from extracellular threats. The most formidable such barrier is the cell the outer membrane [51]. External molecules can gain access to the cell through various barrel-shaped proteins embedded in the bacterium outer membrane [52]. These Outer Membrane Proteins (OMPs) allow the import of nutrients and metabolites and the export of toxins and waste [52]. Bacteriocins, protein toxin systems bacteria use for bacterial warfare, exploit OMPs to cross the impermeable outer membrane, ultimately killing the bacterium. Colicins are *E. coli*-specific bacteriocins with a variety of receptor targets and killing mechanisms. Most colicins share a common tri-domain architecture: an N-terminal

translocation (T) domain, a receptor-binding (R) domain, and a C-terminal cytotoxic (C) domain (Fig. 2.1) [53–55]. Colicin E1 has a unique binding site unlike other colicins: the T domain of Colicin E1 binds to TolC, the outer membrane component of the acridine efflux pump, and the R domain binds to BtuB, the vitamin B12 transporter and primary receptor shared by all E colicins [56, 57]. Prior work on Colicin E1 has found the structure of the cytotoxic domain and preliminary biochemical assays display that portions of the colicin remain tethered to their OMPs partners as the cytotoxic domain depolarizes the cytoplasmic membrane [58–61].

I used diffraction-limited single-molecule fluorescence (SMF) microscopy in live *E. coli* cells to further probe the the Colicin E1 mechanism in conjunction with biochemical assays performed by others [50]. I found that ColE1-TR, a truncation of the protein lacking the cytotoxic domain, remains stalled on the outer membrane and does not fully translocate into cells. This stalling can be used to block the native TolC function as an antibiotic efflux pump [62, 63].

2.2 Materials and Methods

2.2.1 Bacterial Strains

E. coli strains BW25113 and JW5503-1 were purchased from the Coli Genetic Stock Center (CGSC). JW5503-1 is a tolC732(del)::kan from the parent strain BW25113. BL21(DE3) was used for the production of the colicin constructs and TolC. BL21(DE3) has a premature stop codon at residue 58 of the *btuB* gene and therefore we used it as a Δ*btuB* strain for microscopy.

2.2.2 Expression and Purification

The gene for ColE1-TR was synthesized as a gBlock (Integrated DNA Technologies) and cloned into pET303. Inverse PCR was used to delete the R domain and produce col-
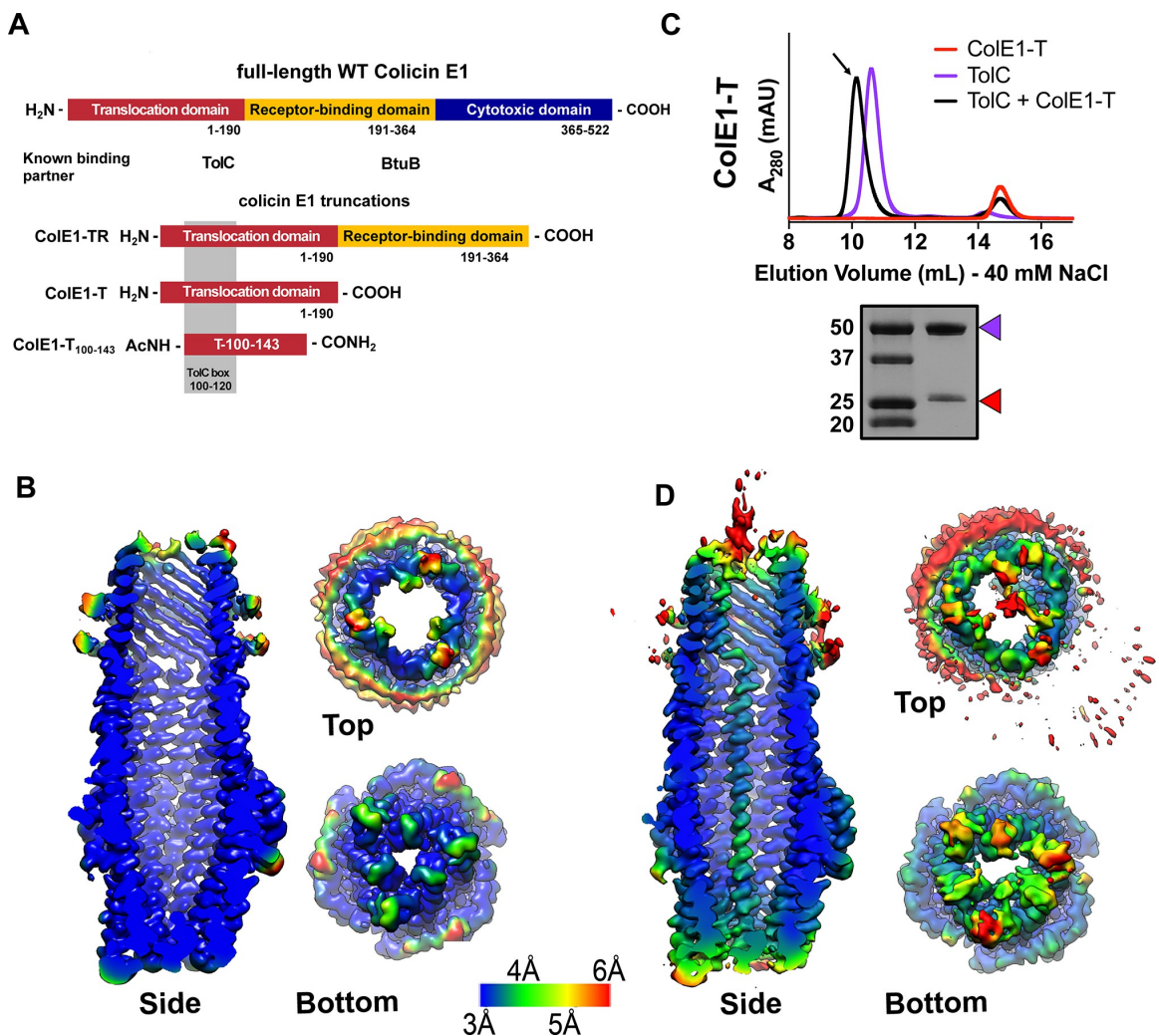
Figure 2.1: Colicin E1-T binds within the lumen of TolC. (A) Architecture of full-length colicin E1 showing domains and their known binding partners. Three truncation constructs were used in this study. (B) CryoEM structure of TolC embedded in nanodiscs. Side, top, and bottom views are colored by local resolution, as computed in cryoSPARC from the final half-maps. The side view is cropped to display the particle interior. (C) SEC chromatogram of ColE1-T (red line) and TolC (purple line). The arrow indicates the co-elution (black line) fractions (eluted in buffer containing 40 mM NaCl) that were analyzed by SDS-PAGE. On the SDS-PAGE gel (bottom), red arrows indicate the presence of the colicin E1 construct that has co-eluted with TolC. (D) The CryoEM structure of ColE1-T bound to TolC and colored by local resolution as in (B). cryoEM, cryo-electron microscopy; SEC, size exclusion chromatography.

16

icin E1-T. Colicin E1-TR-Green Fluorescent Protein (GFP) was produced by inserting GFP at the C terminus of ColE1-TR. A gBlock (Integrated DNA Technologies) was synthesized for GFP containing complementary flanking sequences to the plasmid with ColE1-TR and inserted with the omega-PCR technique. ColE1-TR$_{\Delta 1-40}$ was produced by inverse PCR to delete residues corresponding to 1 through 40. All point mutants (ColE1-T-E192C, ColE1-TR-E366C, ColE1-TR-E366C$_{\Delta 1-40}$, and ColE1-T-P110A) were generated by inverse PCR with mutagenic primers.

Plasmids were transformed into *E. coli* BL21(DE3) cells and plated on lysogeny broth (LB) + agar + 100 μg/ml carbenicillin. Single colonies were inoculated into 50 ml LB broth with 100 μg/ml carbenicillin and grown overnight at 37°C with shaking at 250 rpm. Proteins were produced by inoculating 1 L of TB supplemented with 0.4% glycerol, 10 mM MgCl$_2$, and 100 μg/ml carbenicillin with 20 ml of the overnight culture. The culture was grown at 37°C to an OD600 of 2.0 and induced with 1 mM isopropyl-β-D-thiogalactopyranoside (IPTG). Expression cultures were then grown at 15°C for 24 hr and harvested at 4000g for 30 min at 4°C. Cell pellets were resuspended at 3 ml/g of cell pellet in lysis buffer (TBS, 5 mM MgCl$_2$, 10 mM imidazole, 1 mM PMSF, 10 μg/ml DNase, and 0.25 mg/ml lysozyme) and lysed via sonication (2 min, 2 s on, 8 s off, 40% amplitude, QSonica Q500 with 12.7 mm probe) in an ice bath. Lysates were centrifuged at 4000g for 10 min to remove un-lysed cells and debris. The supernatant was centrifuged again at 50,400g in a Beckman Coulter J2-21 for 1 hr at 4°C. Clarified lysates were applied to a 5-ml HisTrap FF column and purified using an ÄKTA FPLC system with a 20-column volume wash step with binding buffer (TBS, 25 mM imidazole) and eluted using a linear gradient from 0% to 50% elution buffer (TBS, 500 mM imidazole) in 10 column volumes. Concentrated proteins were loaded onto a HiLoad Superdex 16/60 200 pg gel filtration column and eluted into phosphate buffer saline (PBS) pH 7.4.

2.2.3 Protein Tagging

Cysteine mutations were introduced at the C-terminus before the histidine tag for fluorophore conjugation. These constructs were purified as described in the Expression and purification section with the addition of 1 mM TCEP in all buffers. All subsequent steps were performed with limited exposure to light and in amber tubes. Cyanine3 (Cy3) maleimide (Lumiprobe) was reconstituted in Dimethyl sulfoxide (DMSO). Fluorophore labeling was achieved by mixing a 20-fold molar excess of Cy3 maleimide to protein and incubating overnight at 4°C. Free dye was removed by gel filtration on a Sephadex NAP-10 G-25 column. Simultaneously to the dye removal, the sample was buffer exchanged into storage buffer (PBS pH 7.4, 1 mM Dithiothreitol (DTT), and 1 mM Ethylenediaminetetraacetic acid (EDTA)). The degree of labeling was determined spectrophotometrically from the concentrations of the dye and protein solutions using their respective extinction coefficients, ε, as described by their manufacturers or for the proteins as estimated by Expasy ProtParam (Cy3 ε_{548} nm=162,000 L mol^{-1} cm^{-1}; ColE1-T-E192C ε_{280} nm=9970 L mol^{-1} cm^{-1}; ColE1-TR-E366C ε_{280} nm=14,440 L mol^{-1} cm^{-1}). Labeling efficiencies were 75% and 85% for ColE1-T-E192C and ColE1-TR-E366C, respectively. Protein concentrations were adjusted according to the percentage of labeled protein.

2.2.4 Microscopy Sample Preparation

Cultures of *E. coli* (wild-type (WT), $\Delta tolC$, or BL21(DE3)) were grown in LB medium at 37°C with shaking (180 r.p.m.) overnight, then transferred to MOPS minimal medium (Teknova) with 0.2% glycerol and 1.32 mM K$_2$HPO$_4$ and grown at 37°C for 13 hr. The sample was transferred to MOPS medium and grown to turbidity at 37°C overnight. A 1-ml aliquot of culture was centrifuged for 2 min at 4850g to pellet the cells. The pellet was washed in 1 ml MOPS and centrifuged a second time. The supernatant was then removed, and the cell pellet was resuspended in 500 μl MOPS. A 1.0-μl droplet of concentrated cells was placed onto a glass slide. Then, a 1.0-μl droplet of 1 μg/ml colicin E1-Cy3 protein

construct stock was added to the cells. The droplet was covered by an agarose pad (1% agarose in MOPS media) and a second coverslip.

2.2.5 Fluorescence Microscopy

Samples were imaged at room temperature using wide-field epifluorescence microscopy with sensitivity to detect single dye molecules as described previously [4]. Briefly, fluorescence was excited by a 561-nm laser (Coherent Sapphire 560-50) for Cy3 or a 488-nm laser (Coherent Sapphire 488-50) for GFP. The lasers were operated at low power densities (1–2 W/cm^2), and fluorescence was imaged with an Olympus IX71 inverted microscope with a 100×, 1.40-NA phase-contrast oil-immersion objective and appropriate excitation, emission, and dichroic filters. A Photometrics Evolve electron multiplying charged-couple detector (EMCCD) camera with >90% quantum efficiency captured the images at a rate of 20 frames per second. Each detector pixel corresponds to a 49 nm × 49 nm area of the sample. *E. coli* cells were identified and fluorescent signals were detected using the Single-Molecule Accurate LocaLization by LocAl Background Subtraction (SMALL-LABS) algorithm [37].

2.3 Results and Discussion

I probed the interaction between the cell membrane and surface-localized ColE1-TR with SMF microscopy using the fluorescent dye Cy3 [4, 64]. When ColE1-TR-Cy3 was added to the extracellular environment of WT BW25113 *E. coli* (containing TolC), distinct puncta (Fig. 2.2A), right, Fig. 2.3) formed on 94% of the cells (number of cells, n=111) (Fig. 2.2B); cells with observed puncta most often featured a single punctum, though a small fraction had two puncta. On average, the WT cells had 1.2 puncta. In a Δ*tolC* strain, puncta were observed on only 18% of cells (n=99) (Fig. 2.2A, right; Fig. 2.2B); on average, the Δ*tolC* cells had 0.2 puncta. As a Δ*btuB* control strain, we used BL21 (DE3) which is known to have a premature stop codon at BtuB residue 58 [65]. Puncta were observed on only 3% of
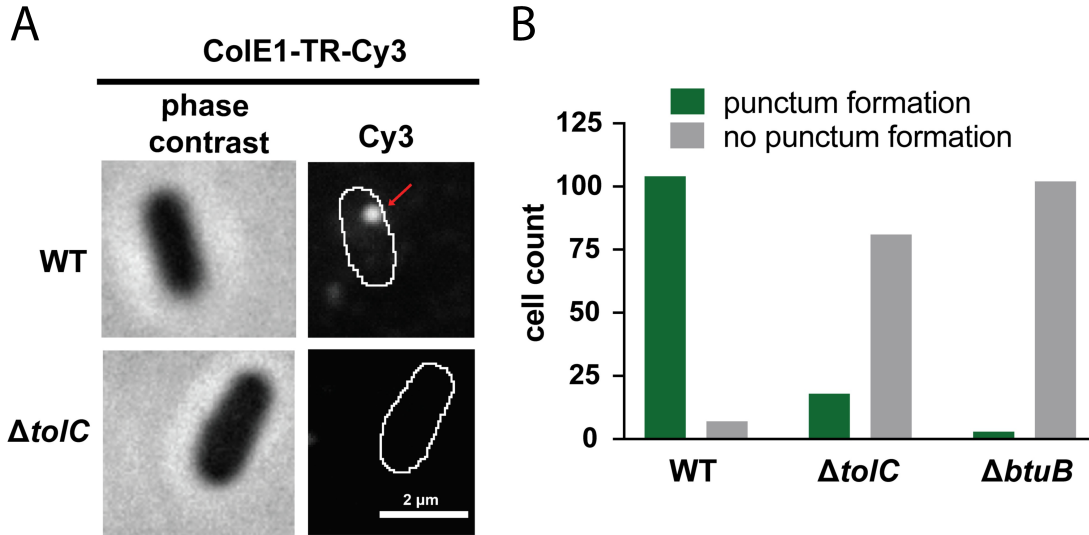
Figure 2.2: Colicin E1-TR localizes on the cell. (A) Fluorescence image (right) of ColE1-TR-Cy3 overlaid on outlines of living *E. coli* cells from phase-contrast microscopy (left) for WT and Δ*tolC*. Red arrow points to a punctum. A larger variety of images is also available (Fig. 2.3) Similar localization was seen for ColE1-TR-GFP (Fig. 2.4) demonstrating that the effect was not caused by the fluorophore, and ColE1-TR$_{\Delta 1-40}$-Cy3 (Fig. 2.5) demonstrating that the effect is not TolA dependent. The puncta were stable and were found to remain intact for more than 5 min. The punctum shown here remained intact for at least 30 s (Video 4-1 in Reference [50]) (B) Cell counts where ColE1-TR-Cy3 punctum formation was observed for WT, Δ*tolC*, and Δ*btuB*. Number of cells observed, n=111, 91, 105, respectively.

cells lacking BtuB (n=105) (Fig. 2.2A, Fig. 2.3, Fig. 2.4A); on average, the Δ*btuB* cells had 0 puncta.

The bright ColE1-TR-Cy3 puncta photobleach over time as they are observed in the fluorescence microscope, ultimately leaving a single-molecule fluorescing before complete photobleaching. We therefore divided the brightness of each punctum by the brightness of that single molecule to estimate the number of molecules in each cluster [66]. In WT and Δ*tolC* cells that featured puncta, ColE1-TR form puncta consistent with 20 molecules; we never detect an isolated single ColE1-TR molecule on either WT or Δ*tolC* cells before photobleaching. The observed size and number of molecules agree with previous studies of BtuB clusters [67, 68] and the punctum locations within the cell were variable. To rule out punctum formation as an artifact of Cy3 conjugation, we found ColE1-TR-GFP
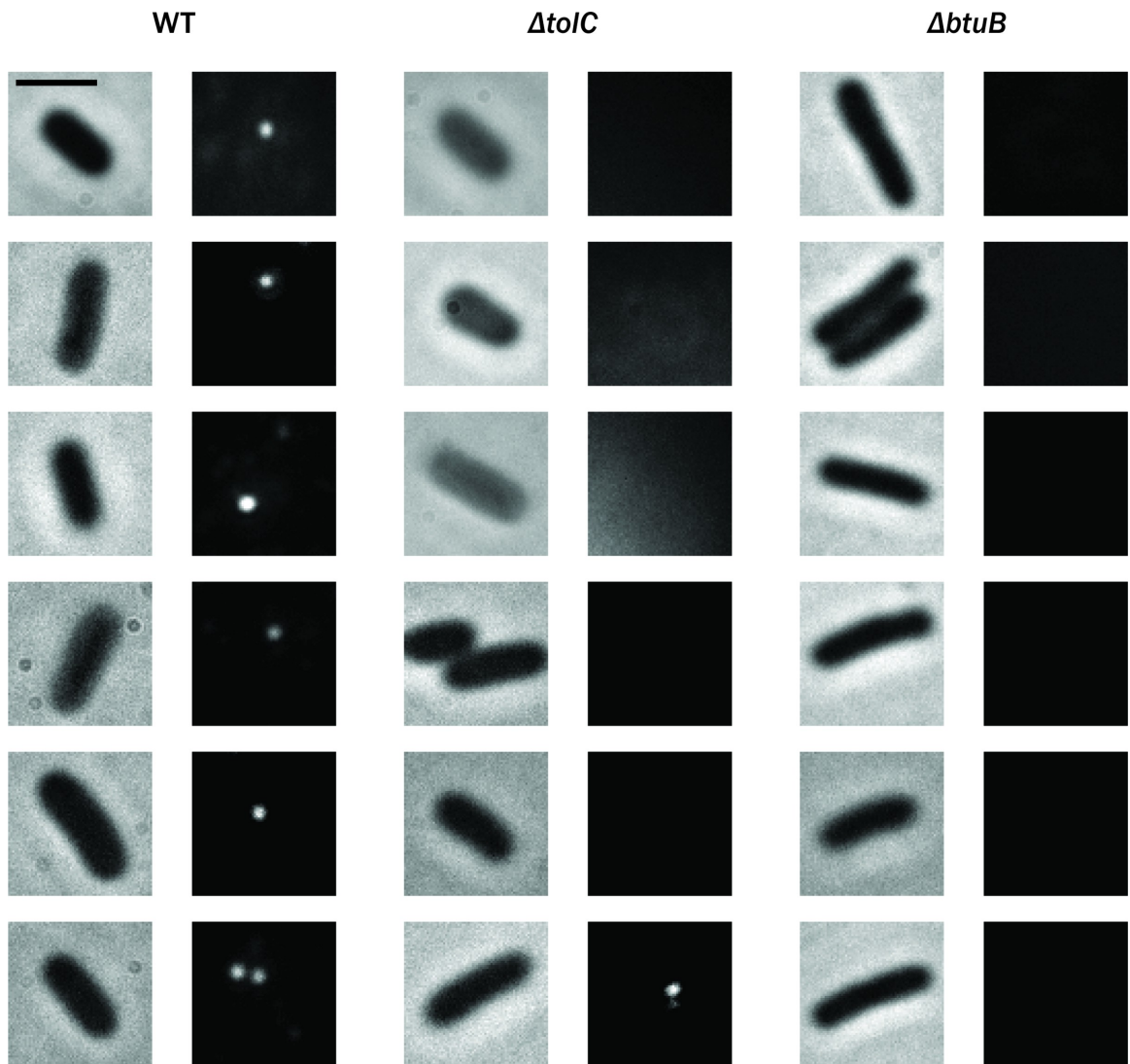
Figure 2.3: Colicin E1-TR localizes on the cell continued. Additional examples of cells observed during imaging described in Fig. 2.2A and B. Brightfield phase-contrast images of living *E. coli* cells (left) and fluorescence images (right) of ColE1-TR-Cy3 for WT, Δ*tolC*, and Δ*btuB*. Scale bars: 2 μm.
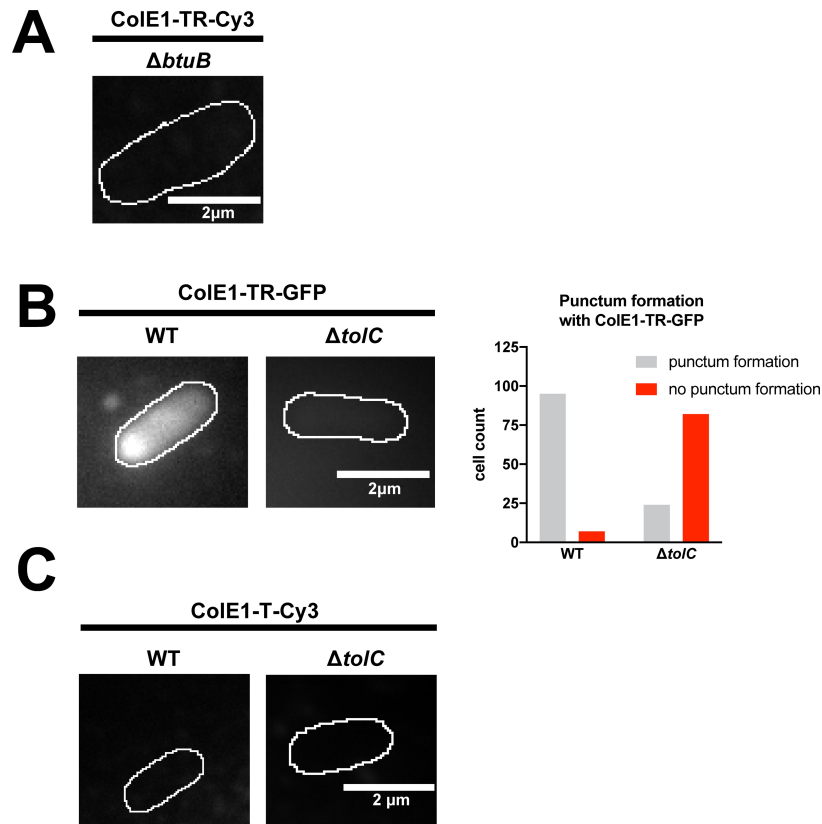
Figure 2.4: Colicin E1-TR binding specific. Single-molecule microscopy fluorescence images overlaid on outlines of living *E. coli* cells from phase-contrast microscopy for WT and Δ*tolC* for ColE1-TR-GFP and counts of cells where ColE1-TR-GFP punctum formation was observed. (A) 97% of cells showed no binding of Cy3-labeled ColE1-TR to Δ*btuB* (B) ColE1-TR-GFP forms similar puncta as Cy3-labeled ColE1-TR (Fig. 2.2A). (C) No binding of Cy3-labeled ColE1-T to WT or Δ*tolC* cells was detected with Cy3-labeled ColE1-T.

displayed the same cluster formation as ColE1-TR-Cy3 (Fig. 2.4B).

Because we usually only see one punctum per cell, we anticipate that some BtuB and TolC may remain unbound because of the geometric constraints of punctum formation. ColE1 must engage both TolC and BtuB simultaneously. Therefore, both receptors must be in close proximity, similar to the 50 Å proximity of BtuB to OmpF when both bound to another type A colicin, ColE9 [69]. Given the two-dimensional surface of a membrane, there are restrictions to how many proteins can be within 50 Å of any other protein. For the clusters we see to occur, when BtuB clusters together in groups of approximately 20 (Fig. 2.2) TolC must also cluster in groups of approximately 20, ultimately requiring ap-

proximately 40 proteins in a relatively small area. The competition between the clustering of BtuB and the requirement for proximity of BtuB and TolC for binding could lower the number of BtuB/TolC sites available for the T and R domains of colicin E1 due to the relative TolC and BtuB geometries needed for ColE1 binding.

Fluorescently labeled pyocins, the colicin analog in *Pseudomonas*, have previously been used to detect translocation across the outer membrane of *P. aeruginosa* [70]. Here, we use an analogous experiment with fluorescently labeled ColE1 to determine cellular localization in *E. coli*. In time courses, bound ColE1-TR puncta remained immobile for >5 min (Video 4-1 in Reference [50] corresponds to 30 s of data used to attain the WT image in Fig. 2.2A). This is consistent with the continued association of ColE1-TR with membrane-embedded BtuB, which has limited mobility [71]. This result indicates that ColE1-TR does not fully translocate [70], because if ColE1-TR entered the periplasmic space it would freely diffuse on these timescales.

Colicin constructs lacking the R domain (ColE1-T-Cy3) showed no detectable binding either to WT or Δ*tolC* cells (Fig. 2.4c), indicating that the TolC-ColE1-T interaction is weaker than the BtuB-ColE1-TR interaction, likely due to the absence of the R domain-BtuB interaction.

TolA is known to be required for ColE1 cytotoxicity [53, 72]. ColE1 lacking the TolA box at the N-terminal T-domain, residues 1-40, would likely be translocation incompetent due to uncoupling from TolA. Similarly, there is a loss of biological activity due to mutations in ColE9 N-terminal region that indirectly interacts with TolA [73, 74]. Biological inactivation has also been caused by mutation to the Tol-Pal interacting regions of ColE3 [75] and ColA [72]. We found that ColE1-TR$_{\Delta 1-40}$ binds to the cell surface of WT, Δ*tolC*, and Δ*btuB* in a similar manner as ColE1-TR (Fig. 2.5). Cell surface localization of ColE1-TR matching that of translocation deficient ColE1-TR$_{\Delta 1-40}$ suggests that ColE1-TR puncta are not within the cell and likely stalled on the outer membrane receptor.
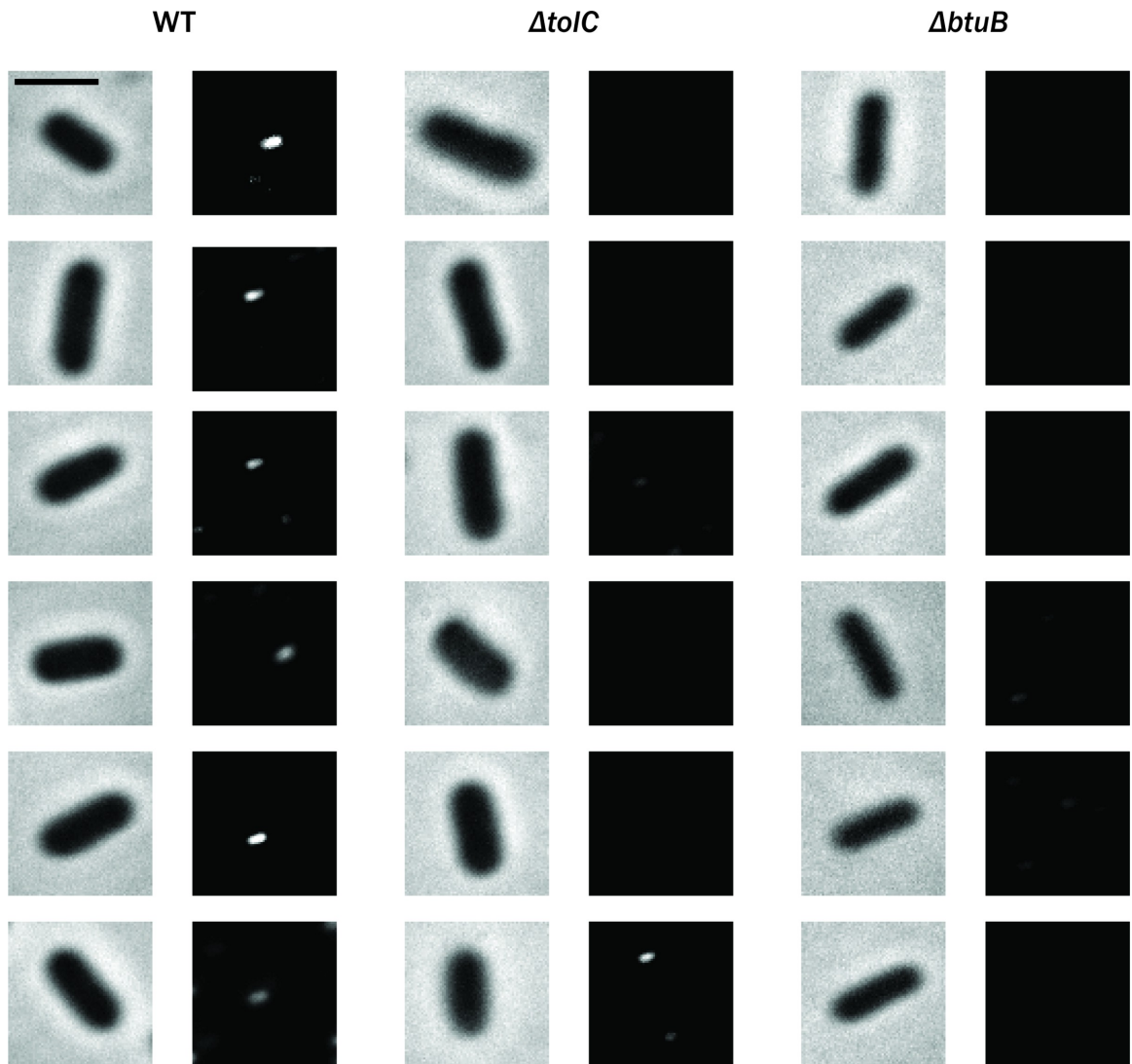
Figure 2.5: Colicin E1-TR$_{\Delta 1\text{-}40}$-Cy3 binds similarly to cells Examples of cells observed with ColE1-TR$_{\Delta 1-40}$-Cy3.Brightfield phase-contrast images of living *E. coli* cells (left) and fluorescence images of ColE1-TR-Cy3 for WT, $\Delta tolC$, and $\Delta btuB$. Scale bar: 2 μm.

2.4   Conclusions

We determined that ColE1 localizes to the outer membrane and does not fully translocate into the periplasmic space. This binding requires both the binding site, TolC, and the receptor site, BtuB, on the outer membrane of the *E. coli* cell. Additionally, the R domain of the colicin protein is required for the localization of the T domain to the TolC channel. Taken together with our collaborators' experiments [50], these discoveries helped to determine the structure and mechanism of ColE1 insertion and led to an alternative approach for targeting OMPs: the development of molecular plugs that block OMPs pores.

CHAPTER III

Independent Promoter Recognition by TcpP Precedes Cooperative Promoter Activation by TcpP and ToxR

3.1 Introduction

The Gram-negative bacterium *Vibrio cholerae* (*V. cholerae*) infects millions of people each year, causing the diarrheal disease cholera resulting in $\sim$ 100,000 deaths annually [12, 13], despite treatments available to combat infection, including vaccines, antibiotic therapy, and oral rehydration therapy [14–21]. With changing climate and growing cases of antibiotic-resistant *V. cholerae*, the number of annual cholera infections is projected to continue to increase [22]. Thus, gaining deeper insight into the pathogenesis of

V. cholerae will facilitate development of alternative methods of treatment, thereby reducing the global burden of cholera.

Upon ingestion, typically from contaminated water or food, *V. cholerae* colonizes the crypts of the villi in the distal portion of the small intestine and stimulates production of virulence factors essential for disease progression, such as the toxin-coregulated pilus (TCP) and cholera toxin (CtxAB) [76–81]. Transcription of *tcp* and *ctxAB* is directly activated by ToxT [11, 23, 82, 83]. Expression of *toxT* is highly regulated and positively stimulated by ToxR and TcpP, two membrane-localized transcription activators (MLTAs), which directly bind to the *toxT* promoter (*toxTpro*), with binding sites at -104 to -68 and -55 to -37, respectively [7, 23, 26, 84–88]. TcpP and ToxR are bitopic membrane proteins, each containing a cytoplasmic DNA-binding domain (within the PhoB and OmpR families, respectively), a single transmembrane domain, and a periplasmic domain [89]. ToxR appears to have an accessory role in *toxT* regulation. Evidence supporting the model that ToxR assists TcpP in *toxT* expression includes that (i) TcpP binds downstream of ToxR, closer than ToxR to the putative RNA polymerase binding site on *toxTpro*, and (ii) overexpression of TcpP results in ToxR-independent *toxT* transcription activation [7, 23, 85, 88]. Furthermore, we have previously measured the single-molecule dynamics of TcpP and noted that deletion of *toxR* decreases but does not eliminate the prevalence of TcpP-DNA binding events [27]. However, it remains unclear how TcpP and ToxR identify the *toxTpro* from the cytoplasmic membrane.

Signal transduction pathways in prokaryotes consist of one-component and two-component regulatory systems that manage cellular processes in response to extracellular information such as pH, temperature, chemical gradients, and nutrients [90–92]. One-component regulatory systems combine their input and output functions in a single protein. MLTAs are a unique family of one-component regulators as they function from the cytoplasmic membrane, whereas the majority (~97%) of one-component regulators are localized in the cytoplasm [90]. These one-component MLTAs like TcpP and ToxR com-

prise a sensor domain and an output domain that are separated by a transmembrane domain. MLTAs have been experimentally characterized in other, Gram-positive and Gram-negative, pathogenic bacteria and have been shown to regulate genes important for pathogenesis (such as capsule production, acid tolerance, antibiotic resistance, virulence gene regulation, and natural competence) [93–102]. Using the Microbial Signal Transduction Database (MIST), we collected candidate MLTAs from 20 bacterial species and found that the prevalence and diversity of MLTAs are much higher than previously anticipated Fig. 3.1. These data indicate that MLTAs are more common among bacteria than previously appreciated. Yet, it remains unclear how MLTAs identify a specific promoter(s) while localized to the cytoplasmic membrane. Some challenges emerge in understanding how MLTAs affect their function of activating transcription in response to external stimuli. For example, diffusion of these regulators is constrained to the cytoplasmic membrane. Additionally, the chromosome structure, which is not static, is known to influence the association of an MLTAs with its target sequence [103–112]. How MLTAs locate their target sequences while bound to the membrane represents a major gap in our knowledge. Here, we investigated the subcellular single-molecule dynamics of TcpP-PAmCherry (TcpP-PAmC) to understand how TcpP localizes to the *toxTpro* and to develop a general model for how MLTAs identify their DNA targets.

Our approach was to apply superresolution single-molecule tracking (SMT) in living cells. Previous work demonstrated that TcpP molecules exhibit heterogeneous diffusion patterns [27,38]. Here, we expand upon this earlier work to study the effect of specific mutations, which alter TcpP binding to DNA or the potential association of TcpP with ToxR, on TcpP subcellular mobility. By tracking the movement of TcpP-PAmC molecules within single living *V. cholerae* cells, we determined the distributions of the heterogeneous motions of TcpP and detected changes in these diffusion coefficients in response to targeted genetic alterations. From these data, we identify three biophysical states (fast diffusion, intermediate diffusion, and slow diffusion), we propose a biological role corresponding to
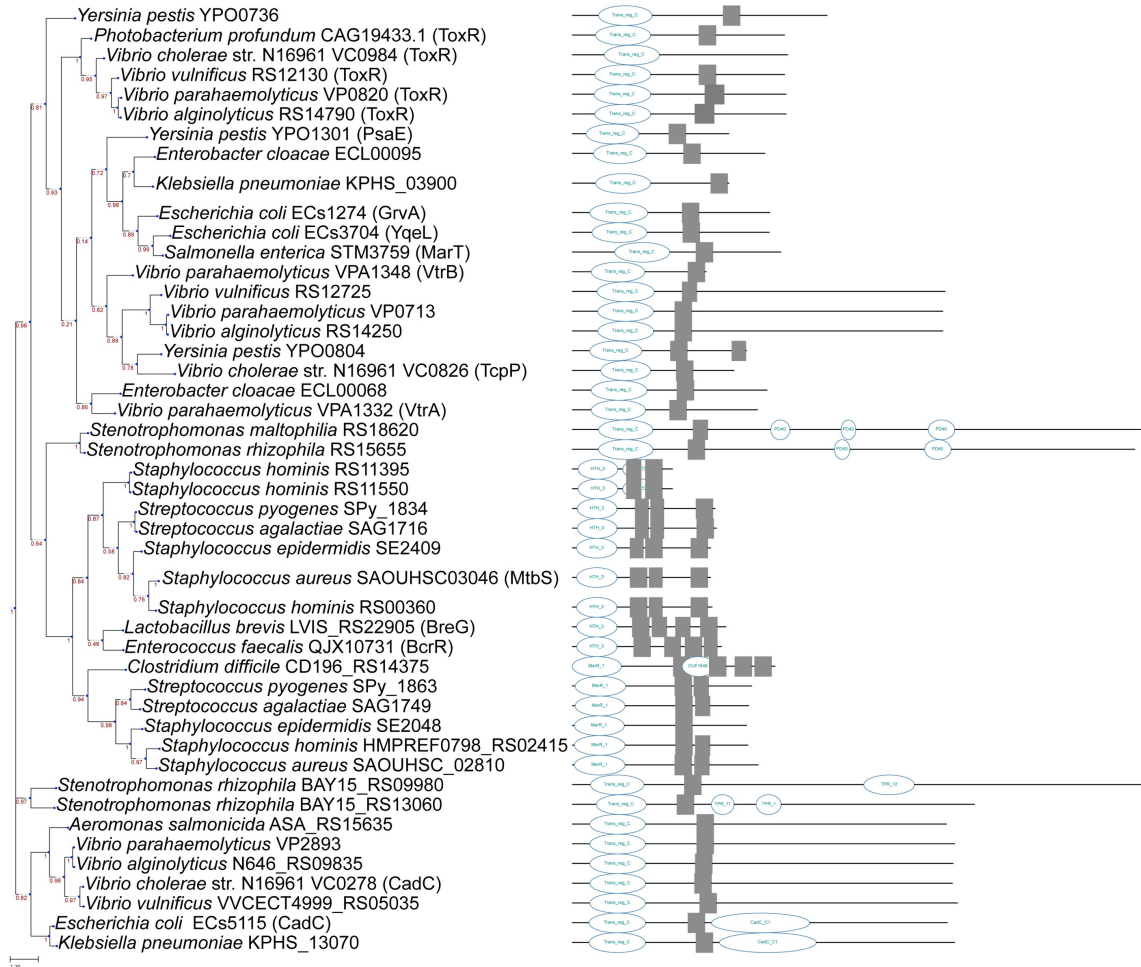
Figure 3.1: Maximum likelihood phylogenetic tree of MLTAs collected from the MIST database. Phylogenetic tree generated using the TREND server [12,13]. MLTAs displayed here represent a portion of the total MLTAs identified in our small survey. Genus and species information displayed on each branch followed by locus tag and gene designation, where applicable. Numbers next to branch points indicate the bootstrap value. Bootstrap values were generated from 100 replicates. The corresponding MLTAs genes are displayed on the right with their predicted domain(s) (in blue) and transmembrane domain(s) (in gray).

each state, and we suggest an alternative model of *toxT* activation where TcpP independently identifies the *toxTpro* prior to assistance from ToxR.

3.2 Materials and Methods

3.2.1 Bacterial Strains and Growth Conditions

Escherichia coli (*E. coli*) and *V. cholerae* strains used here can be found in Table 3.1. Unless otherwise stated, *E. coli* and *V. cholerae* cells were grown on lysogeny broth (LB) plates, or in LB at 210 rpm, at 37℃. LB was prepared according to previous descriptions [113]. To stimulate virulence, *V. cholerae* cells were diluted from overnight cultures in LB and subcultured under virulence-inducing conditions: LB, pH 6.5, 110 rpm, 30℃; filter sterilized. Here, the LB pH was adjusted by adding HCl (1 M) to pH 6.5 (±0.05), and then the medium was filter sterilized to maintain pH. Where appropriate, antibiotics and cell wall intermediates were added at the concentrations given in parentheses: streptomycin (100 μg ml^{-1}), ampicillin (100 μg ml^{-1}), and diaminopimelic acid (DAP) (300 μM).

3.2.2 Plasmid Construction

Plasmid vectors were purified using the Qiagen miniprep kit. Plasmid inserts were amplified from *V. cholerae* genomic DNA using Phusion high-fidelity polymerase (Thermo Scientific). Splicing by overlap extension was used to combine the entire plasmid insert sequences together; see Table 3.2 for the primer list. Plasmid vector was digested by restriction digestion using KpnI-HiFi and XbaI (New England BioLabs) at 37℃ for 2 h. After digestion, the plasmid vector and insert were added to Gibson assembly master mix (1.5 μl insert, 0.5 μl vector, 2 μl master mix) (New England BioLabs) and incubated at 50℃ for 1 h. Assembled plasmid was electroporated into *E. coli* λpir cells and recovered on LB plates with ampicillin and DAP.

Table 3.1: *V. cholerae* Strain list.

Strain	Description	Reference
V. cholerae 0395 classical biotype	Wild type	DiRita lab collection
V. cholerae Δ *tcpH*	Isogenic deletion	Beck, N.A., et. al. 2004. *Journal of bacteriology*, *186*(24), p.8309.
V. cholerae Δ *tcpP*	Isogenic deletion	Häse, C.C. and Mekalanos, J.J., 1998. *PNAS*, *95*(2),pp.730-734.
V. cholerae Δ *toxRS*	Isogenic deletion	DiRita lab collection
V. cholerae tcpP-PAmCherry	Isogenic construct; TcpP-PAmCherry (C-terminal fusion), native *tcpH* start codon and 3rd amino acid mutated (ATG to GTG and AAA to TAA respectively), both ribosomal binding site and coding sequence of *tcpH* cloned downstream of PAmCherry.	Calkins, A.L.[*], Demey, L.M.[*] et al. 2021. *mBio 12*(5), e02213-21
V. cholerae tcpP-PAmCherry Δ *tcpH*	Isogenic construct	Calkins, A.L.[*], Demey, L.M.[*] et al. 2021. *mBio 12*(5), e02213-21
V. cholerae tcpP-PAmCherry Δ *toxRS*	Isogenic construct	Calkins, A.L.[*], Demey, L.M.[*] et al. 2021. *mBio 12*(5), e02213-21
V. cholerae tcpP-PAmCherry Δ *toxRStoxTpro*(-55-+1)	Isogenic construct	Calkins, A.L.[*], Demey, L.M.[*] et al. 2021. *mBio 12*(5), e02213-211
V. cholerae tcpPK94E-PAmCherry	Isogenic construct	Calkins, A.L.[*], Demey, L.M.[*] et al. 2021. *mBio 12*(5), e02213-21
V. cholerae tcpP-PAmCherry Δ *toxTpro*(-55-+1)	Isogenic construct	Calkins, A.L.[*], Demey, L.M. et al.[*] 2021. *mBio 12*(5), e02213-21
V. cholerae tcpP-PAmCherry Δ *toxTpro*(-112-+1)	Isogenic construct	Calkins, A.L.[*], Demey, L.M.[*] et al. 2021. *mBio 12*(5), e02213-21
V. cholerae tcp-PAmCherry pMMB66eh-*toxR*	Isogenic construct	Calkins, A.L.[*], Demey, L.M.[*] et al. 2021. *mBio 12*(5), e02213-21
E. coli ET12567 Δ *dapA*	Cloning vector recipient	Allard, N., et al. 2015 *Can. J. of Microbiol*, *61*(8), pp. 565-574.
E. coli ET12567 Δ *dapA* pKAS32-(empty vector)	Plasmid vector strain	Skorupski, K. and Taylor, R.K., 1996. *Gene*, *169*(1),pp.47-52.

Table 3.2: *V. cholerae* Primer list. Kpn1-HiFi restriction sites were included in forward primers and Xba1 restriction sites were included in all reverse primers to provide homology between insert and vector sequences.

Description	Sequence
pKAS-TcpP promoter FW	ctaacgttaacaaccggtac TTTCGAGTGATAGAAAAAGG
pKAS-TcpP FW	ctaacgttaacaaccggtac ATGGGGTATGTCCGCGTG
TcpP-PAmCherry FW	atgcactaaaaat ATGGTGAGCAAGGGCGAGGA
TcpP-PAmCherry RV	ccttgctcaccatATTTTTAGT GCATTCTAATGTCTTCT GTTC
TcpH-PAmCherry FW	ctaatgtctt CTTGTACAGCTCGTCCATGC
TcpH-PAmCherry RV	gctgtacaagAAGACATTA GAATGCACAAAAAATTAA AAG
Downstream TcpH-PAmCherry RV	tcatgataagacc CTTGTACAGCTCGTCCATGCC
Downstream TcpH-PAmCherry FW	cgagctgtacaagGGTC TTATCATGAGCCGCCTAG
pKAS-downstream TcpH RV	aaatttgcgcatgctagctatagtt CTTGGTCTTTTTTAGATA ACGTAAGC
TcpPK94E RV	GATCAACGTCTCATGTTCATC
TcpPK94E FW	GATGAACATGAGACGTTGATC
toxTpro Δ (-55−+1) RV	tcccaatcatATCTTAAAATC GAAGTTAATATAAAACTAC
toxTpro Δ (-55−+1) FW	gattttaagatATGATT GGGAAAAAATCTTTTC
pKAS- *toxTpro* Δ (-112−+1) FW	ctaacgttaacaaccggtac GTTGGTGGTGTTCCAGATA ATAC
toxTpro Δ (-112−+1) RV	ttcccaatcaGTATTACAT AAGAAAAACATAAAGTAA CTCATG
toxTpro Δ (-112−+1) FW	tatgtaatacTGA TTGGGAAAAAATCTTTTC
pKAS- *toxTpro* Δ (-112−+1) RV	tgcgcatgctagctatagtt ATCATCAGTAATAAATATAGA GTTATATTTTTTTTC
recA FW	ATTGAAGGCGAAATGGGCGATAG
recA RV	TACACATACAGTTGGATTGCTTG AGG
toxT FW	ACTGATGATCTTGATGCTATGGAG
toxT RV	CATCCGATTCGTTCTTAATTCACC

3.2.3 Bacterial Strain Construction

Strain construction follows the protocol outlined in Skorupski et al. [114]. Briefly, *E. coli* λpir harboring the pKAS plasmid and the donor *V. cholerae* strain were incubated in LB (broth or agar) supplemented with DAP overnight at 37°C. The remaining cells were then spread on LB plates containing ampicillin or thiosulfate-citrate-bile-sucrose (TCBS) plates containing ampicillin. Counterselection for loss of the pKAS construct by *V. cholerae* cells was done by incubating cells in LB for 2 h and then for 2 h with 2,500 μg ml^{-1} streptomycin (strp) (both at 37°C, 210 rpm). Twenty microliters of this culture was spread onto LB plates containing 2,500 μg ml^{-1} of streptomycin and incubated overnight at 37°C. strp-resistant colonies were screened for the chromosomal mutation of interest via colony PCR using Taq DNA polymerase (Thermo Fisher). Genomic DNA was purified from possible mutants and sequenced (Genewiz) to validate the exchange. Because overlapping open reading frames encode TcpP and TcpH, *tcpH* was cloned downstream of PAmCherry to maintain its expression, and a stop codon was introduced within the first three codons of the native *tcpH* coding sequence to prevent out-of-frame translation of PAmCherry.

3.2.4 Growth Curves

V. cholerae strains were initially grown on LB plates containing streptomycin (100μg ml^{-1}) overnight at 37°C, and then an individual colony was picked and grown overnight in LB at 37°C. *V. cholerae* cells were diluted to an optical density at 600 nm (OD600) of 0.01 from the overnight LB into a 96-well plate (Cell Pro) with 200 μL of virulence-inducing medium per well. The plate was then incubated at 30°C with shaking every 30 min before each measurement in a SPECTROstar Omega plate reader (BMG Labtech).

3.2.5   RT-qPCR

RNA was extracted from *V. cholerae* cells grown under virulence-inducing conditions. RNA was preserved by resuspending pellet cells in 1 mL TRIzol (Sigma-Aldrich) and then purified using an RNeasy kit (Qiagen). RNA was further purified with Turbo DNase treatment. RNA quantity and quality were measured via UV-visible (UV-Vis) spectrophotometry (NanoDrop ND-1000) and by detection of large and small ribosomal subunits via 2% agarose gel. RNA was then converted to cDNA using Superscript III reverse transcriptase (Thermo Scientific). Real-time quantitative PCR (RT-qPCR) was performed using 5 ng of cDNA in SYBR green master mix (Applied Biosystems). RecA was used as a housekeeping gene of reference to calculate the cycle threshold values (Δ ΔCT) [115, 116]. See Table 3.2 for primers.

3.2.6   Protein Electrophoresis and Immunodetection

After lysis, total protein concentration samples were measured via Bradford assay. Samples were subsequently diluted to 0.5 μg total protein/μL. All SDS-PAGE gels contained 12.5% acrylamide and were run at 90 to 120 V for 1.5 h. Proteins were transferred to nitrocellulose membranes using a semidry electroblotter (Fisher Scientific) overnight at 35 mA or for 2 h at 200 mA. Membranes were blocked with 5% nonfat milk, 2% bovine serum albumin in Tris-buffered saline, 0.5% Tween 20 (TBST) for 1 h. Membranes were then incubated with primary antibody (anti-TcpA, 1:100,000; anti-TcpP, 1:1,000; anti-TcpH, 1:500; anti-ToxR, 1:50,000; anti-mCherry, 1:1,000) diluted in TBST and nonfat milk (2.5%, wt/vol) for an additional hour at room temperature with shaking. Membranes were then washed 3 times with TBST. Secondary antibody (goat anti-rabbit IgG-horseradish peroxidase [HRP], 1:2,000) (Sigma) was diluted in TBST and nonfat milk (2.5%, wt/vol). Secondary antibody was incubated with the membranes for an additional hour at room temperature with shaking. Membranes were washed again with TBST 3 times and then incubated with Super-Signal HRP chemiluminescence substrate (Thermo Fisher). Membranes were imaged with

an Amersham Imager 600.

3.2.7 Single-molecule Microscopy

V. cholerae strains were grown on LB plates containing streptomycin (100 μg ml^{-1}) overnight at 37°C, and then an individual colony was picked and grown overnight in LB at 37°C. *V. cholerae* cells were diluted from LB under virulence-inducing conditions and grown until they reached mid-log phase. They were then washed and concentrated in M9 minimal medium with 0.4% glycerol. A 1.5-μL droplet of concentrated cells was placed onto an agarose pad (2% agarose in M9, spread and flattened on a microscope slide) and covered with a coverslip. Cells were imaged at room temperature using an Olympus IX71 inverted epifluorescence microscope with a 100X 1.40-numerical aperture (NA) oil-immersion objective, a 405-nm laser (Coherent Cube 405-100; 50 W/cm^2) for photoactivation, and a coaligned 561-nm laser (Coherent-Sapphire 561-50; 210 W/cm^2) for fluorescence excitation. Fluorescence emission was filtered with appropriate filters and captured on a 512- by 512-pixel Photometrics Evolve electron multiplying charged-couple detector (EMCCD) camera. To prevent higher-order excitation during photoactivation, a pair of Uniblitz shutters controlled the laser beams such that samples were exposed to only one laser at a time. During imaging, the cells were given a 40-ms dose of 405-nm light every 90 s. Images were collected continuously every 40 ms, and acquisitions lasted 5 to 7 min each.

3.2.8 Data Analysis

Recorded single-molecule positions were detected and localized based on point spread function fitting using home-built code, Single-Molecule Accurate LocaLization by LocAl Background Subtraction (SMALL-LABS) [37]. This program reduces biases due to background subtraction, increasing the precision of each molecule localization. Subsequent localizations of the same molecule were then connected into trajectories using the Hun-

garian algorithm [117, 118]. All trajectories from each movie for a given condition were combined and analyzed together using the Single-Molecule Analysis by Unsupervised Gibbs sampling (SMAUG) algorithm [38]. This algorithm considers the collection of steps in all trajectories and uses a Bayesian statistical framework to estimate the parameters of interest: number of mobility states, diffusion coefficient, weight fraction, transition probabilities between states, and noise.

3.3 Results

3.3.1 Single-molecule tracking of TcpP-PAmCherry is useful to study promoter identification but cannot probe regulated-intramembrane proteolysis.

To investigate the dynamics of individual TcpP molecules, we generated a *V. cholerae* strain in which the wild-type (WT) *tcpP* allele is replaced with one expressing TcpP fused at its C terminus to a photoactivatable fluorescent protein, PAmCherry (TcpP-PAmC). Levels and activity of TcpP are controlled by a two-step proteolytic process known as regulated intramembrane proteolysis (RIP) [119–121]. Under RIP-permissive conditions (defined as LB, pH 8.5, 37°C, shaking at 210 rpm) the C terminus of TcpP becomes sensitive to proteolysis by Tsp, a site-1 protease, and YaeL, a site-2 protease; this sensitivity results in the inability of the cell to activate *toxT* expression. Under RIP-nonpermissive conditions (defined as LB, pH 6.5, 30°C, shaking at 110 rpm), TcpP is protected from RIP by TcpH [122–124].

We investigated whether we could assess RIP dynamics using single-molecule tracking. Like wild-type TcpP, TcpP-PAmC was sensitive to RIP in the absence of TcpH, indicated by lower levels of TcpP-PAmC in *tcpP-PAmCherryΔtcpH* relative to *tcpP-PAmCherry* Fig. 3.2. Second, in both *tcpP-PAmCherry* and *tcpP-PAmCherryΔtcpH* a smaller species of TcpP-PAmC was observed, referred to as TcpP-PAm* Fig. 3.2A. A similar result has been observed for native TcpP in *ΔyaeL* cells and indicates RIP [123]. Complementation of

tcpP-PAmCherryΔtcpH with a plasmid encoding TcpH resulted in a band with the mass of native TcpP (~29 kDa) Fig. 3.3. These data indicate that TcpP-PAmC resists RIP in a TcpH-dependent fashion similar to native TcpP. As expected, native TcpP was not detected in the absence of TcpH. These data indicate that (i) TcpP-PAmC is sensitive to RIP, (ii) TcpH can protect TcpP-PAmC from RIP, and (iii) addition of PAmCherry to the C terminus of TcpP reduces RIP of TcpP-PAmC relative to TcpP. These conclusions are supported by similar levels of TcpA, CtxB, and *toxT* expression in *tcpP-PAmCherry* and *tcpP-PAmCherryΔtcpH* [38] Fig. 3.2 and Fig. 3.4). Notwithstanding the detectable levels of TcpP-PAmC on immunoblots of total proteins from *tcpP-PAmCherryΔtcpH*, we observed almost no TcpP-PAmC molecules in our single-molecule tracking experiments. As a result, we are unable to collect sufficient data to perform any analysis of *tcpP-PAmCherryΔtcpH* cells. Though we cannot determine how RIP influences TcpP-PAmC single-molecule dynamics, fusion of PAmC to the C terminus of TcpP does not affect its ability to stimulate *toxT* expression (Fig. 3.4). In addition, activity of TcpP is influenced by homodimerization, mediated by a periplasmic cysteine residue (C207) [125, 126]. We sought to determine if addition of PAmC to the C terminus of TcpP promotes its ability to dimerize. To test this, we measured *toxT* expression in both *tcpP-PAmCherry* and *tcpPC207S-PAmCherry* cells (Fig. 3.5). We found that PAmC does not compensate for loss of C207, suggesting that it does not stimulate dimerization of TcpP-PAmC. These data indicate that PAmCherry does not simulate dimerization of TcpP-PAmC. Lastly, addition of PAmCherry to the C terminus of TcpP does not affect the growth rate of *V. cholerae* (Fig. 3.6). Therefore, TcpP-PAmC is an effective tool to understand how TcpP locates the *toxTpro* from its position in the membrane.

SMAUG characterizes the motion of molecules based on the collection of measured displacements (steps) in their single-molecule trajectories. SMAUG estimates the biophysical descriptors of a system by embedding a Gibbs sampler in a Markov chain Monte Carlo framework. This nonparametric Bayesian analysis approach determines the most likely
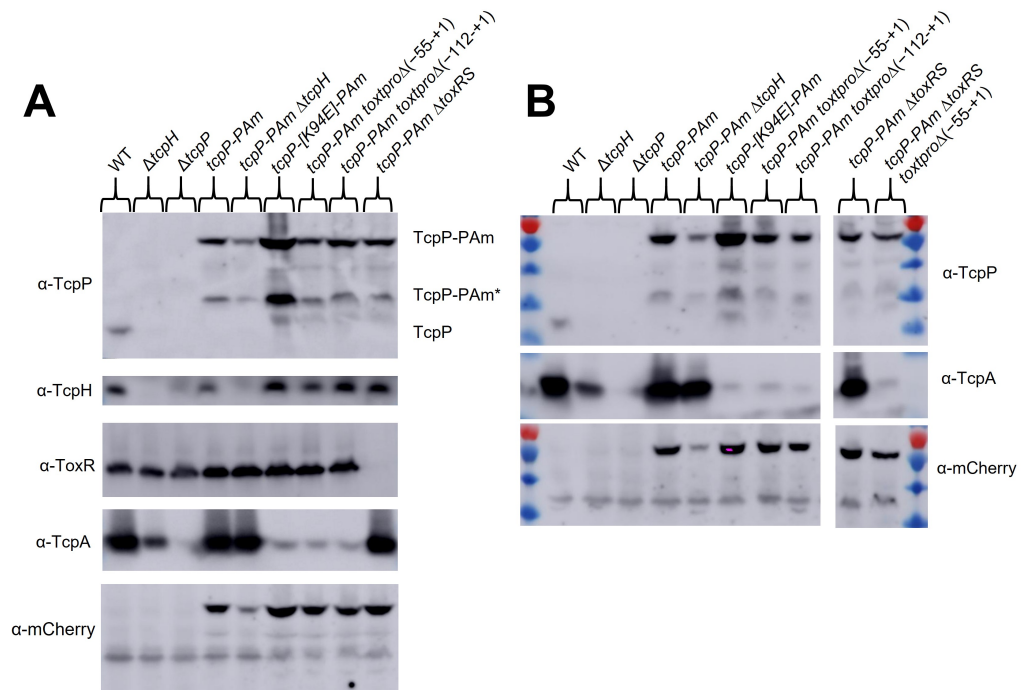
Figure 3.2: Identifying TcpP-PAmCherry vs. TcpP-PAmCherry*. (A and B) Western blot assays of cultures grown under virulence-inducing conditions for 6 h; see Materials and Methods for primary antibody dilution. PAmC is fused to the C terminus of TcpP and is under the control of its endogenous promoter on the chromosome. Addition of PAmC to TcpP results in two species: TcpP-PAmC (~70 kDa) and TcpP-PAmCherry* (~36 kDa). Deletion of *tcpH* yields lower levels of TcpP-PAmC and TcpP-PAmCherry*, likely due to an increase in RIP.
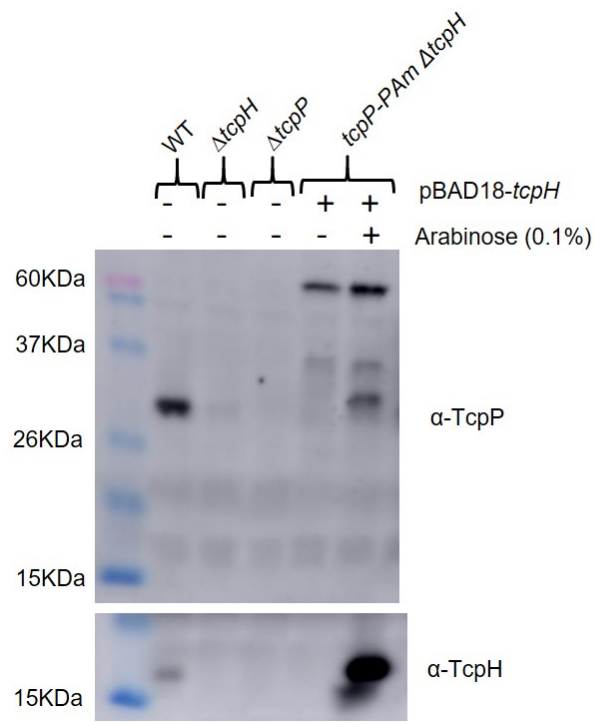
Figure 3.3: Baseline dynamics of TcpP-PAmCherry. Western blot assays of cultures grown under virulence-inducing conditions for 6 h with or without arabinose; see Materials and Methods for primary antibody dilution. *tcpP-PAmC ΔtcpH* cells harbor an arabinose-inducible vector (pBAD18) carrying *tcpH*. Ectopic expression of *tcpH* complemented deletion of *tcpH*. Complementation of *tpcH* also resulted in an additional TcpP band, ~29 kDa, that corresponds to native TcpP.
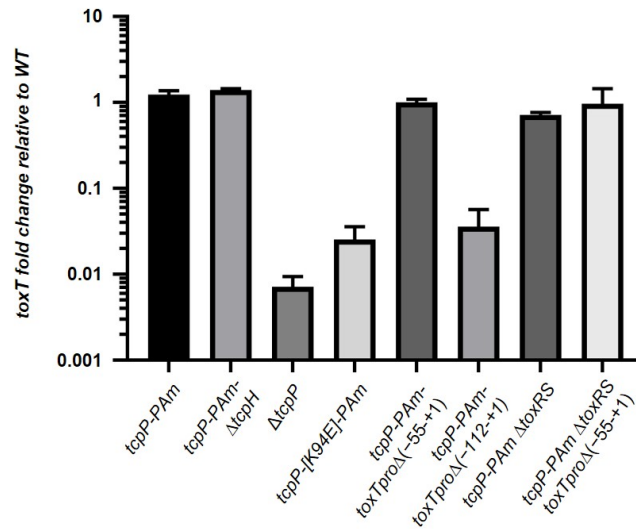
Figure 3.4: *toxT* fold change across various strains. Average *toxT* fold change, relative to WT, across three biological replicates (determined via the Δ ΔCT method) [127]. mRNA was collected from cells after 2 h under virulence-inducing conditions, and error bars represent standard error of the mean.
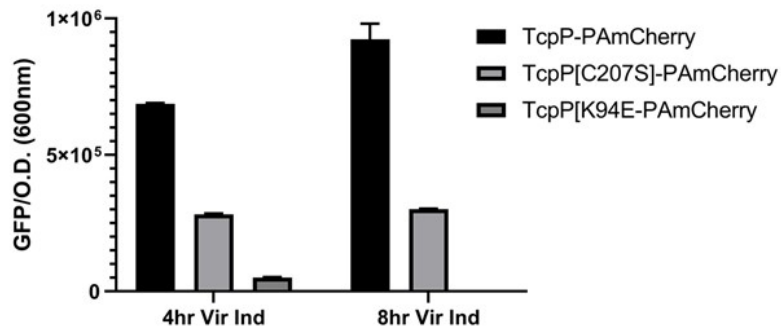
Figure 3.5: *toxT* expression via *toxT*::GFP transcriptional reporter. *toxT* expression in *V. cholerae* cells determined using a plasmid-based *toxT*::GFP transcriptional reporter. At each time point, *toxT* expression was determined by measuring green fluorescent protein (GFP) fluorescence (excitation, 488 nm, and emission, 515 nm) and optical density (600 nm). The data here are an average from three biological replicates. Error bars represent the standard error of the mean.
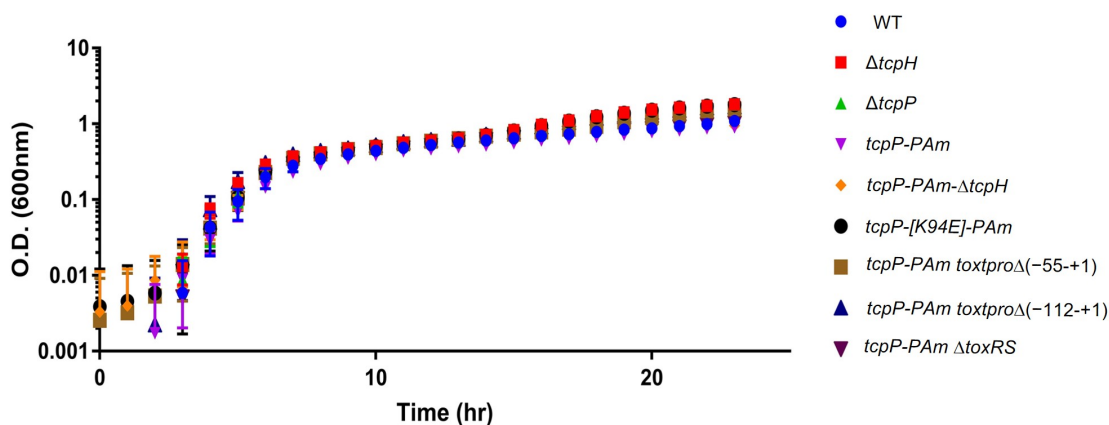
Figure 3.6: In vitro growth curve under virulence-inducing conditions. Optical density (O.D.) values are the average from three biological replicates, and error bars represent standard error of the mean.

number of mobility states and the average diffusion coefficient of single molecules in each state, the population of each state, and the probability of transitioning between different mobility states over the course of a single trajectory [38]. In our previous study, we determined that TcpP-PAmC molecules in *V. cholerae* cells transition between multiple biophysical states: fast diffusion, intermediate diffusion, and slow diffusion [38].

Here, we collected a new robust set of TcpP-PAmC tracking data in living *V. cholerae* cells (54,454 steps collected from 7,601 trajectories) to further refine our analysis and to assign biochemical mechanisms to these biophysical observations (a sample of these tracks is shown in Fig. 3.7B and Supplemental Video in Reference [1]). Consistent with our previous results, we ascertained that TcpP-PAmC exists in three distinct states (slow diffusion, intermediate diffusion, and fast diffusion; blue, orange, and purple, respectively, in Fig. 3.7C). Furthermore, we determined that TcpP-PAmC molecules do not freely transition between all the diffusion states: we observe that TcpP-PAmC molecules can transition between the fast state (purple) and the intermediate state (orange) and between the intermediate state (orange) and the slow state (blue) freely, but there is no significant probability of transitions directly from the fast diffusion state (purple) to the slow diffusion state

(blue) on successive steps (Fig. 3.7D). Thus, the intermediate diffusion state represents a critical biochemical intermediate between the slow and fast diffusion states.

The high transition probability of TcpP-PAmC molecules from the intermediate diffusion state to the fast diffusion state (50%) is unexpected, as the fast diffusion state represents the smallest population of TcpP-PAmC molecules (9%), with a low probability (8%) of TcpP-PAmC molecules transitioning from the fast diffusion state back to the intermediate diffusion state (Fig. 3.7d). While we cannot directly determine how RIP influences the dynamics of TcpP-PAmC, the stark difference in the transition probabilities and the populations of TcpP-PAmC in the fast and intermediate diffusion states suggests that fast-diffusing TcpP-PAmC molecules are potentially sensitive to some form of degradation.

Given this baseline for the dynamics of TcpP-PAmC, we hypothesize that (i) the three diffusion states (slow, intermediate, and fast) are features of TcpP-PAmC molecules with three biologically distinct roles; (ii) the slow diffusion state is occupied by TcpP-PAmC molecules interacting with DNA, such as *toxTpro*; and (iii) the intermediate diffusion state is influenced by ToxR. We further explore these three hypotheses with *V. cholerae* mutants below.

3.3.2   Mutation of the *toxT* promoter Decreases the Slow Diffusion State Occupancy

We hypothesized that the slow TcpP-PAmC diffusion state encompasses molecules specifically interacting with DNA at its binding site in the *toxTpro*. The molecular weight of chromosomal DNA (chromosome 1, 2.96 Mbp) is much higher than that of any protein. Thus, binding of TcpP-PAmC to this promoter on the chromosome should result in an extremely low apparent diffusion rate. To test our hypothesis, we removed key binding sites for TcpP (-55 to -37) and both ToxR and TcpP (-112 to +1) in the *toxTpro*, generating *tcpP-PAmCherry toxTpro*Δ(-55−+1) and *tcpP-PAmCherry toxTpro*Δ(-112−+1) (Fig. 3.8), both of which resulted in a drastic reduction in TcpA production, similar to that of a Δ*tcpP*
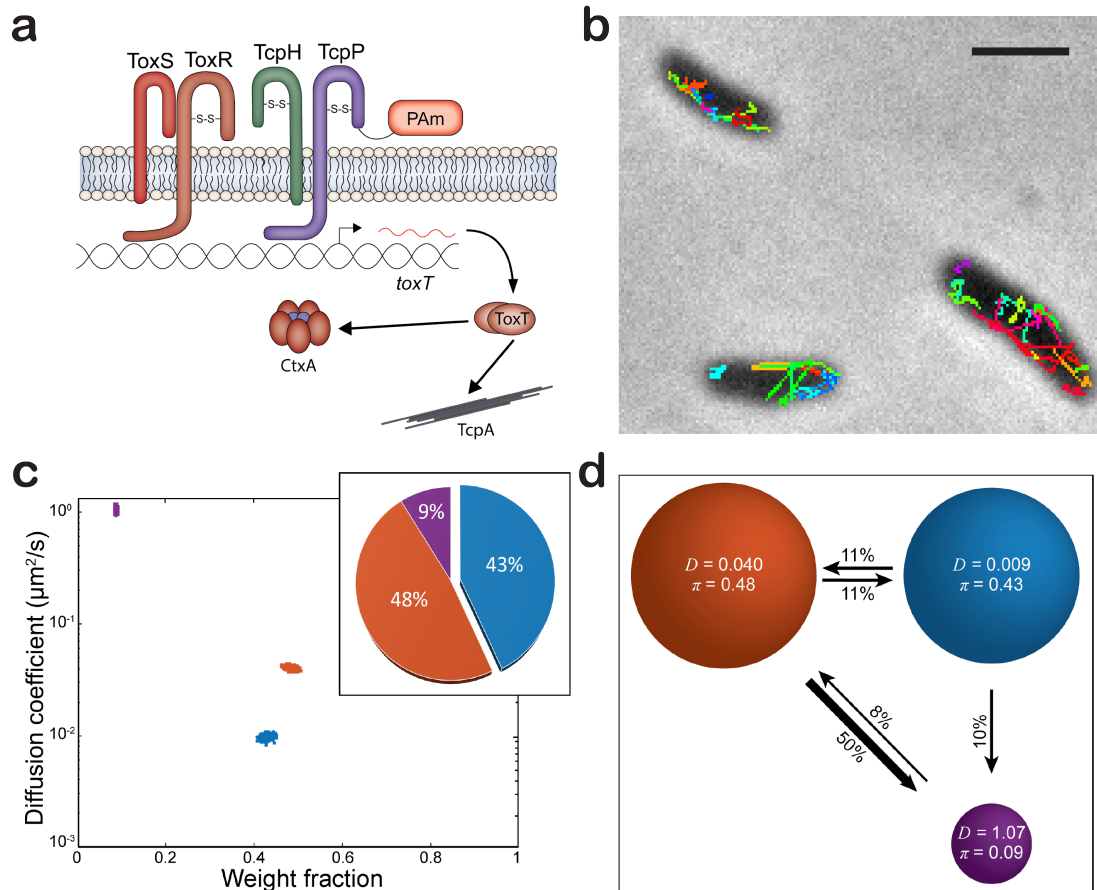
Figure 3.7: Single-molecule imaging and tracking of TcpP-PAmCherry in wild-type *V. cholerae.* (a) Model of *tcpP-PAmC*. (b) Representative single-molecule trajectory maps overlaid on reverse-contrast bright-field image of *V. cholerae* TcpP-PAmC. Only trajectories lasting 0.20 s (5 frames) are shown. Trajectories shown in a variety of colors to show diversity of motion observed. Scale bar, 2μm. (c) Average single-molecule diffusion coefficients and weight fraction estimates for TcpP-PAmC in live *V. cholerae* cells grown under virulence-inducing conditions. Single-step analysis identifies three distinct diffusion states (fast [purple], intermediate [orange], and slow [blue], respectively). Each point represents the average single-molecule diffusion coefficient versus weight fraction of TcpP-PAmC molecules in each distinct mobility state at each saved iteration of the Bayesian algorithm after convergence. The data set contains 54,454 steps from 7,601 trajectories. (Inset) Percentage (weight fraction) of TcpP-PAmC in each diffusion state. Colors as in panel. (d) Based on the identification of three distinct diffusion states for TcpP-PAmC (three circles with colors as in panel c and with average single-molecule diffusion coefficient, D, indicated in μm^2/s), the average probabilities of transitioning between mobility states at each step are indicated as arrows between those two circles, and the circle areas are proportional to the weight fractions. Low-significance transition probabilities less than 4% are not displayed; for instance, the probability of TcpP-PAmC molecules transitioning from the fast diffusion state to the slow diffusion state is 1%. Numbers above the arrows indicate the probability of transition.

mutant (Fig. 3.2A). *toxT* expression was reduced in *tcpP-PAmCherry toxTpro*Δ(-112−+1) but not in *tcpP-PAmCherry toxTpro*Δ(-55−+1) Fig. 3.4). It is possible that the *toxTpro*Δ(-55−+1)* mutation causes TcpP-PAmC and ToxR to stimulate expression of a nonfunctional *toxT* mRNA. Regardless, loss of either region of the *toxTpro* results in loss of production of the TcpA virulence factor.

Relative to the wild type (Fig. 3.7), deleting both the ToxR and TcpP binding sites [*toxTpro*Δ(-112−+1)] reduces the percentage of slow-diffusing TcpP-PAmC to very low levels (7%; Fig. 3.8b). Thus, TcpP-PAmC in the slow diffusion state requires *toxTpro*; therefore, we propose molecules in this state are bound to *toxTpro*. On the other hand, loss of the TcpP binding site alone [*toxTpro*Δ(-55−+1)] reduces the percentage of slow TcpP-PAmC molecules only subtly (from 43% to 34%; Fig. 3.8d). This result is consistent with earlier observations demonstrating that association with ToxR can restore the function of TcpP variants otherwise unable to bind the *toxTpro* [7, 23].

Furthermore, our single-step analysis of TcpP-PAmC in the *toxTpro*Δ(-112−+1) cells indicates five distinct TcpP-PAmC diffusion states, an increase from three states in the wild type (Fig. 3.8b). In particular, the percentage of TcpP-PAmC molecules within the intermediate state overall increased (48% to 78%), but our analysis showed that these moderate moving molecules in fact cluster into three distinct substates (yellow, light orange, and orange in Fig. 3.8b). These intermediate TcpP-PAmC diffusion substates appear when TcpP-PAmC is unable to associate with the *toxTpro*. Though large-scale changes in the chromosome structure following the promoter deletion may play a role, these intermediate TcpP-PAmC diffusion substates may represent true biochemical interactions that are too short-lived to precisely distinguish and identify due to our current time resolution of 40 ms/acquisition. Further investigation is required to understand the specific biological roles of these substates, but indeed as discussed below, we detect these intermediate substates in all the other mutants studied here (Fig. 3.9 and Fig. 3.12).
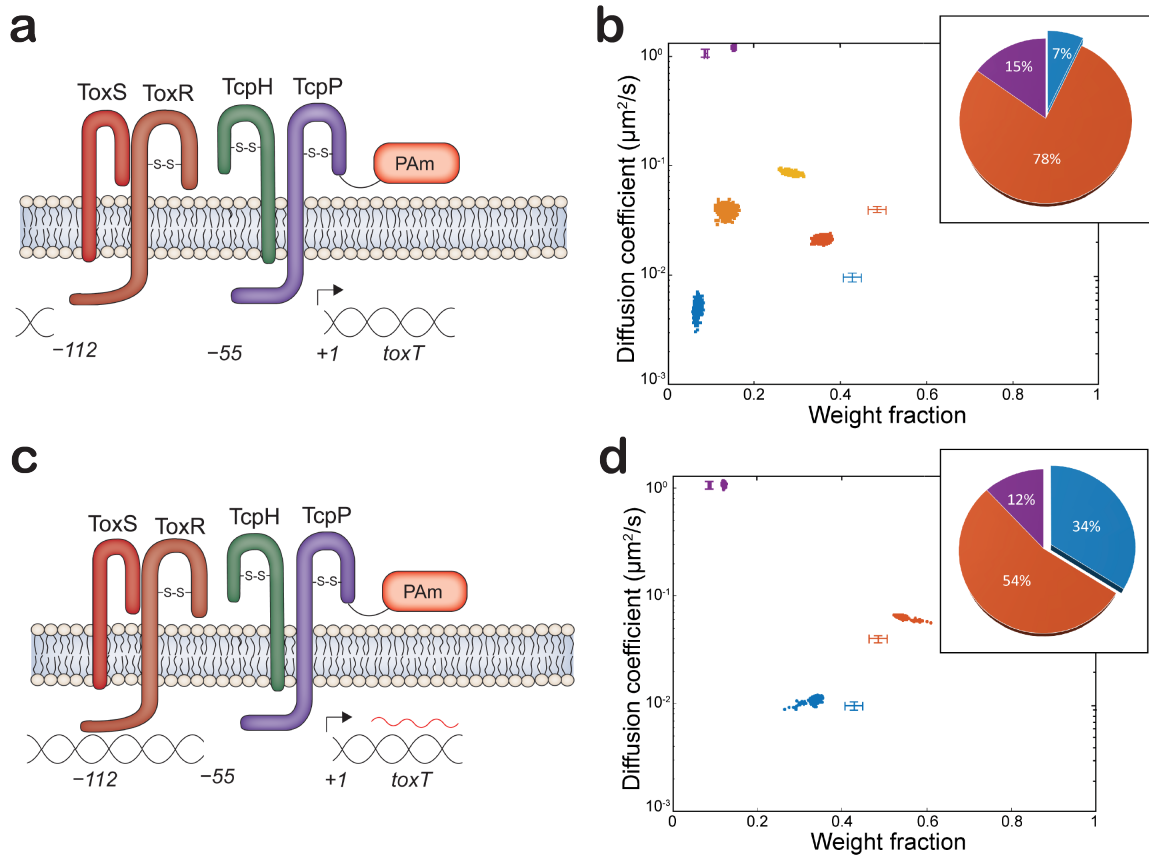
Figure 3.8: TcpP-PAmCherry diffusion dynamics within live *V. cholerae* cells containing mutated regions of the *toxTpro*. (a and c) Model of *toxTpro* mutations in *tcpP-PAmC toxTpro*Δ(-112–+1), and *tcpP-PAmC toxTpro*Δ(-55–+1), respectively. (b and d) Average single-molecule diffusion coefficients and weight fraction estimates for TcpP-PAmC in live *V. cholerae tcpP-PAmCherry toxTpro*Δ(-112–+1) (b) and *V. cholerae tcpP-PAmCherry toxTpro*Δ(-55–+1) (d) grown under virulence-inducing conditions. Single-step analysis identifies five and three distinct diffusion states (fast [purple], intermediate [orange, light orange, and yellow], and slow [blue], respectively). Each point represents the average single-molecule diffusion coefficient versus weight fraction of TcpP-PAmC molecules in each distinct mobility state at each saved iteration of the Bayesian algorithm after convergence. The data set contains 104,341 steps from 21,274 trajectories for panel b and 75,841 steps from 11,624 trajectories for panel d. The data for TcpP-PAmC diffusion in wild-type *V. cholerae* cells (Fig. 3.7c) are provided for reference (cross-hairs). (Insets) Percentage (weight fraction) of TcpP-PAmC in each diffusion state. Colors as in panel.

45

3.3.3 ToxR Promotes TcpP-PAmCherry Association with the Slow and Fast Diffusion States

ToxR is a critical regulator of *toxT* expression through its role supporting TcpP interaction with the *toxTpro* [7, 23, 85]. Prior studies have shown that TcpP and ToxR interact in response to low oxygen concentrations, and ToxR antagonizes H-NS from the *toxTpro* [7, 127, 128]. Several models for TcpP-mediated *toxT* transcription implicate ToxR in recruitment of TcpP molecules to the *toxTpro* [7, 23, 26, 27, 85, 88]. Another model invokes "promoter alteration" to suggest that ToxR promotes TcpP-*toxTpro* interaction by displacing the histone-like protein (H-NS) and altering DNA topology rather than recruiting TcpP molecules to the *toxTpro* [88].

To examine the role of ToxR in the motion and localization of TcpP-PAmC, we deleted *toxR*, as well as *toxS*, the gene encoding the ToxR accessory protein, in both the TcpP-PAmC and the *tcpP-PAmCherry toxTpro*Δ(-55−+1) backgrounds, resulting in *tcpP-PAmCherry* Δ*toxRS* and *tcpP-PAmCherry* Δ*toxRS toxTpro*Δ(-55−+1) genotypes. We found that *tcpP-PAmCherry* Δ*toxRS* and *tcpP-PAmCherry* Δ*toxRS toxTpro* Δ(-55−+1) cells could activate *toxT* transcription, but only *tcpP-PAmCherry* Δ*toxRS* supported virulence factor production Fig. 3.2A and B and Figure Fig. 3.4). Complementation of *tcpP-PAmCherry* Δ*toxRS* with *toxR* did not change overall levels of TcpA (Fig. 3.10). Complementation of *tcpP-PAmCherry* Δ*toxRS toxTpro*Δ(-55−+1) with ToxR did not restore TcpA to WT levels (Fig. 3.10). These data show that TcpP-PAmC can stimulate *toxT* expression and bind to the *toxTpro* independent of ToxR. WT TcpP can stimulate *toxT* expression independent of ToxR, but only upon TcpP overexpression [7, 23]. Due to reduced sensitivity of TcpP-PAmC to RIP, we measure higher levels of TcpP-PAmC relative to TcpP (Fig. 3.2a). This observation suggests that cooperativity between ToxR and TcpP is necessary only when levels of TcpP are low (i.e., when TcpP is sensitive to RIP).

The percentage of slowly diffusing TcpP-PAmC molecules depends on *toxRS*, as deleting *toxRS* reduces this population in *tcpP-PAmCherry*Δ*toxRS* from 43% to 20% (Fig. 3.9b).

This *toxRS* dependence is maintained even in the absence of the TcpP binding site within the *toxTpro*; the slow population in *tcpP-PAmCherry ΔtoxRS toxTpro*Δ(-55−+1) is reduced to 8% from 34% in *tcpP-PAmCherry toxTpro*Δ(-55−+1) (Fig. 3.9d). Indeed, the TcpP-PAmC dynamics are very similar for *tcpP-PAmCherry toxTpro*Δ(-112−+1) (Fig. 3.8b) and *tcpP-PAmCherry ΔtoxRS toxTpro*Δ(-55−+1) (Fig. 3.9d). The major difference between TcpP-PAmC diffusion dynamics is the loss of the light orange intermediate diffusion substate in *tcpP-PAmCherry ΔtoxRS toxTpro*Δ(-55−+1) (Fig. 3.9d). These data indicate that, in addition to the slow diffusion state, the presence of ToxR is critical for TcpP-PAmC molecules to exist in one of the intermediate substate diffusion states (i.e., the light orange diffusion state).
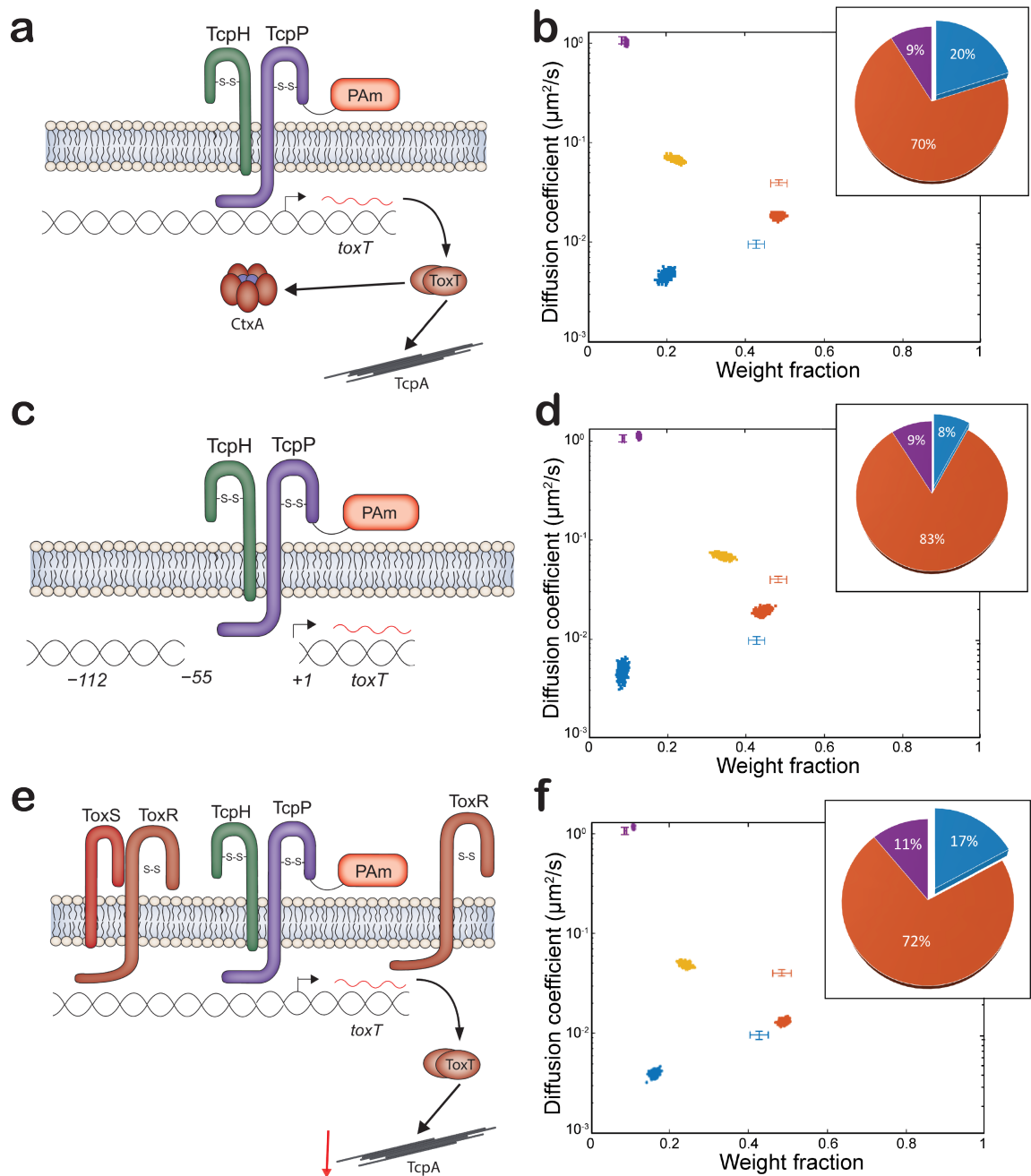
Figure 3.9: TcpP-PAmCherry diffusion dynamics within live *V. cholerae* cells lacking ToxRS and regions of the *toxTpro*. Caption on next page.

Figure 3.9: (a, c, and e) Model of *tcpP-PAmCherry ΔtoxRS, tcpP-PAmCherry ΔtoxRS toxTpro Δ(-55−+1),* and *tcpP-PAmCherry pMMB66EH-toxR,* respectively. (b, d, and f) Average single-molecule diffusion coefficients and weight fraction estimates for TcpP-PAmC in live *V. cholerae tcpP-PAmCherry ΔtoxRS* (b), *V. cholerae tcpP-PAmCherry Δ toxRS toxTproΔ(-55-+1)* (d), and *tcpP-PAmCherry pMMB66eh-toxR* (f) grown under virulence-inducing conditions. *tcpP-PAmCherry pMMB66eh-toxR* was grown in the presence of 1 mM IPTG. Single-step analysis identifies four distinct diffusion states (fast [purple], intermediate [yellow and orange], and slow [blue], respectively). Each point represents the average single-molecule diffusion coefficient versus weight fraction of TcpP-PAmC molecules in each distinct mobility state at each saved iteration of the Bayesian algorithm after convergence. The data set contains 80,005 steps from 11,069 trajectories for panel b, 58,577 steps from 11,314 trajectories for panel d, and 134,071 steps from 19,509 trajectories for panel f. The data for TcpP-PAmC diffusion in WT *V. cholerae* cells (Fig. 3.7c) are provided for reference (cross-hairs). (Inset) Percentage (weight fraction) of TcpP-PAmC in each diffusion state. Colors as in panel.
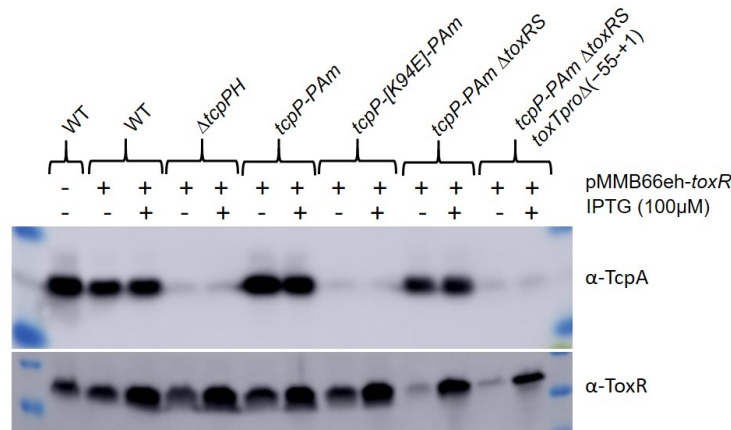
Figure 3.10: Complementation and overexpression of ToxR from the pMMB66EH plasmid. Western blot assays of cellular lysates collected after growth under virulence-inducing conditions for 6 h with or without IPTG; see Materials and Methods for primary antibody dilution. ToxR does not stimulate TcpA production without TcpPH, and ToxR cannot complement TcpPK94E-PAmC or *toxTproΔ*(-55−+1). Low levels of ToxR were detected in *tcpP-PAmCherry ΔtoxRS* and *tcpP-PAmCherry ΔtoxRS toxTproΔ*(-55−+1) without IPTG, likely due to leaky expression of *toxRS* at the IPTG promoter. Multiple copies of the *lac promoter* are known to result in leaky expression due to insufficient levels of LacI [120, 127]

As shown in Fig. 3.7d, we found that TcpP-PAmC molecules do not freely transition between all the diffusion states: the intermediate diffusion state is an important diffusion state for TcpP-PAmC molecules to transition between the fast and the slow diffusion
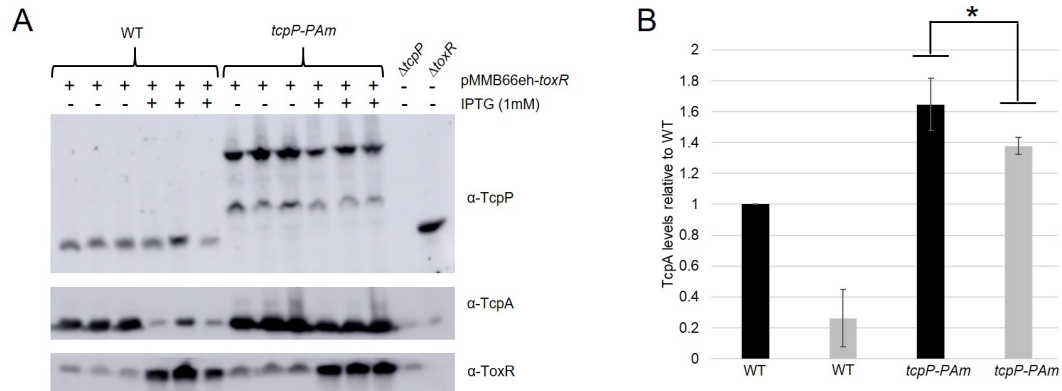
Figure 3.11: ToxR overexpression reduces virulence factor production. (A) Western blot assays of cell lysates; three biological replicates, collected after 6 h of virulence-inducing conditions with or without IPTG. (B) Densitometry analysis of the TcpA Western blot in panel A. ImageJ was used to perform the densitometry analysis. Black bars, without isopropyl-β-D-thiogalactopyranoside (IPTG); gray bars, with IPTG. Error bars represent standard deviation. One-tailed Student's t test was used to determine statistical significance. * indicates a P value of 0.029.

states. Since the ToxR-TcpP interaction is proposed to enable TcpP to associate with the transcription complex at *toxTpro* [7, 23], we reasoned that ToxR is responsible for the preferred intermediate-to-slow-state transition of TcpP-PAmC. However, in the Δ*toxRS* mutant (Fig. 3.9b) as in the wild type (Fig. 3.7c), only TcpP-PAmC molecules in the slowest of the intermediate diffusion substates were likely to transition to the slow diffusion state (orange and blue diffusion states, respectively; Fig. 3.13b). These transition probabilities suggest that ToxR is not responsible for the restricted transition of TcpP-PAmC between the slow and fast diffusion states. Furthermore, the absence of ToxR reduced the probability of TcpP-PAmC entering the fast diffusion state and increased the probability of TcpP-PAmC leaving the fast diffusion state (Fig. 3.7d and Fig. 3.13b). Taken together, these data indicated that ToxR sequesters a portion of the total TcpP-PAmC population away from the *toxTpro*. We reasoned that increased levels of ToxR might sequester TcpP molecules to an inactive state (represented by the intermediate diffusion state). To test this
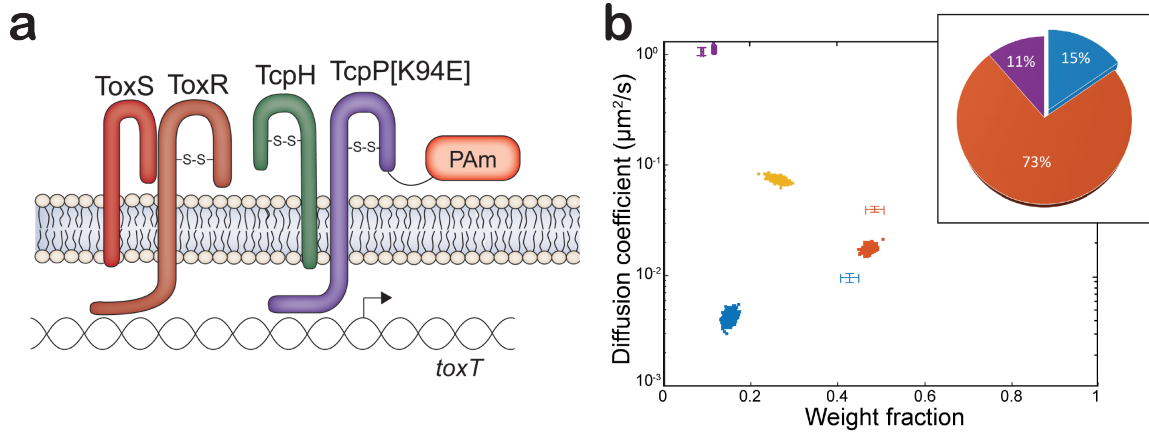
Figure 3.12: TcpP[K94E]-PAmCherry diffusion dynamics within live *V. cholerae* cells. (a) Model of *tcpP-[K94E]-PAmCherry*. (b) Diffusion dynamics of a DNA binding-deficient TcpP-PAmC variant within live *V. cholerae* cells. Average single-molecule diffusion coefficients and weight fraction estimates for TcpP-[K94E]-PAmCherry in live *V. cholerae tcpP-[K94E]-PAmCherry* grown under virulence-inducing conditions. Single-step analysis identifies four distinct diffusion states (fast [purple], intermediate [yellow and orange], and slow [blue], respectively). Each point represents the average single-molecule diffusion coefficient versus weight fraction of TcpP-[K94E]-PAmC molecules in each distinct mobility state at each saved iteration of the Bayesian algorithm after convergence. The data set contains 52,565 steps from 8,056 trajectories. The data for TcpP-PAmC diffusion in WT *V. cholerae* cells (Fig. 3.7c) are provided for reference (cross-hairs). (Inset) Percentage (weight fraction) of TcpP-[K94E]-PAmC in each diffusion state. Colors as in panel.

hypothesis, we overexpressed ToxR in a *tcpP-PAmCherry* background and quantified virulence factor expression (i.e., TcpA) (Fig. 3.11). We found that elevated ToxR levels reduced virulence factor levels in both WT and *tcpP-PAmCherry* cells. Furthermore, overexpression of ToxR also decreased the percentage of TcpP-PAmC in the slow diffusion state (17% versus 43%) and resulted in the formation of a subintermediate diffusion state, similar to *tcpP-PAmCherry* Δ*toxRS* (Fig. 3.9f). These data suggest that elevated levels of ToxR can repress *toxT* expression by reducing the percentage of TcpP molecules entering the slow diffusion state.

3.3.4 Mutation of the TcpP Helix-turn-helix Domain Reduces the Percentage of Slowly Diffusing TcpP-PAmCherry

Based on results shown in Fig. 3.7c, we proposed that TcpP-PAmC molecules in the slow diffusion state are bound to *toxTpro*, and we found that removing the *toxTpro* binding sites (Fig. 3.8) or eliminating *toxR* (Fig. 3.9) significantly reduces this bound state population. Previous studies demonstrated that TcpP does not require DNA binding capability to activate *toxT* expression if ToxR is present [7, 23]. To examine this finding further by SMT, we used a *tcpP-PAmCherry* allele with a mutation (K94E) that inhibits TcpP from binding to the *toxTpro* [7]. This mutation results in greatly reduced *toxT* expression and TcpA levels (Fig. 3.2A and Figure Fig. 3.4). The levels of TcpP[K94E]-PAmC are elevated compared with TcpP-PAmC (Figure Fig. 3.2A), consistent with earlier evidence that the K94E substitution increases TcpP stability [7]. In addition to TcpP[K94E]-PAmC being unable to stimulate *toxT* expression, a lower percentage of TcpP[K94E]-PAmC molecules are detected in the slowest-diffusing state than for TcpP-PAmC (15% versus 43%; Fig. 3.12b). Furthermore, TcpP[K94E]-PAmC molecules have an additional intermediate diffusion substate, similar to both *tcpP-PAmCherry ΔtoxRS* and *tcpP-PAmCherry ΔtoxRS toxTpro* Δ(-55−+1) (Fig. 3.12b).
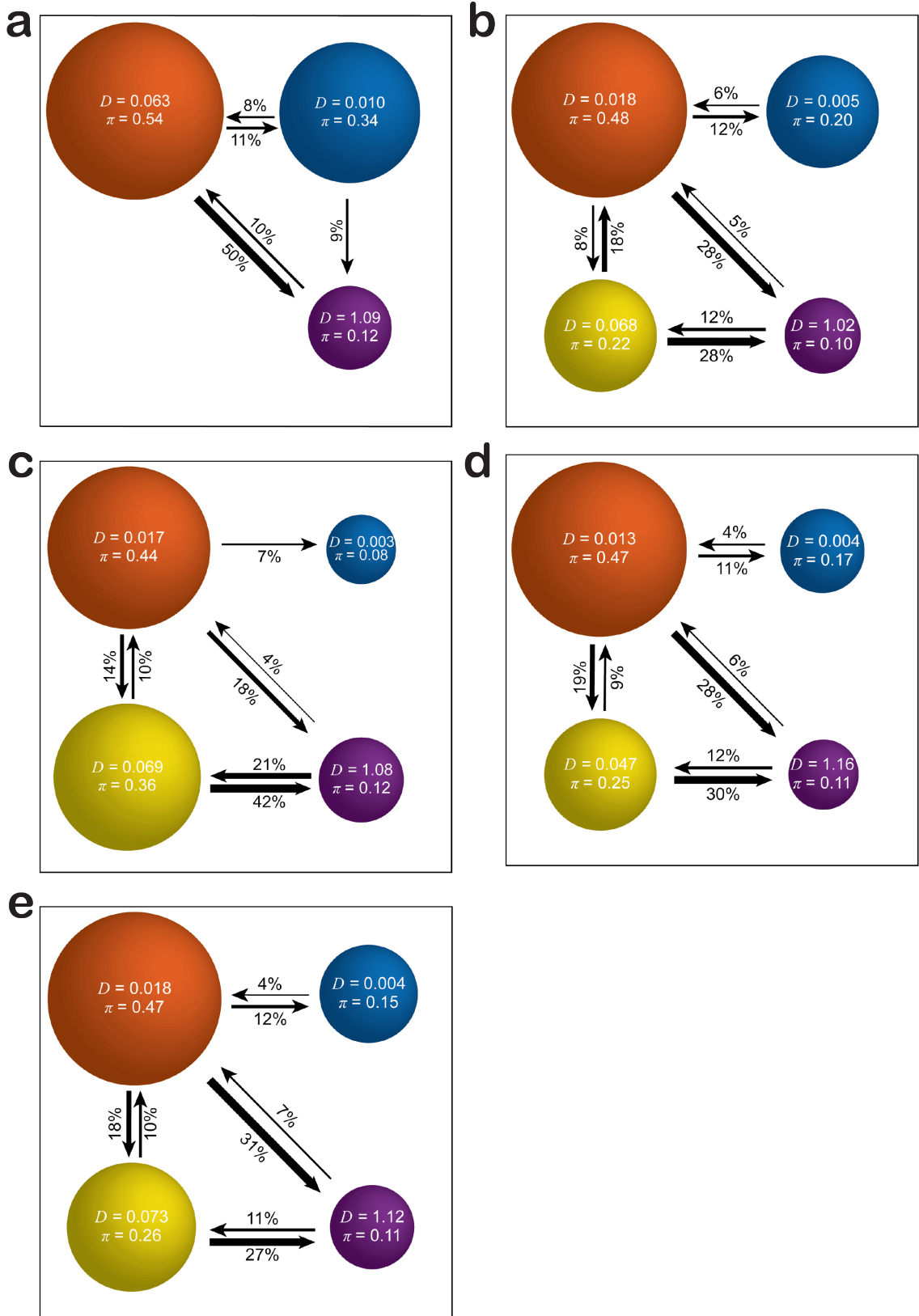
Figure 3.13: TcpP-PAmCherry transition plots. Caption on next page.

Figure 3.13: Based on the identification of distinct diffusion states for TcpP-PAmC (circles with colors as in Fig. 3.7c and with average single-molecule diffusion coefficient, D, indicated in $\mu m^2/s$), the average probabilities of transitioning between mobility states at each step are indicated as arrows between those two circles, and the circle areas are proportional to the weight fractions. Low-significance transition probabilities less than 4% are not displayed. Numbers above the arrows indicate the probability of transition. (a) *V. cholerae tcpP-PAmCherry toxTpro*Δ*(-55−+1)*, corresponding to Fig. 3.8d. (b) *V. cholerae tcpP-PAmCherry* Δ*toxRS*, corresponding to Fig. 3.9b. (c) *V. cholerae tcpP-PAmCherry* Δ*toxRS toxTpro*Δ*(-55−+1)*, corresponding to Fig. 3.9d. (d) *V. cholerae tcpP-PAmCherry pMMB66eh-toxR*, corresponding to Fig. 3.9f. (e) *V. cholerae tcpP-K94E-PAmCherry*, corresponding to Fig. 3.12b.

3.4 Conclusions

How MLTAs find their target sequences from the membrane represents a major gap in knowledge. Here, we started to address this by investigating single-molecule dynamics of TcpP-PAmC. Taken together with previous work, the data presented here demonstrate that TcpP-PAmC molecules diffuse in at least three distinct biophysical states (fast, intermediate, and slow diffusion) but do not freely transition between all diffusion states [38]. We hypothesized that each of these biochemical states have distinct biological roles. Specifically, we hypothesized that the slow diffusion state represented TcpP-PAmC molecules interacting with the *toxTpro*. To test this hypothesis, we made targeted deletions to the *toxTpro* and of *toxRS*, and we mutated the TcpP DNA binding domain (K94E). Our biophysical measurements of these mutations support the hypothesis that the slow diffusion state is occupied by TcpP-PAmC molecules interacting specifically with DNA at *toxTpro*. Additionally, we observed that TcpP-PAmC molecules only transition to the slow diffusion state from the intermediate diffusion state and that ToxR is not responsible for this transition specificity. These data support a modified promoter alteration model [88] in which ToxR binds to the distal region of the *toxTpro* to promote TcpP binding to the proximal region of the *toxTpro* or, in the absence of its binding site, ToxR directly interacts with TcpP to stimulate *toxT* expression. Our data do not suggest that ToxR directs or recruits TcpP to the *toxTpro*.

While ToxR is critical for TcpP to stimulate *toxT* expression [7,23,87], our data demonstrate that TcpP-PAmC can support *toxT* expression and virulence factor production without ToxR, which may be a consequence of the greater stability of TcpP-PAmC than of native TcpP (see Fig. 3.2A and Fig. 3.4). Moreover, our single-molecule imaging finds a higher percentage of the TcpP-PAmC molecules in the slow diffusion state in *tcpP-PAmCherry* Δ*toxRS* cells than in *tcpP-PAmCherry* Δ*toxRS toxTpro*Δ(-55−+1) cells (Fig. 3.9). In addition, prior DNase I footprinting experiments have demonstrated that in cells lacking *toxR* TcpP protects a larger region of the *toxTpro(-100 to -32)*, i.e., TcpP protects most of the ToxR binding and TcpP binding sites in the Δ*toxRS* mutant [23]. Taken together, these results indicate that (i) ToxR is not essential for TcpP to locate the *toxTpro* and (ii) TcpP is able to interact with the *toxTpro* independent of ToxR. In addition, our data show that Δ*toxRS* reduces the percentage of DNA-bound TcpP-PAmC but does not decrease the probability of TcpP-PAmC molecules transitioning from the intermediate state to the bound state (Fig. 3.9 and Fig. 3.13b). Despite a reduction in the percentage of DNA-bound TcpP-PAmC, TcpP-PAmC stimulates WT *toxT* expression independent of ToxR (Fig. 3.4). These data support the promoter alteration model [88] in which, rather than ToxR recruiting TcpP to the *toxTpro*, ToxR assists TcpP to stimulate *toxT* transcription once TcpP independently associates with the *toxTpro*. Counterintuitively, in the absence of ToxRS TcpP-PAmC molecules have a lower probability of exiting the slow diffusion state (Fig. 3.13b). Given that RIP of TcpP-PAmC impedes our ability to image TcpP-PAmC, these data suggest that TcpP-PAmC molecules might be sensitive to RIP while interacting with the *toxTpro* and that ToxRS may inhibit RIP of TcpP while interacting with the *toxTpro*. If this is the case, given that we are unable to image TcpP-PAmC molecules that are sensitive to RIP, it might explain why we observe a lower percentage of TcpP-PAmC molecules in the slow diffusion state and yet we observe WT *toxT* expression in the absence of ToxRS. However, future experiments are required to determine if ToxRS inhibits RIP of TcpP while interacting with the *toxTpro*.

Under certain conditions, ToxR can negatively influence *toxT* expression. In response to stationary-phase accumulation of the cyclic dipeptide cyclic phenylalanine-proline (cyc-Phe-Pro), ToxR stimulates production of LeuO, resulting in down regulation of the *tcpP* regulator aphA [119, 120]. Our data suggest that ToxR can also reduce *toxT* expression by influencing TcpP-PAmC single-molecule dynamics (Fig. 3.13b). Deletion of *toxRS* reduces the overall probability of TcpP-PAmC molecules transitioning between the intermediate and fast diffusion states (Fig. 3.13b). Moreover, elevated levels of ToxR reduce both the percentage of TcpP-PAmC in the slow diffusion state and virulence factor production (Fig. 3.9f and Fig. 3.11), suggesting that ToxR can antagonize *toxT*expression by promoting transition of TcpP molecules to the fast or subintermediate diffusion states. A similar phenotype has been reported previously [23]. Lastly, prior electrophoretic mobility shift assays also indicate that ToxR can sequester TcpP from the *toxTpro*. In Δ*toxRS* cells TcpP is able to bind to the *toxTpro* -73−+45 (*toxTpro* lacking the ToxR binding region), but not in the presence of ToxR molecules [23]. It remains unclear how ToxR sequesters TcpP-PAmC molecules from the slow diffusion state. However, we hypothesize that ToxR promotes TcpP molecules to transition away from the slow diffusion state to prevent aberrant *toxT*expression. Follow-up experiments are required to test this hypothesis.

Currently, the biological roles of the intermediate diffusion states (or intermediate diffusion substates) are unclear, but the intermediate states are certainly important, as TcpP molecules transition to the *toxTpro*-bound state from them. There is nearly a 10-fold difference in diffusion coefficients between the slow and intermediate diffusion states (0.006 μm^2/s versus 0.044 μm^2/s, respectively; Fig. 3.7c). This difference cannot be explained by dimerization or interaction of ToxR and TcpP-PAmC alone: the mobility of membrane-localized proteins scales linearly with the number of transmembrane helices, such that increasing the number of transmembrane helices via dimerization from one to two would reduce the diffusion coefficient only by a factor of two [121]. One possibility is that TcpP-PAmC molecules undergo fast diffusion in less protein-dense areas of the

cytoplasmic membrane relative to TcpP-PAmC molecules undergoing intermediate diffusion. Prior single-molecule analysis of 209 membrane-localized proteins in *Bacillus subtilis* (*B. subtilis*) revealed that only 6% of all membrane proteins imaged were homogeneously distributed throughout the cytoplasmic membrane [129]. Heterogeneous distribution of membrane-localized proteins in *B. subtilis* suggests that similar distribution of membrane-localized proteins in *V. cholerae* can occur. It remains unclear why the vast majority of these membrane-localized proteins in *B. subtilis* have heterogeneous diffusion dynamics. One possibility is that these membrane-localized proteins have different preferences for lipid-ordered and lipid-disordered membrane domains. Prior studies have demonstrated that transmembrane domain properties (e.g., surface area, length, and posttranslational modifications) are major factors in determining lipid-ordered or lipid-disordered membrane domain preference [130]. We are currently exploring if lipid-ordered and lipid-disordered membrane domains influence diffusion dynamics of TcpP molecules within the fast and intermediate diffusion states.

Alternatively, it is possible that the diffusion coefficients of TcpP-PAmC molecules in the intermediate state are undergoing nonspecific interactions with DNA whereas the slowest TcpP-PAmC molecules are specifically bound at *toxTpro*. Our data show that there are some slow-moving TcpP-PAmC molecules when major regions of the *toxTpro* are deleted or when key residues within the DNA binding domain of TcpP are mutated (i.e., *tcpP[K94E]-PAmCherry*; Fig. 3.8 and Fig. 3.12). When considering our alternative model of nonspecific DNA binding by TcpP, our data suggest two possibilities: (i) TcpP-PAmC molecules in the slow diffusion state represent TcpP molecules that make both specific and nonspecific interactions with DNA or (ii) TcpP-PAmC molecules in the slow diffusion state interact specifically with non-*toxTpro* DNA (i.e., TcpP regulates additional genes). Several genes appear to have altered gene expression upon deletion of *tcpPH* [131]. However, these experiments have yet to be replicated. Thus, future experiments would be required to test these hypotheses.

These results provide deep insights that further expand the model of cooperativity between ToxR and TcpP-PAmC. Our data demonstrate that ToxR assists TcpP to associate with the *toxTpro* even in the absence of the TcpP binding site, further supporting the established model of cooperativity between TcpP and ToxR. The data also show that TcpP can locate the *toxTpro*, interact with the *toxTpro*, and stimulate *toxT* expression independent of ToxR. This supports the promoter alteration model in which TcpP molecules independently associate with the *toxTpro* while ToxR enhances this association by altering *toxTpro* topology to stimulate *toxT* transcription. In addition to independently associating with the *toxTpro*, these data show that ToxR promotes transition of TcpP molecules to the fast and subintermediate diffusion states, shifting the equilibrium of TcpP molecules away from the *toxTpro*. The mechanism by which ToxR promotes transition of TcpP molecules away from the slow diffusion state is currently unclear but will be the subject of future investigation. Given that *toxT* expression is highly regulated, we speculate that sequestration of TcpP molecules from the *toxTpro* is yet another mechanism to fine-tune *toxT* expression. It is probable that other MLTAs, found in both Gram-negative and Gram-positive bacteria, have similar biophysical properties (Fig. 3.1). Continued exploration of MLTAs biophysical properties could be leveraged to develop alternative strategies to inhibit MLTAs to treat bacterial infections without exacerbating the global antibiotic resistance crisis.

Development of Chitosan Coverslip Coatings for Single-molecule Fluorescence Imaging in Live Bacteria Cells during Real-time Environment Perturbations

4.1   Introduction

Behavior adaptation to environmental changes is vital to bacterial survival and proliferation. Bacteria have developed a variety of mechanisms to adapt to changes in the environment [5]. Environmental signaling triggers changes in growth rate, cell secretions such as toxin and quorum-sensing agents, and nutrient storage [6–9]. Insight into the signaling pathways of these cells during environmental perturbations will elucidate key

functions of the bacteria species and lead to the development of new therapies and small molecule treatments for disease [32, 132].

Cholera is a diarrheal disease caused by the Gram-negative bacterium *Vibrio cholerae* (*V. cholerae*) and leads to ~100,000 deaths annually [13, 133]. To reach the surface of intestinal epithelial cells, proliferate, and cause disease, *V. cholerae* regulates the production of virulence factors such as the cholera toxin and toxin co-regulated pilus [11, 77, 78, 81, 82, 134, 135]. The membrane-localized transcription regulators TcpP and ToxR play key roles in this regulation pathway by controlling expression of *toxT*, the product of which directly controls expression of cholera toxin and the toxin co-regulated pilus; however, the precise mechanism remains unclear [23–27]. Recently, we expanded our understanding by quantifying the interactions of TcpP and ToxR with the *toxT* promoter (*toxTpro*) with live-cell single-molecule imaging and tracking [1]. These experiments determined the cooperativity between TcpP and ToxR under steady-state conditions, highlighting the complexity of their roles in regulating virulence factor production.

Environmental factors dramatically change the production of toxin by *V. cholerae* [6, 28–31]. This bacterium exists as a free-living marine microorganisms and it experiences a major shift in extracellular conditions upon transitioning from the marine environment to the human gastrointestinal tract [136, 137]. However, how this rapid change in conditions affects the subcellular dynamics of TcpP and its ability to identify and interact with the *toxTpro* has not been studied. To accurately localize and track single molecules in live bacteria cells, the cells must be immobilized. To immobilize the cells while maintaining their access to important nutrients, cells are typically sandwiched between an agarose gel pad and a glass coverslip. However, this confined geometry does not allow for changes to the cell environment after the initial sample preparation. Thus, conventional sample preparation methods are incompatible with registering the effect of real-time perturbations during live-cell single-molecule imaging and tracking.

Recent developments in slide coatings—have enabled the ability to make real-time

perturbations during single-molecule imaging experiments while maintaining the physiology of the bacterial cell. Appropriately coated microscope coverslips immobilize bacteria cells without impeding access for real-time exchange of the cell media. Recently, preparation of bacteria on chitosan-coated slides has been shown to immobilize bacteria cells by charge-charge interactions with the acetylated side chains without altering cell growth or physiology [45, 46]. Chitosan slide coatings therefore represents a significant advantage relative to other slide coatings like poly-L-lysine, which can immobilize bacteria cells but which has been shown to increase the cell area and induce division defects [47–49]. Fluorescence imaging of bacteria mounted on chitosan-coated coverslips has been explored, but single molecules have not been imaged or tracked within bacteria cells immobilized in this way. While chitosan-coated coverslips offer a simple solution to change the environment during imaging, microfluidic devices would allow for more control VII.

In this chapter, I present a sample preparation method capable of immobilizing *V. cholerae* cells without altering the cell's natural functions and which allow for real-time environmental perturbations during single-molecule imaging. I localize and track single TcpP-PAmCherry (TcpP-PAmC) molecules in live *V. cholerae* cells immobilized on chitosan-coated coverslips and show that these dynamics match previously published results with traditional sample preparation.

4.2 Materials and Methods

4.2.1 Bacterial Strains and Growth Conditions

The three *V. cholerae* strains used here were all in the O395 classical biotype background. Strains used in this study were wild-type (WT), *tcpP-PAmCherry*, and *tcpP-PAmCherry* pMMB66EH-*toxR* Δ*toxR*. All construct development was previously published [1]. *V. cholerae* strains were grown overnight at 37 ℃ on lysogeny broth (LB) plates containing streptomycin (100μg mL^{-1}, streptomycin (strp)). Then, an individual colony was picked

and grown overnight in LB + strp medium under indicated conditions (virulence-inducing or non-virulence inducing conditions). Overnight *V. cholerae* cell cultures were diluted into LB + strp medium and grown until they reached mid-log phase. Cultures were then centrifuged at 5000 rpm for 1.5 min and resuspended in half the volume of M9 minimal medium + strp with 0.4% glycerol. This concentrated cell culture method was used for all traditional and chitosan slide coating sample preparation described for all growth conditions.

Two growth conditions were used for this study: virulence-inducing conditions (medium pH adjusted to 6.0 (± 0.05) with 1 M hydrochloric acid; temperature set to 30 ℃) and non-virulence inducing conditions (medium pH adjusted to 8.0 (±0.05) with 1 M sodium hydroxide; temperature set to 37 ℃).

4.2.2 Live/Dead Cell Assay

Using the BacLight Bacterial Viability Kit L7007, 0.25 μL of Component A and 0.25 μL of Component B were added to 500 μL of concentrated wild-type *V. cholerae* cells in M9 minimal medium. Cells were immobilized on chitosan-coated coverslips or on agarose pads according to sample preparation protocol. Cells were imaged at room temperature using an Olympus IX71 inverted epifluorescence microscope with a 100X 1.40-numerical aperture (NA) oil-immersion objective, a 488-nm laser (Coherent-Sapphire 488-50; 2.5 W/cm^2) for fluorescence excitation of SYTO 9 (all cells), and a coaligned 561-nm laser (Coherent-Sapphire 561-50; 2.5 W/cm^2) for fluorescence excitation of Propidium iodide (dead cells). Fluorescence emission was filtered with appropriate filters and captured on a 512- by 512-pixel Photometrics Evolve electron multiplying charged-couple detector (EMCCD) camera. Manual shutters were used to block the lasers to image at one wavelength at a time. Images were collected continuously every 40 ms, and acquisitions lasted 2 min for each wavelength. Gridded coverslips (ibidi) were used to measure the same cells at each time point. Three biological replicates of at least 35 cells were performed. Image

intensities were analyzed using Fiji Image J2. The same intensity thresholds were applied to every image regardless of sample preparation or collection day. Cells detected in the phase-contrast, 561-nm, and 488-nm channels were counted as dead; cells appearing in only the phase-contrast and 488-nm channels were counted as alive. Cells appearing in the phase-contrast and/or 561-nm channels but not the 488-nm channels were not counted.

4.2.3   Single-molecule Microscopy

A minimum of 50 cells per condition were imaged at room temperature using an Olympus IX71 inverted epifluorescence microscope with a 100X 1.40-NA oil-immersion objective, a 405-nm laser (Coherent Cube 405-100; 50 W/cm^2) for photoactivation, and a coaligned 561-nm laser (Coherent-Sapphire 561-50; 210 W/cm^2) for fluorescence excitation. Fluorescence emission was filtered with appropriate filters and captured on a 512-by 512-pixel Photometrics Evolve EMCCD camera. To prevent higher-order excitation during photoactivation, a pair of Uniblitz shutters controlled the laser beams such that samples were exposed to only one laser at a time. During imaging, the cells were given a 40-ms dose of 405-nm light every 90 s. Images were collected continuously every 40 ms, and acquisitions lasted 5 - 7 min each.

4.2.4   Data Analysis

Recorded single-molecule positions were detected and localized based on point spread function fitting using our home-built code, Single-Molecule Accurate LocaLization by LocAl Background Subtraction (SMALL-LABS) [37]. This program reduces biases due to background subtraction, increasing the accuracy of each single-molecule localization. Subsequent localizations of the same molecule were then connected into trajectories using the Hungarian algorithm [118]. All trajectories from each movie for a given condition were combined and analyzed together using the Single-Molecule Analysis by Unsupervised Gibbs sampling (SMAUG) algorithm [38]. This algorithm considers the collection of

all the steps within all the trajectories and uses a Bayesian statistical framework to infer the parameters of interest including the number of mobility states and the diffusion coefficient and weight fraction of each state. A minimum of 25,000 steps were analyzed at each condition.

4.2.5 Traditional (agarose pad) cell sample preparation

A 1.5-μL droplet of concentrated cells was placed onto an agarose pad (2% agarose (Fisher Bioreagents) in M9 + strp at appropriate pH, spread and flattened on a microscope slide) and covered with an argon plasma-etched coverslip. Imaging was performed within 1 hour of making the agarose pad and assembling the sample. For the LB experiments, the agarose pad was made with 2% agarose in LB + strp at pH 6 and cells were concentrated in LB + strp at pH 6.

4.2.6 Chitosan Coverslip Coating

Chitosan powder (low molecular weight, deacetylated chitin, Sigma Aldrich) was added to a concentration of 2.5% in 25% v/v acetic acid in water and gently shaken overnight to fully dissolve. 500 μL of the solution was pipetted onto the center of an argon plasma-etched glass coverslip followed by spinning at 2000 rpm for 5 min to form a thin film of the chitosan solution on top. Coverslips dried overnight in an enclosed container then were washed with 1% acetic acid in water then water and dried with air. Chitosan-coated coverslips were stored in an enclosed container until use for up to one month.

4.2.7 Chitosan-coated Coverslip Cell Sample Preparation

V. cholerae cells in M9 minimal media were pipetted into a hard plastic O-ring on a chitosan-coated coverslip and allowed to bind for 10 min. Media and unbound cells were removed without scratching slide surface using a pipette. Fresh M9 media was immediately added to the O-ring. The sample was placed on the microscope stage for single-

molecule microscopy. To change the cell environment, media was pipetted out and a new media environment was immediately added to the O-ring. To induce ToxR transcription in *tcpP-PAmCherry pMMB66eh-toxR Δ toxR*, M9 media + strp at pH 6 with 0.1 mM isopropyl-β-D-thiogalactopyranoside (IPTG) was added. To induce virulence conditions, M9 media + strp at pH 6 was added.

4.3   Results and Discussion

4.3.1   Translating the chitosan coverslip coating method to *Vibrio cholerae.*

Previously, *Escherichia coli* (*E. coli*) and *Klebsiella pneumoniae* (*K. pneumoniae*) cells were immobilized on a chitosan slide coating [45]. We hypothesized this coating would translate readily to another Gram-negative bacterium, *V. cholerae*. We spin-coated glass microscope coverslips with thin chitosan films with varying concentrations in water of chitosan (2 – 5%) and acetic acid (10 – 50%), and we determined by inspection of the phase contrast images that 2% chitosan in 25% acetic acid in water provided the best cell immobilization (Video S3 in Reference [2]. Thus, in all subsequent experiments, samples were prepared according to: a 2% chitosan in 25% acetic acid solution was spin-coated on a glass coverslip, then 100 μL of concentrated cells in M9 minimal medium was pipetted into an O-ring on the coverslip, cells were allowed to bind to the chitosan for 10 min, excess cells were removed by pipetting out medium, and fresh minimal medium was pipetted into the O-ring to immerse the cells (Fig. 4.1a).

We confirmed wild-type *V. cholerae* cell health on chitosan-coated slides with a Baclight live/dead cell assay: SYTO 9, which permeates all bacterial cell membranes, was excited at 488 nm to indicate all cells in the blue channel, and propidium iodide, which permeates only bacteria with damaged membranes, was excited at 561 nm to indicate dead cells in the green channel. 97% of cells on chitosan films were alive, which is comparable to 98% of cells under traditional agarose pad sample preparation (Fig. 4.2). Furthermore,
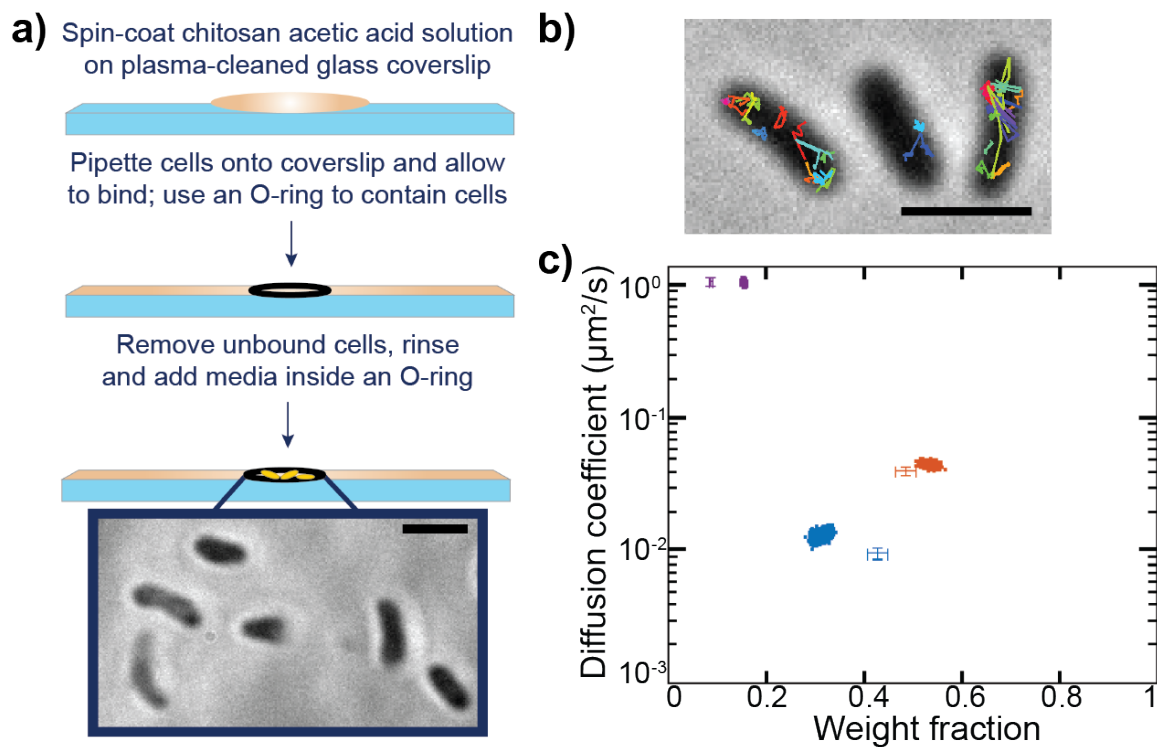
Figure 4.1: Chitosan coverslip coating preparation and evaluation. a) Chitosan coverslip coating preparation procedure. Scale bar: 2 μm. b) Representative single-molecule TcpP-PAmC trajectories overlaid on a phase-contrast image of *V. cholerae* cells on chitosan-coated coverslips. The false-colored trajectories show the diversity of motion observed. Scale bar: 2 μm. c) Average single-molecule diffusion coefficients and weight fraction estimates for TcpP-PAmC in live *V. cholerae* cells grown under virulence-inducing conditions and immobilized on chitosan-coated coverslips. Single-step analysis identifies three distinct diffusion states (fastest to slowest: purple, orange, and blue). Each point represents the average single-molecule diffusion coefficient vs. weight fraction of TcpP-PAmC molecules in each distinct mobility state at each saved iteration of the Bayesian algorithm after convergence. The data set contains 42,975 steps from 12,195 trajectories. Previously published data [1] for TcpP-PAmC diffusion in living *V. cholerae* cells grown under virulence-inducing conditions and immobilized on an agarose pad (traditional sample preparation) are provided for reference (cross-hairs).

we confirmed that *V. cholerae* cells remain alive on chitosan films after 3 hours on the microscope at room temperature with intermittent exposure to laser excitation, mimicking experiment conditions: 95% of cells on chitosan-coated coverslips were alive, which is comparable to 97% of cells under traditional sample preparation. Additionally, we confirmed that *V. cholerae* cells can grow on chitosan-coated coverslips in rich cell medium (Fig. 4.2d). These assays confirm our ability to translate chitosan-slide coatings for imaging living *V. cholerae* cells.

Single-molecule imaging and tracking has not been achieved in live cells on chitosan-coated slides before. Previously, we studied the dynamics of TcpP-PAmC in living *V. cholerae* cells to better understand the role of TcpP in regulating toxin production Chapter III [1]. Here, we measured TcpP-PAmC in living *V. cholerae* cells on chitosan-coated coverslips and found that the sensitivity required for single-molecule tracking was attainable with this sample preparation (Fig. 4.1b and Video S4 in reference [2]). We also found that the localization precision of molecules detected in cells on chitosan-coated slides was comparable to molecules in cells on traditional sample preparation with a mean localization precision of 48.5 ± 12.6 nm vs. 42.3 ± 12.3 nm for cells on chitosan-coated slides and agarose, respectively (Fig. 4.3). The cell immobilization is also robust to changes in pH and oxidative conditions (Fig. 4.4).

As previously published [1] for TcpP-PAmC in *V. cholerae* cells mounted on agarose pads (cross-hairs in Fig. 4.1c), we determined for cells grown in virulence-inducing conditions (30 °C, pH 6) and mounted on chitosan-coated coverslips that TcpP-PAmC moves in the cells in three distinct states (slow diffusion, intermediate diffusion, and fast diffusion; blue, orange, and purple scatter plots, respectively, in Fig. 4.1c) Chapter III [1]. Average diffusion coefficients are shown in Table 4.1. We previously showed that the blue state corresponds to TcpP-PAmC binding to the *toxTpro*, the orange state corresponds to TcpP-PAmC searching for its binding target, and the purple state corresponds to TcpP-PAmC freely diffusing in the membrane. We attribute the slight differences in the weight fraction of the

purple and blue groups to typical measurement and analysis error (Fig. 4.5) [38, 138].
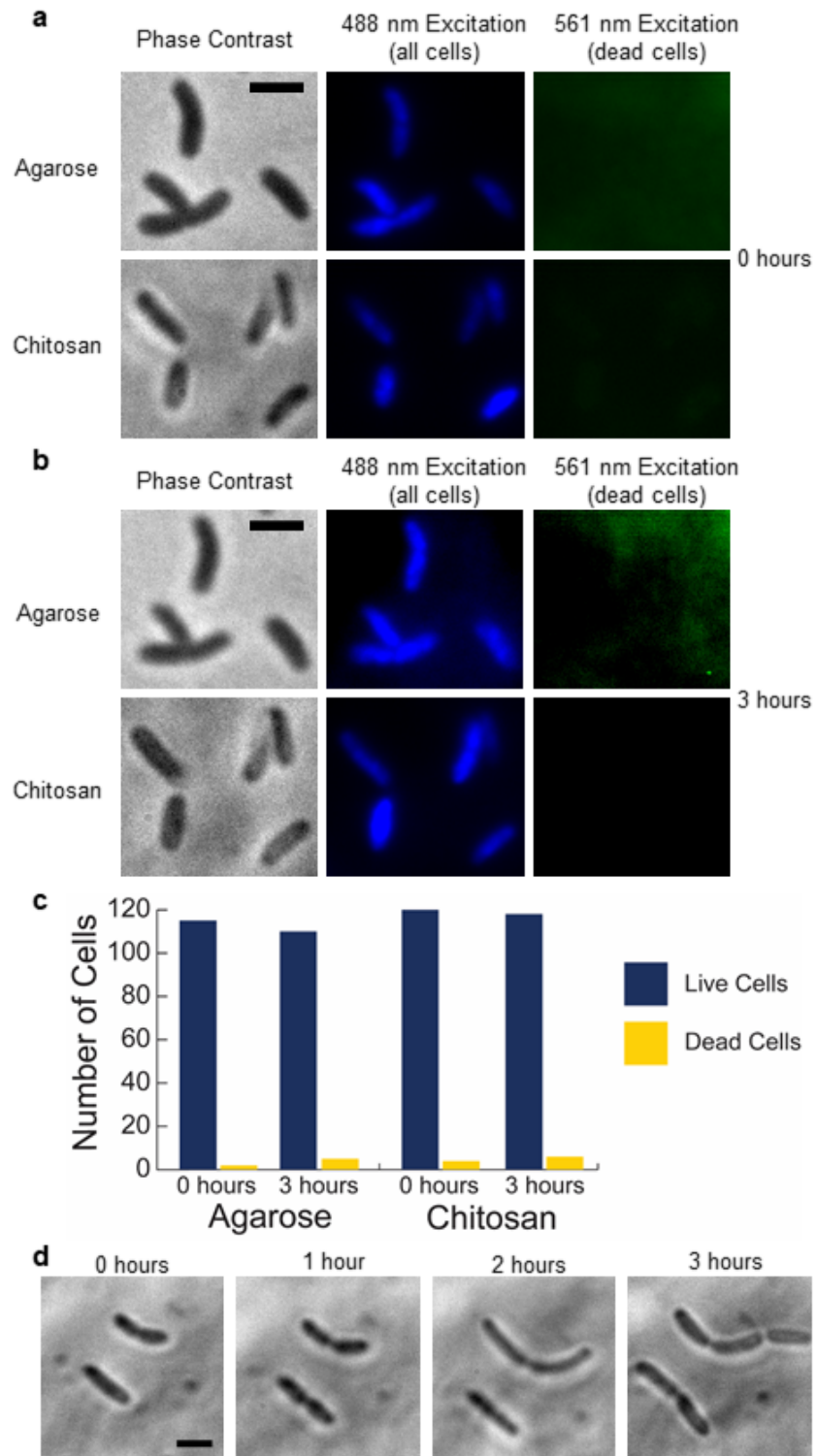
Figure 4.2: Cell health on chitosan coverslip coating. Caption on next page.

Figure 4.2: Comparing health of cells immobilized on an agarose pad (traditional sample preparation) and cells immobilized on chitosan coverslip coatings. 488-nm illumination: SYTO9 dye, which permeates all cells (false colored blue). 561-nm illumination: propidium iodine dye, which permeates only dead cells (false colored green). a) Cells directly after sample preparation. b) Cells 3 hours after sample preparation at room temperature and exposed to white light and laser exposure, consistent with single-molecule imaging experiments. Rows 'a' and 'b' show example cells that are all alive. c) Cell viability with each sample preparation at 0 and 3 hours. Dead cells: all cells detected in both the 488- and 561-nm channels. Live cells: all cells detected only in the 488-nm channel. d) Growth in LB media of cells immobilized on chitosan-coated coverslip at 0, 1, 2, and 3 hours at room temperature on the microscope. Scale bars: 2 μm.
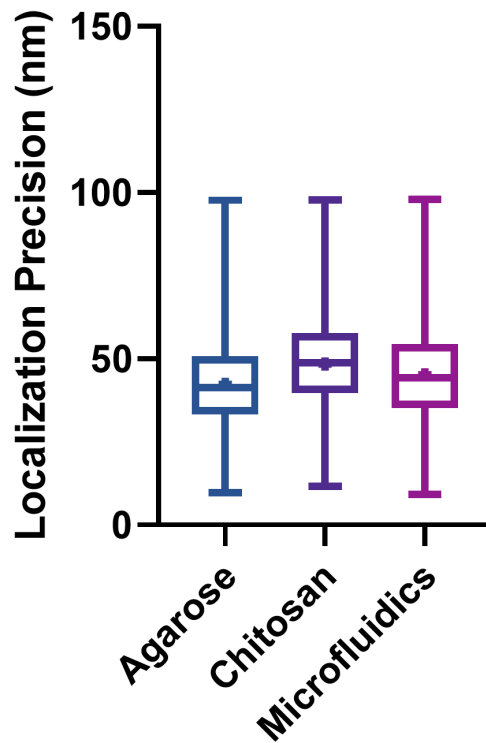
Figure 4.3: Comparing localization precision. Localization precision (95% confidence interval on localization position) for $N = 100{,}000$ single molecules each detected in cells immobilized on agarose pads (blue), on chitosan-coated coverslips (purple), or in a microfluidic device (pink). The box indicates the middle 50% of the data set and the middle line indicates the median. The single point represents the mean. The horizontal lines indicate the minimum and maximum of each total data set.
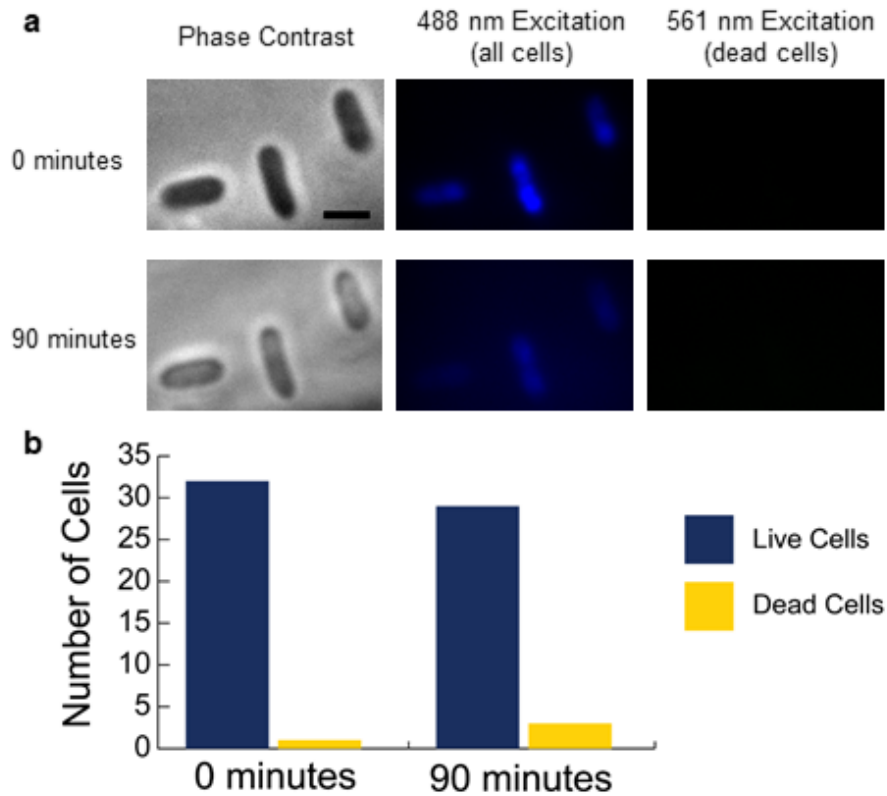
Figure 4.4: Examining cell health adherence chitosan coverslip after hydrogen peroxide addition. Comparing the health of *E. coli* cells immobilized on chitosan-coated coverslip before addition of hydrogen peroxide and 90 minutes after changing cell environment to M9 and hydrogen peroxide at 10 μM. 488-nm illumination: SYTO9 dye, which permeates all cells (false colored blue). 561-nm illumination: propidium iodine dye, which permeates only dead cells (false colored green). a) Examples of cells that are alive before and 90 minutes after exposure to 10 μM hydrogen peroxide (H_2O_2). b) Cell viability before addition of hydrogen peroxide and 90 minutes after changing cell environment to M9 and hydrogen peroxide at 10 μM. Dead cells: all cells detected by in both the 488- and 561-nm channels. Live cells: all cells detected only in the 488-nm channel.
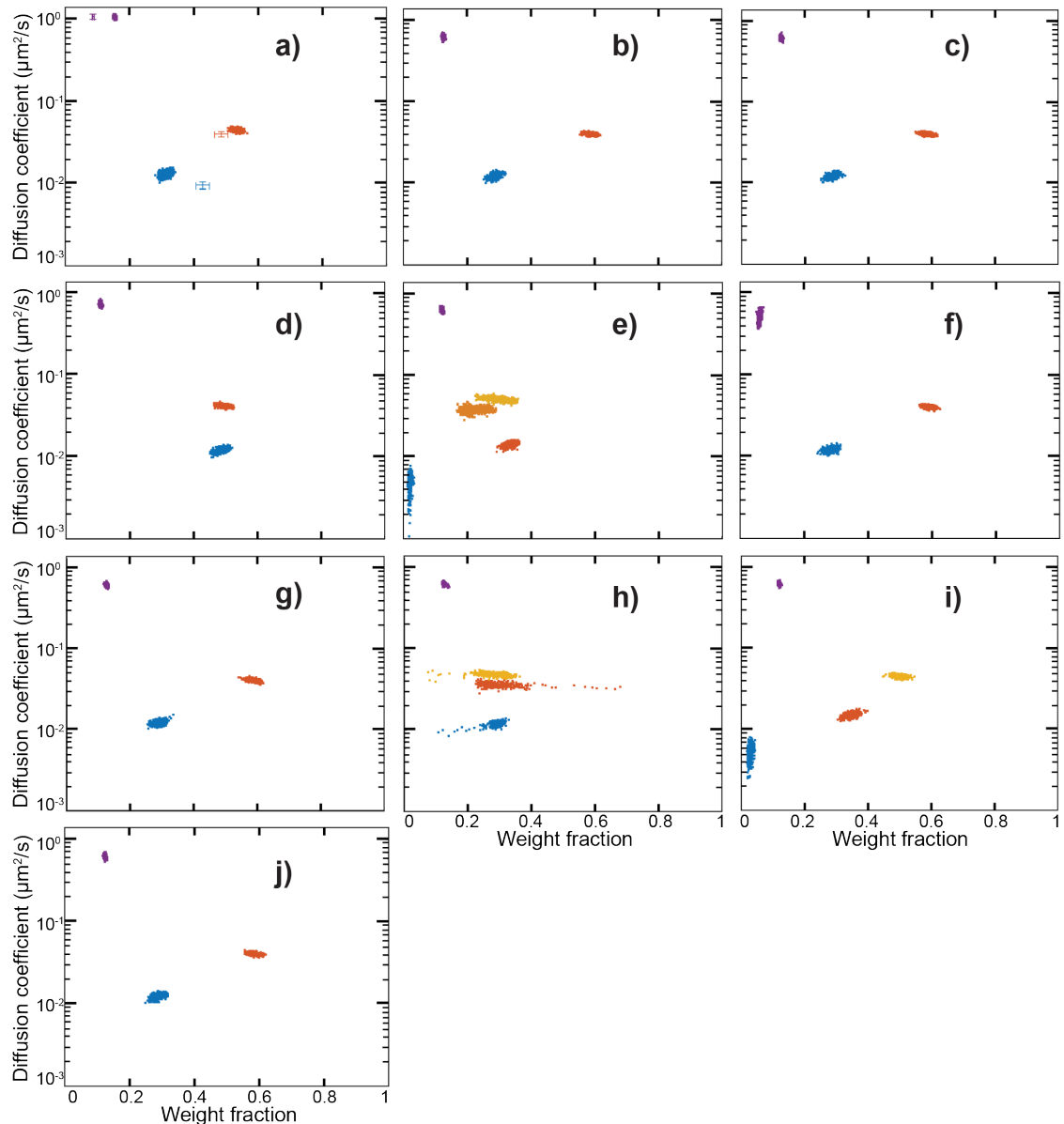
Figure 4.5: Replications of single-molecule tracking analysis. Average single-molecule diffusion coefficients and weight fraction estimates for TcpP-PAmC in live *V. cholerae tcpP-PAmCherry* cells grown under virulence-inducing conditions and immobilized on chitosan-coated coverslips (Fig. 4.1c). Each point represents the average single-molecule diffusion coefficient vs. weight fraction of TcpP-PAmC molecules in each distinct mobility state at each saved iteration of the Bayesian algorithm after convergence. The single-step analysis for the same data set generally identifies three diffusion states (fastest to slowest: purple, orange, and blue) but occasionally finds additional states (light orange and yellow). The outcome in Fig. 4.1c is shown again here in panel 'a' for comparison. 70% of the analysis outcomes have three diffusion states, and panel 'a' has a weight fraction distribution closest to the average; therefore, we chose 'a' as the most likely distribution. A similar process of repeating the analysis was applied to all other data sets analyzed in this study.

4.3.2 Measuring Changes in TcpP-PAmCherry Dynamics on Chitosan-coated Coverslips during Real-time Induction of Genetic Changes

We analyzed TcpP-PAmC motion in *V. cholerae* cells expressing the TcpP-binding partner ToxR under the control of an IPTG-inducible promoter (*tcpP-PAmCherry pMMB66EH-toxR ΔtoxR*; Fig. 4.6) [1]. We found that incubating these cells in 0.1 mM IPTG for 3 h at room temperature followed by traditional sample preparation on agarose pads leads to expression of sufficient ToxR protein that the TcpP-PAmC dynamics (cross-hairs in Fig. 4.6 at 180 min) resemble those of TcpP-PAmC in otherwise wild-type cells (cross-hairs in Fig. 4.1c). Average diffusion coefficients are shown in Table 4.1. With cells mounted on chitosan-coated coverslips, we analyzed how the TcpP-PAmC diffusion changes in real time after exchanging from minimal medium without IPTG to minimal medium with 0.1 mM IPTG. Use of chitosan-coated coverslips gives us the ability to monitor changes in the single-molecule dynamics in real time with 5-min temporal resolution. At early time points, we observed a state (green in Fig. 4.6) that is even slower than the binding state (blue in Fig. 4.6). With chitosan-coated coverslips, we also observed the disappearance of this slowest diffusion state (green) between 20 and 25 min after induction of *toxR* expression. The observed TcpP-PAmC dynamics returns to three states after 25 min, matching the dynamics observed in otherwise wild-type cells (Fig. 4.6 at 25 min and Fig. 4.7 at 30 – 60 min). This 20 – 25 min transition time matches previously reported measurements of the time for transcription activation in bacteria cells [139, 140]. At 20 min, we observed two states with very similar diffusion coefficients and therefore we labeled them both as blue states. We attribute this non-converged result to measurement noise: the rapidly changing dynamics at this time point lead to an analysis of mixed populations during our finite (5-minute) imaging window.
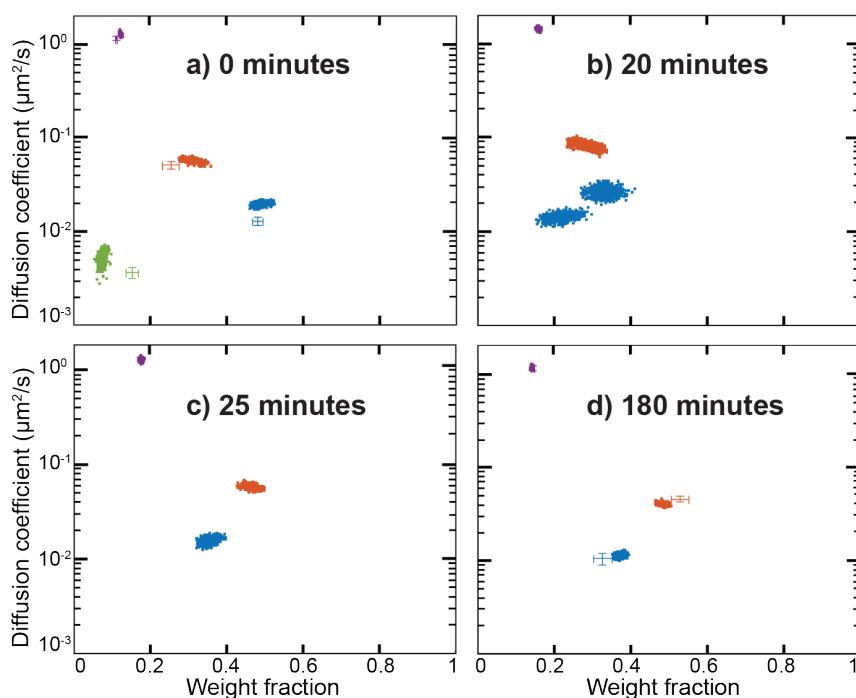
Figure 4.6: Changes in TcpP-PAmCherry dynamics on chitosan-coated coverslips during real-time environment changes. Average single-molecule diffusion coefficients and weight fraction estimates for TcpP-PAmC in live *V. cholerae tcpP-PAmCherry pMMB66eh-toxR ΔtoxR* cells grown under virulence-inducing conditions and immobilized on chitosan-coated coverslips at a) 0 min, b) 20 min, c) 25 min, and d) 180 min after exchanging in situ to cell media containing 0.1 mM IPTG, which induces *toxR* transcription, at 0 min. Each time on the graph indicates the beginning time of data collection. Each data collection window is approximately 4 minutes after that indicated time. Single-step analysis identifies three or four distinct diffusion states (fastest to slowest: purple, orange, blue and green). Each point represents the average single-molecule diffusion coefficient vs. weight fraction of TcpP-PAmC molecules in each distinct mobility state at each saved iteration of the Bayesian algorithm after convergence. The data sets each contain 33,452 – 82,146 steps from 9,116 – 20,727 trajectories. The data for TcpP-PAmC diffusion in living *V. cholerae tcpP-PAmCherry pMMB66eh-toxR ΔtoxR* cells grown under virulence-inducing conditions and immobilized with traditional sample preparation is provided for reference (cross-hairs on the 0 min plot). Data for TcpP-PAmC diffusion in living *V. cholerae* cells grown under virulence-inducing conditions, exposed to 0.1 mM IPTG for 3 hours, and immobilized with traditional sample preparation is provided for reference (cross-hairs on the 180 min plot).
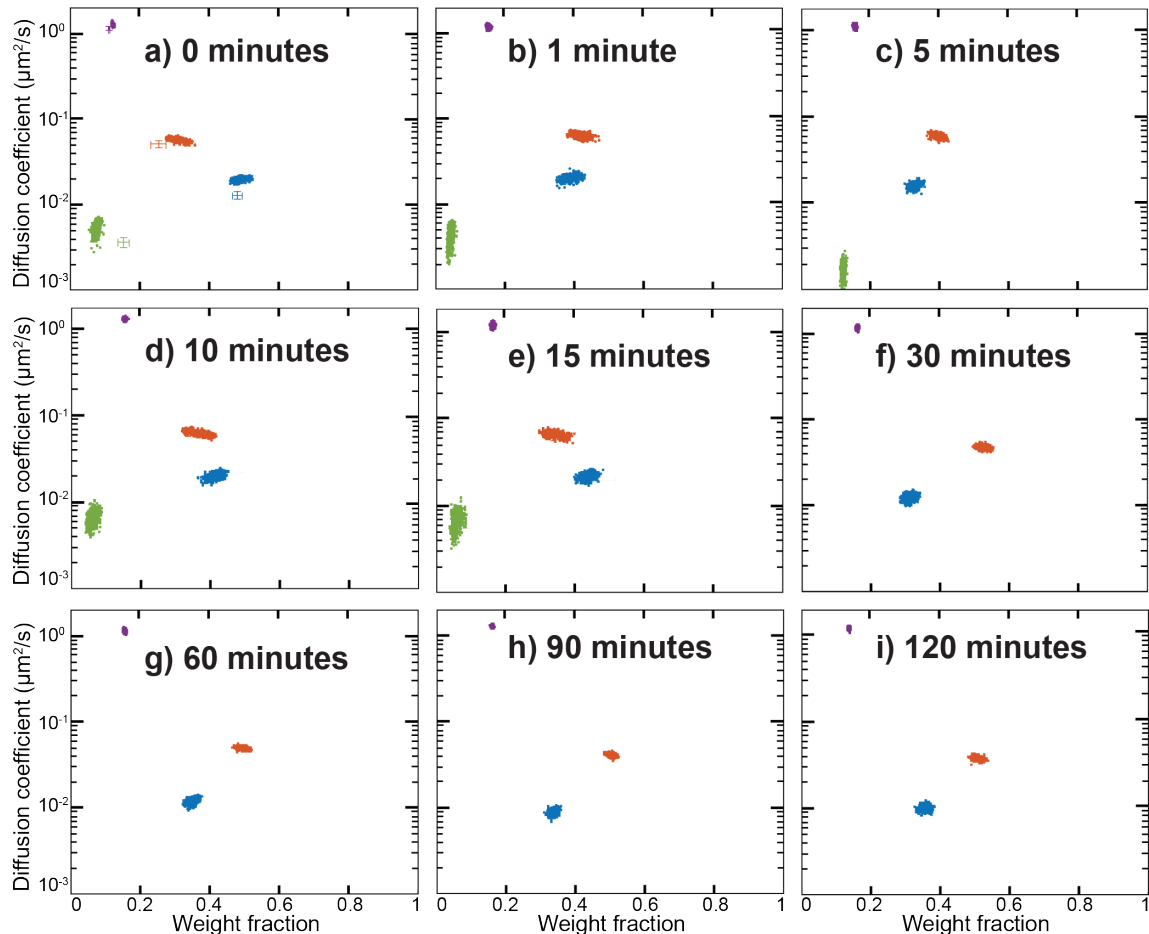
Figure 4.7: Changes in TcpP-PAmCherry dynamics on chitosan-coated coverslips during real-time environment changes continued. Average single-molecule diffusion coefficients and weight fraction estimates for TcpP-PAmC in live *V. cholerae tcpP-PAmCherry pMMB66eh-toxR ΔtoxR* cells grown under virulence-inducing conditions and immobilized on chitosan-coated coverslips at various time points as indicated after changing cell environment to M9 with IPTG at 0.1mM, inducing *toxR* transcription. Each time on the graph indicates the beginning time of data collection. Each data collection window is approximately 4 minutes after that indicated time. Single-step analysis identifies three or four distinct diffusion states (fastest to slowest: purple, orange, blue, and green). Each point represents the average single-molecule diffusion coefficient vs. weight fraction of TcpP-PAmC molecules in each distinct mobility state at each saved iteration of the Bayesian algorithm after convergence. The data sets each contain 33,452 − 82,146 steps from 9,116 − 20,727 trajectories. The data for TcpP-PAmC diffusion in living *V. cholerae tcpP-PAmCherry pMMB66eh-toxR ΔtoxR* cells grown under virulence-inducing conditions and immobilized with traditional sample preparation (Fig. 4.6a) is provided for reference (cross-hairs) in 'a'.

Table 4.1: Average diffusion coefficient and weight fraction for each diffusion state in this section's figures as indicated.

Figure	Condition	State Color	Diffusion Coefficient (μm^2)	Weight Fraction
4.1c	Chitosan	purple	1.057 ± 0.038	0.15
4.1c	Chitosan	orange	0.045 ± 0.002	0.53
4.1c	Chitosan	blue	0.013 ± 0.001	0.32
4.1c	Agarose	purple	1.071 ± 0.041	0.09
4.1c	Agarose	orange	0.040 ± 0.001	0.48
4.1c	Agarose	blue	0.010 ± 0.004	0.43
4.6c (0 min)	Chitosan	purple	1.270 ± 0.037	0.12
4.6c (0 min)	Chitosan	orange	0.057 ± 0.003	0.32
4.6c (0 min)	Chitosan	blue	0.020 ± 0.001	0.48
4.6c (0 min)	Chitosan	green	0.005 ± 0.001	0.08
4.6c (0 min)	Agarose	purple	1.164 ± 0.026	0.11
4.6c (0 min)	Agarose	orange	0.049 ± 0.003	0.25
4.6c (0 min)	Agarose	blue	0.013 ± 0.001	0.48
4.6c (0 min)	Agarose	green	0.004 ± 0.0002	0.16
4.6c (180 min)	Chitosan	purple	1.213 ± 0.030	0.14
4.6c (180 min)	Chitosan	orange	0.041 ± 0.002	0.48
4.6c (180 min)	Chitosan	blue	0.011 ± 0.001	0.38
4.6c (180 min)	Agarose	purple	1.188 ± 0.035	0.14
4.6c (180 min)	Agarose	orange	0.047 ± 0.002	0.53
4.6c (180 min)	Agarose	blue	0.011 ± 0.001	0.33

4.4   Conclusions

Environmental factors have been shown to dramatically change the interactions and motions of molecules inside cells [5, 6, 8, 9, 24], but the real-time effects of these changes have not previously been examined with live-cell single-molecule imaging. Here, we address this gap in experimental ability by developing sample preparation platforms to immobilize live bacteria cells while keeping their environment accessible to changes and without disrupting their natural cell function. We show that chitosan-coated coverslips can be used as substrates for experiments tracking single molecules in live *V. cholerae* cells and we observed that the TcpP-PAmC dynamics are not changed on chitosan-coated coverslips, relative to their dynamics in cells mounted on agarose pads. Additionally, these coverslips enable us to monitor real-time changes in single-molecule dynamics upon changes to the cell environment. We demonstrated this ability by observing the transition

in dynamics of TcpP-PAmC in cells expressing an IPTG-inducible copy of *toxR*, which encodes the TcpP binding partner and co-activator of *toxT*. This transition occurs at 20 min after addition of IPTG, matching the time frame of transcription induction in previous studies [139, 140]. We observed these dynamics changes with a 5-min temporal resolution not possible with traditional sample preparation technologies.

CHAPTER V

Regulation of Toxin Production in *Vibrio cholerae* in Response to Real-time Changes in Environment pH

The work presented in this chapter was previously published in Analytical Chemistry

5.1   Introduction

In the previous chapter, I present a sample preparation method capable of immobilizing *Vibrio cholerae* (*V. cholerae*) cells without altering the cell's natural functions and which allow for real-time environmental perturbations during single-molecule imaging. I localize and track single TcpP-PAmCherry (TcpP-PAmC) molecules in live *V. cholerae* cells immobilized on chitosan-coated coverslips and show that these dynamics match previously published results with traditional sample preparation. To display the capabilities of our sample preparation method in this chapter, we analyze how TcpP-PAmC dynam-

ics evolve in real time after a change in the surrounding pH with a five-minute temporal resolution.

5.2 Materials and Methods

5.2.1 Bacterial Strains and Growth Conditions

The two *V. cholerae* strains used here were all in the O395 classical biotype background. Strains used in this study were wild-type (WT) and *tcpP-PAmCherry*. All construct development was previously published [1]. *V. cholerae* strains were grown overnight at 37 °C on lysogeny broth (LB) plates containing streptomycin ($100\mu g$ mL^{-1}, streptomycin (strp)). Then, an individual colony was picked and grown overnight in LB + strp medium under indicated conditions (virulence-inducing or non-virulence inducing conditions). Overnight *V. cholerae* cell cultures were diluted into LB + strp medium and grown until they reached mid-log phase. Cultures were then centrifuged at 5000 rpm for 1.5 min and resuspended in half the volume of M9 minimal medium + strp with 0.4% glycerol. This concentrated cell culture method was used for all traditional and chitosan slide coating sample preparation described for all growth conditions.

Two growth conditions were used for this study: virulence-inducing conditions (medium pH adjusted to 6.0 (± 0.05) with 1 M hydrochloric acid; temperature set to 30 °C) and non-virulence inducing conditions (medium pH adjusted to 8.0 (±0.05) with 1 M sodium hydroxide; temperature set to 37 °C).

5.2.2 Single-molecule Microscopy

A minimum of 50 cells per condition were imaged at room temperature using an Olympus IX71 inverted epifluorescence microscope with a 100X 1.40-NA oil-immersion objective, a 405-nm laser (Coherent Cube 405-100; 50 W/cm^2) for photoactivation, and a coaligned 561-nm laser (Coherent-Sapphire 561-50; 210 W/cm^2) for fluorescence excita-

tion. Fluorescence emission was filtered with appropriate filters and captured on a 512-by 512-pixel Photometrics Evolve electron multiplying charged-couple detector (EMCCD) camera. To prevent higher-order excitation during photoactivation, a pair of Uniblitz shutters controlled the laser beams such that samples were exposed to only one laser at a time. During imaging, the cells were given a 40-ms dose of 405-nm light every 90 s. Images were collected continuously every 40 ms, and acquisitions lasted 5 - 7 min each.

5.2.3 Data Analysis

Recorded single-molecule positions were detected and localized based on point spread function fitting using our home-built code, Single-Molecule Accurate LocaLization by LocAl Background Subtraction (SMALL-LABS) [37]. This program reduces biases due to background subtraction, increasing the accuracy of each single-molecule localization. Subsequent localizations of the same molecule were then connected into trajectories using the Hungarian algorithm [118]. All trajectories from each movie for a given condition were combined and analyzed together using the Single-Molecule Analysis by Unsupervised Gibbs sampling (SMAUG) algorithm [38]. This algorithm considers the collection of all the steps within all the trajectories and uses a Bayesian statistical framework to infer the parameters of interest including the number of mobility states and the diffusion coefficient and weight fraction of each state. A minimum of 25,000 steps were analyzed at each condition.

5.2.4 Traditional (Agarose Pad) Cell Sample Preparation

A 1.5-μL droplet of concentrated cells was placed onto an agarose pad (2% agarose (Fisher Bioreagents) in M9 + strp at appropriate pH, spread and flattened on a microscope slide) and covered with an argon plasma-etched coverslip. Imaging was performed within 1 hour of making the agarose pad and assembling the sample. For the LB experiments, the agarose pad was made with 2% agarose in LB + strp at pH 6 and cells were concentrated

in LB + strp at pH 6.

5.2.5   Chitosan Coverslip Coating

Chitosan powder (low molecular weight, deacetylated chitin, Sigma Aldrich) was added to a concentration of 2.5% in 25% v/v acetic acid in water and gently shaken overnight to fully dissolve. 500 μL of the solution was pipetted onto the center of an argon plasma-etched glass coverslip followed by spinning at 2000 rpm for 5 min to form a thin film of the chitosan solution on top. Coverslips dried overnight in an enclosed container then were washed with 1% acetic acid in water then water and dried with air. Chitosan-coated coverslips were stored in an enclosed container until use for up to one month.

5.2.6   Chitosan-coated Coverslip Cell Sample Preparation

V. cholerae cells in M9 minimal media were pipetted into a hard plastic O-ring on a chitosan-coated coverslip and allowed to bind for 10 min. Media and unbound cells were removed without scratching slide surface using a pipette. Fresh M9 media was immediately added to the O-ring. The sample was placed on the microscope stage for single-molecule microscopy. To change the cell environment, media was pipetted out and a new media environment was immediately added to the O-ring. To induce virulence conditions, M9 media + strp at pH 6 was added.

5.3   Results and Discussion

5.3.1   Effect of pH on TcpP-PAmCherry Dynamics in Living *Vibrio cholerae* Cells in Real Time

The surrounding pH has been shown to be a key factor in inducing *V. cholerae* virulence; specifically, decreasing to pH 6 increases toxin and pilus production, and pH 6 media is therefore used as the virulence-inducing condition [29,31]. We applied our new method

for real-time single-molecule imaging in living bacteria to understand the timing of the response of TcpP to extracellular changes in pH to provide more mechanistic information. Our previous studies were carried out at pH 6 to study TcpP-PAmC dynamics under virulence-inducing conditions; we found that the TcpP-PAmC molecules move in three distinct diffusion states: most molecules diffuse slowly or moderately, and a small number diffuse rapidly (blue, orange, and purple cross-hairs, respectively, in Fig. 4.1). We found different TcpP-PAmC diffusion states in cells grown at pH 8 (non-virulence inducing conditions): a slower state (green) emerges, reducing the population of the intermediate state (orange) (Fig. 5.1a). As alkaline pH has been well documented not to support *toxT* expression, we attribute this slowest group to a role reassignment of the TcpP molecules, which reduces the number of molecules capable of searching for, and ultimately binding to, the promoter, and even perhaps being sequestered away from the *toxT* promoter (*toxTpro*). We generated the normalized localization density maps of TcpP-PAmC in cells grown at non-virulence inducing conditions from the data in 57 WT cells (Fig. 5.2a) to determine the spatial distribution of each diffusion state (Fig. 5.3) [117]. We found that molecules in the slowest state (green) were more likely to be localized at the poles in comparison to molecules in the other states. This finding is consistent with molecules being sequestered away from the nucleoid.

We also found that, for *V. cholerae* grown in non-virulence inducing conditions (pH 8), the TcpP-PAmC dynamics change in response to decreasing the extracellular pH to virulence-inducing conditions (pH 6). We grew cells at pH 8, spun them down, and resuspended in minimal medium at pH 6. These cells were left at room temperature for 3 hours with no shaking then imaged. Analysis of the dynamics of TcpP-PAmC at this 3-hour timepoint shows that the motions match those of cells grown exclusively at virulence-inducing conditions (Fig. 5.1b).

Figure 5.1: TcpP-PAmCherry dynamics before and after changes from pH 8 to 6. Average single-molecule diffusion coefficients and weight fraction estimates for TcpP-PAmC in live *V. cholerae* cells. Single-step analysis identifies three or four distinct diffusion states (fastest to slowest: purple, orange, blue, and green). Each point represents the average single-molecule diffusion coefficient vs. weight fraction of TcpP-PAmC molecules in each distinct mobility state at each saved iteration of the Bayesian algorithm after convergence. a) Cells were grown under non-virulence inducing conditions and immobilized on an agarose pad (traditional sample preparation). b) Cells were grown under non-virulence inducing conditions and switched to virulence-inducing conditions. Three hours later, cells were immobilized on an agarose pad (traditional sample preparation) and imaged. The data set contains 50,574 steps from 5,965 trajectories for 'a' and 43,169 steps from 5,884 trajectories for 'b'. The previously published data for TcpP-PAmC diffusion in living *V. cholerae* cells grown under virulence-inducing conditions immobilized under an agarose pad (traditional sample preparation) are provided for reference (cross-hairs) in both panels.

Figure 5.2: TcpP-PAmCherry dynamics during real-time changes from pH 8 to 6.
Caption on next page.

Figure 5.2: Average single-molecule diffusion coefficients and weight fraction estimates for TcpP-PAmC in live *V. cholerae* cells grown under non-virulence inducing conditions and immobilized on chitosan-coated coverslips. The cell media is exchanged to virulence-inducing conditions (pH = 6) in situ at 0 min. Each time on the graph indicates the beginning time of data collection. Each data collection window is approximately 4 minutes after that indicated time. Single-step analysis identifies three or four distinct diffusion states (fastest to slowest: purple, orange, blue, and green). Each point represents the average single-molecule diffusion coefficient vs. weight fraction of TcpP-PAmC molecules in each distinct mobility state at each saved iteration of the Bayesian algorithm after convergence. The data sets each contain 20,785 – 51,235 steps from 3,803 – 10,219 trajectories. The data for TcpP-PAmC diffusion in living *V. cholerae* cells grown under non-virulence inducing conditions and immobilized with traditional sample preparation are provided for reference (cross-hairs on the 0 min plot). The data for TcpP-PAmC diffusion in living *V. cholerae* cells grown under virulence-inducing conditions and immobilized with traditional sample preparation are provided for reference (cross-hairs on the 180 min plot). r) Weight fraction of the slowest state (green) at each time point in Fig. 4.6b-j (navy blue) and Fig. 5.2a-d (yellow).
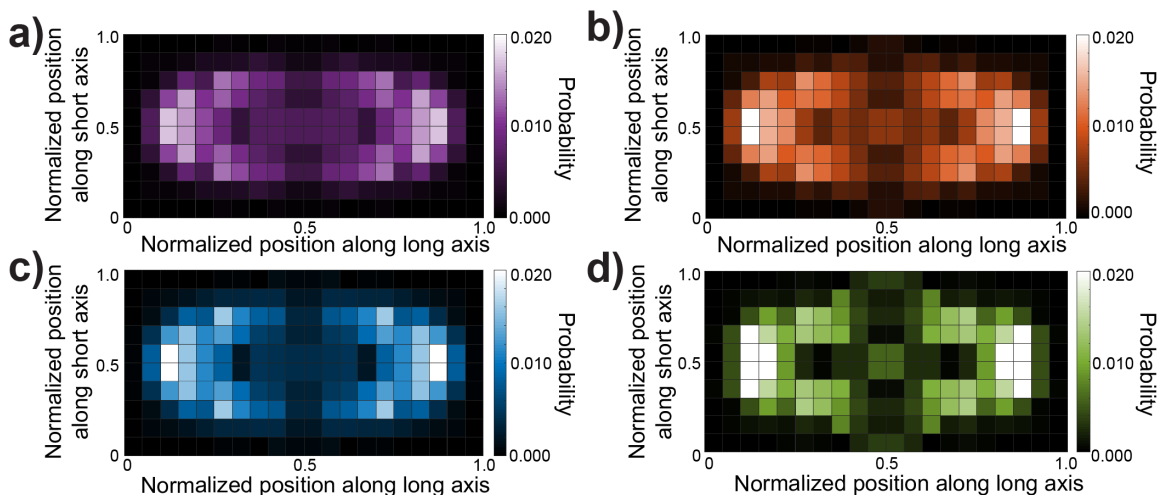
Figure 5.3: Localization probability density maps of TcpP-PAmCherry. Localization probability density maps within a normalized cell for each of the four diffusion states of TcpP-PAmC in live *V. cholerae* cells grown under non-virulence inducing conditions (data from Fig. 5.2a): a) fast state (purple); b) intermediate state (orange); c) slow state (blue); d) slowest state (green). Single-molecule localizations from 57 cells are projected along the long and short axes of the cell, normalized to their relative position, and re-symmetrized along the axes; each pixel color indicates the percentage of localizations (probability of localization) in that region [117].

To measure the timescale of the change that occurs during this three-hour period, we grew cells at pH 8, mounted cells on chitosan-coated coverslips, decreased the *V. cholerae* cell medium pH to 6 at 0 min, and then characterized the TcpP-PAmC dynamics in real time in five-min increments (Fig. 5.2). Average diffusion coefficients are shown in Table 5.1. In particular, we monitored the reduction and subsequent disappearance of the stationary state (green) that is observed under non-virulence inducing conditions over time after exposure to media at pH 6 (virulence-inducing conditions). We observed that the weight fraction of this slowest group (green) begins to decrease starting at 30 min and disappears at 45 min. Additionally, we observed a corresponding increase in the weight fraction of the searching state (orange). At 50 min, we observed a decrease in the weight fraction of the bound state (blue) before the dynamics fully stabilize to three groups at 55 min, matching the pH 6 results (Fig. 5.2). We attribute the rapid changes in the weight fraction of the blue and orange states between 45 and 50 min to measurement noise: the rapidly changing dynamics as the system reaches equilibrium lead to an analysis of mixed populations during our finite (5-minute) imaging window. Consistent with our previous studies of TcpP-PAmC dynamics as a function of *V. cholerae* mutations, we detect either three or four groups at all time points; no additional intermediate groups appear [1].

As a control, we tracked the dynamics of TcpP-PAmC in *V. cholerae* cells on chitosan-coated coverslips over a 3-hour period after exchanging the medium with fresh buffer without changing the pH and found no changes in dynamics (Fig. 5.4). Interestingly, we found that, for *V. cholerae* grown in virulence inducing conditions (pH 6); the TcpP-PAmC dynamics do not change in response to increasing the extracellular pH to non-virulence inducing conditions, which indicates that this induction of virulence is irreversible within 4 hours (Fig. 5.5).
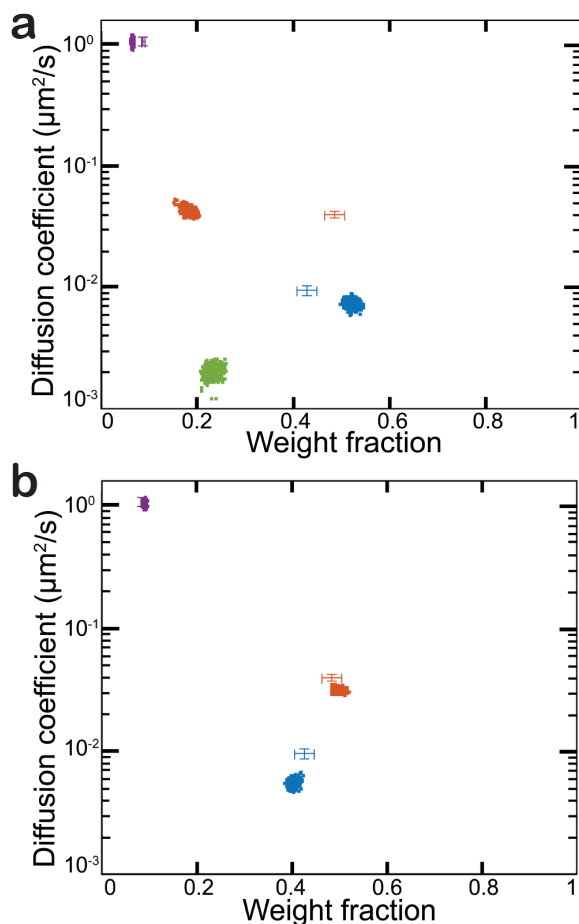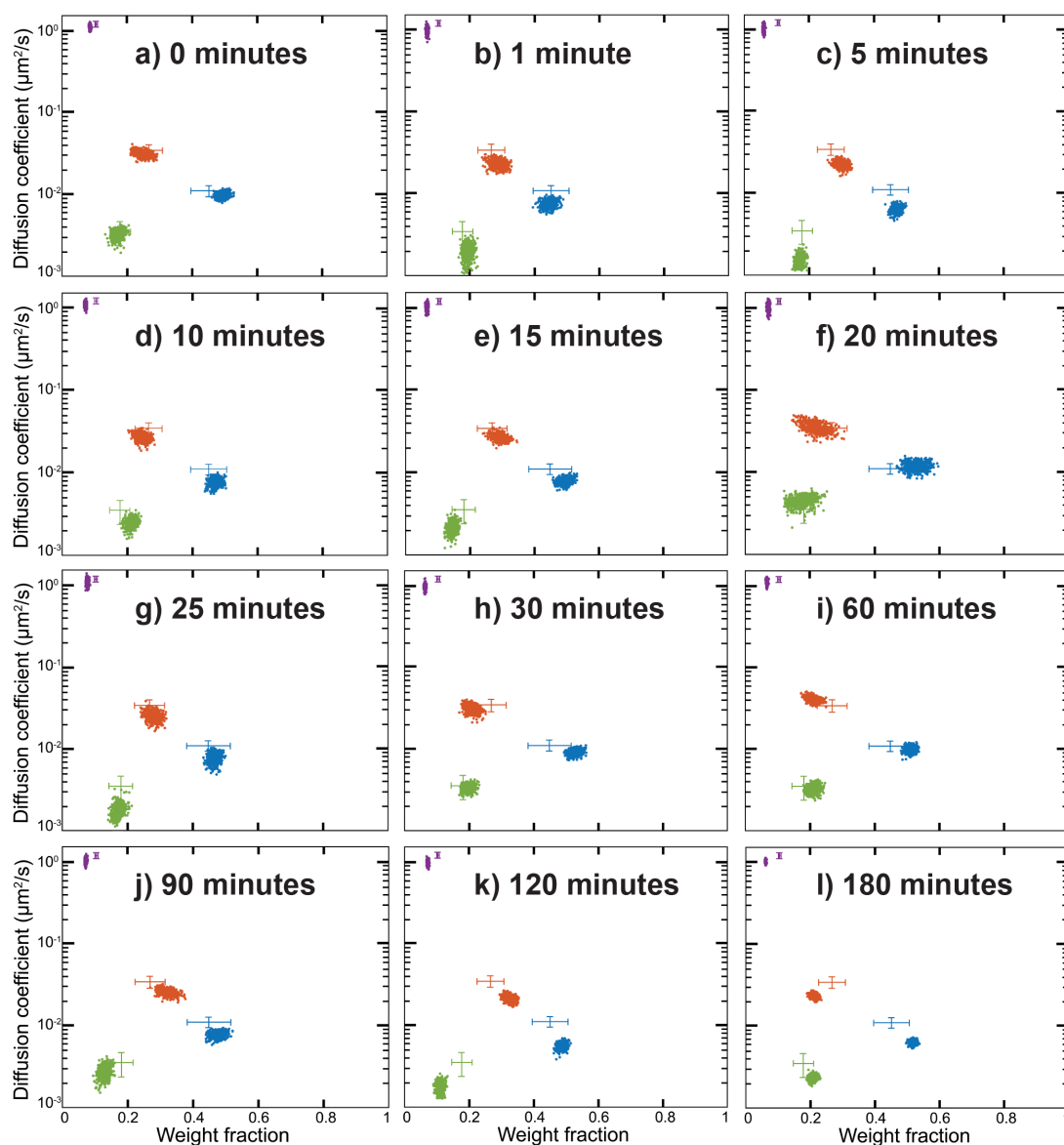
Figure 5.4: TcpP-PAmCherry dynamics during no changes in pH. Average single-molecule diffusion coefficients and weight fraction estimates for TcpP-PAmC in live *V. cholerae* cells grown under non-virulence inducing conditions and immobilized on chitosan-coated coverslips at various time points as indicated after changing media for fresh media with the same non-virulence inducing environment conditions. Each time on the graph indicates the beginning time of data collection. Each data collection window is approximately 4 minutes after that indicated time. Single-step analysis identifies four distinct diffusion states (fastest to slowest: purple, orange, blue, and green). Each point represents the average single-molecule diffusion coefficient vs. weight fraction of TcpP-PAmC molecules in each distinct mobility state at each saved iteration of the Bayesian algorithm after convergence. The data sets each contain 15,098 – 96,748 steps from 2,142 –12,768 trajectories. The data for TcpP-PAmC diffusion in living *V. cholerae* cells grown under non-virulence inducing conditions and immobilized with chitosan coverslip coatings are provided for reference (cross-hairs). No change in dynamics occurs upon this media replacement.
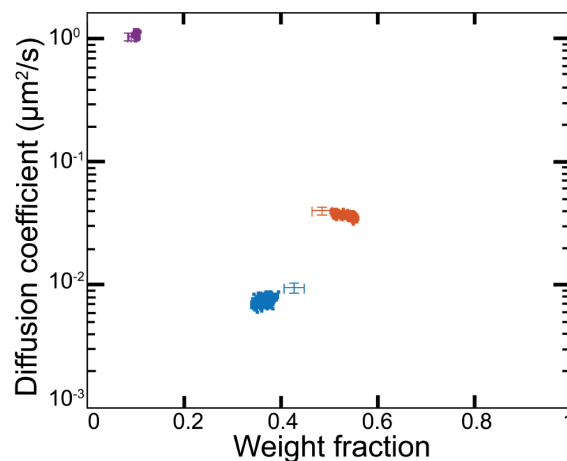
Figure 5.5: TcpP-PAmCherry dynamics during changes from pH 6 to 8. Average single-molecule diffusion coefficients and weight fraction estimates for TcpP-PAmC in live *V. cholerae* cells grown under virulence-inducing conditions and switched to non-virulence inducing conditions. Cells were immobilized on an agarose pad after 3 hours. Single-step analysis identifies three distinct diffusion states (fastest to slowest: purple, orange, and blue). Each point represents the average single-molecule diffusion coefficient vs. weight fraction of TcpP-PAmC molecules in each distinct mobility state at each saved iteration of the Bayesian algorithm after convergence. The data set contains 32,686 steps from 4,536 trajectories. The previously published data for TcpP-PAmC diffusion in living *V. cholerae* cells grown under virulence-inducing conditions immobilized under an agarose pad (traditional sample preparation) are provided for reference (cross-hairs). No change in dynamics occurs upon alteration of environment.
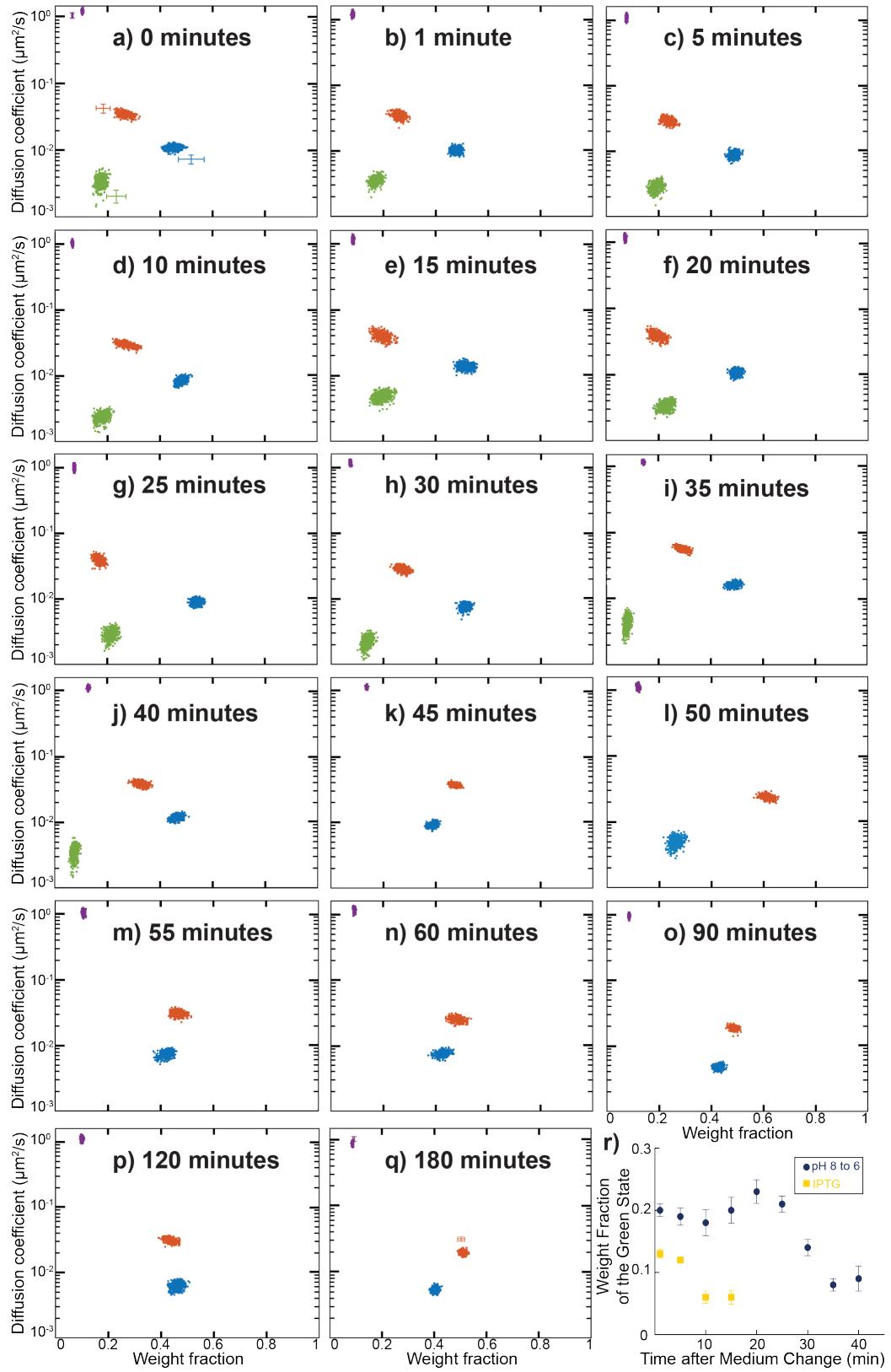
Table 5.1: Average diffusion coefficient and weight fraction for each diffusion state in this section's figures as indicated.

Figure	Condition	State Color	Diffusion Coefficient (μm^2)	Weight Fraction
5.2a (0 min)	Chitosan	purple	1.226 ± 0.051	0.10
5.2a (0 min)	Chitosan	orange	0.035 ± 0.003	0.27
5.2a (0 min)	Chitosan	blue	0.011 ± 0.001	0.45
5.2a (0 min)	Chitosan	green	0.004 ± 0.001	0.18
5.2a (0 min)	Agarose	purple	1.065 ± 0.052	0.07
5.2a (0 min)	Agarose	orange	0.043 ± 0.003	0.18
5.2a (0 min)	Agarose	blue	0.008 ± 0.001	0.52
5.2a (0 min)	Agarose	green	0.002 ± 0.0002	0.23
5.2h (30 min)	Chitosan	purple	1.187 ± 0.061	0.08
5.2h (30 min)	Chitosan	orange	0.028 ± 0.002	0.27
5.2h (30 min)	Chitosan	blue	0.008 ± 0.001	0.51
5.2h (30 min)	Chitosan	green	0.002 ± 0.0004	0.14
5.2i (35 min)	Chitosan	purple	1.065 ± 0.052	0.07
5.2i (35 min)	Chitosan	orange	0.044 ± 0.003	0.18
5.2i (35 min)	Chitosan	blue	0.008 ± 0.001	0.52
5.2i (35 min)	Chitosan	green	0.002 ± 0.0002	0.23
5.2j (40 min)	Chitosan	purple	1.107 ± 0.045	0.13
5.2j (40 min)	Chitosan	orange	0.041 ± 0.011	0.32
5.2j (40 min)	Chitosan	blue	0.013 ± 0.002	0.47
5.2j (40 min)	Chitosan	green	0.004 ± 0.001	0.09
5.2k (45 min)	Chitosan	purple	1.121 ± 0.038	0.14
5.2k (45 min)	Chitosan	orange	0.038 ± 0.002	0.47
5.2k (45 min)	Chitosan	blue	0.009 ± 0.001	0.39
5.2l (50 min)	Chitosan	purple	1.131 ± 0.067	0.12
5.2l (50 min)	Chitosan	orange	0.024 ± 0.002	0.61
5.2l (50 min)	Chitosan	blue	0.005 ± 0.001	0.27
5.2m (55 min)	Chitosan	purple	1.051 ± 0.068	0.11
5.2m (55 min)	Chitosan	orange	0.031 ± 0.002	0.47
5.2m (55 min)	Chitosan	blue	0.008 ± 0.001	0.42
5.2n (60 min)	Chitosan	purple	1.171 ± 0.078	0.09
5.2n (60 min)	Chitosan	orange	0.025 ± 0.003	0.48
5.2n (60 min)	Chitosan	blue	0.008 ± 0.003	0.43
5.2q (180 min)	Chitosan	purple	0.868 ± 0.042	0.09
5.2q (180 min)	Chitosan	orange	0.020 ± 0.001	0.51
5.2q (180 min)	Chitosan	blue	0.006 ± 0.0003	0.40
5.2q (180 min)	Agarose	purple	1.103 ± 0.043	0.09
5.2q (180 min)	Agarose	orange	0.032 ± 0.001	0.50
5.2q (180 min)	Agarose	blue	0.006 ± 0.0004	0.41

5.4 Conclusions

We implemented this new experimental protocol to study the effects of changes in pH on TcpP-PAmC dynamics and found that virulence induction occurs during the period $30-55$ min after exchanging the cell media with pH 6 media, which establishes virulence-inducing conditions. We hypothesized that the slowest diffusion state (green in Fig. 5.2), which is only found at non-virulence inducing conditions, corresponds to sequestering of TcpP away from its binding site. The timescale of the disappearance of this slowest state (green) Fig. 5.2r, combined with the higher likelihood of molecules in this state localizing at the poles, confirms our hypothesis regarding the biophysical role: TcpP is sequestered from the *toxTpro* at pH 8 and gradually allowed to bind upon environmental signaling (pH 6). If new TcpP was being introduced into the cells through transcription and translation, we would see a reduction at $20-25$ min as was the timing in the activation of *toxR* transcription. Rather, the weight fraction of the stationary state (green) gradually decreases with a corresponding increase in the weight fraction of the searching state (orange) on a timescale longer than 25 min. This finding indicates that TcpP is slowly released from sequestration and allowed to search for its binding site on the *toxTpro* with time at pH 6. Prior to this work, there was no evidence that TcpP molecules are sequestered from the *toxTpro*. The work presented here has revealed a novel mechanism of post-translational regulation of TcpP that motivates further study. This result highlights the value of the chitosan slide coating technology to better understand the mechanism by which TcpP regulates *V. cholerae* toxin production as this conclusion can only be drawn based on the ability to monitor these single-molecule dynamics during changes in real time. The chitosan-coated coverslip is robust to many environment changes including pH and increased oxidative conditions and can immobilize a variety of bacteria. This cell immobilization methodology can be expanded to study other bacteria and impact our understanding of their biological functions in changing environments.

Regulation of a DNA-binding Protein in *Escherichia coli* in Response to Real-time Oxidative Damage

Bacteria strains constructed by Elio Abbondanzieri, Lauren M. McCarthy, and Vyom Grover.

6.1   Introduction

Bacteria survive many environmental stresses by protecting their most vital components in the nucleoid including DNA. *Escherichia coli* (*E. coli*) employs a DNA-binding protein, DNA-binding Protein from Starved cells (Dps), to compact the nucleoid and selectively exclude molecules from entering the nucleoid [141]. Dps typically self-associates to form dodecamers [142] and this complex binds to DNA in vitro with no apparent sequence specificity [143, 144]. This protein has been studied during starvation conditions under which *E. coli* can survive a days-long starvation period. Dps is highly upregulated during this period, becoming one of the highest copy number proteins in the cell [145]. The nucleoid of cells lacking the Dps protein does not compact as much during starvation as cells with the protein [146]. Additionally, cells with Dps can selectively exclude restriction enzymes, but not RNA polymerase (RNAP), from the compact nucleoid, while cells without Dps cannot [146]. Dps also plays an important role in *E. coli* survival during

other stress conditions including oxidative damage, heat shock, exposure to antibiotics, osmotic stress, and overexposure to iron [8, 147, 148].

Microorganisms such as *E. coli* encounter oxidative stress as a by-product of their aerobic metabolism [149]. The resultant formation of reactive oxygen species can lead to damage to cellular components including DNA [150]. These organisms have developed a variety of mechanisms to survive in this challenging environment, including enzymes that reduce reactive oxygen species, excretion pathways, and protective proteins such as Dps in *E. coli* [151, 152]. It is hypothesized that Dps provides dual protection through mechanical shielding by binding to DNA [141, 143, 153] and a chemical reaction using stored iron to reduce hydrogen peroxide (hydrogen peroxide (H_2O_2)) [154]. However, little has been done to explore the exact role of Dps during this stress condition in vivo.

Single-molecule fluorescence (SMF) imaging and tracking can provide insight into the mechanism for Dps response to a variety of stress conditions. Since starvation and oxidative damage trigger different sigma factors, proteins that initiate transcription, (σ^s and σ^{70}, respectively [155–157]) in vivo, it can be hypothesized that Dps could have different mechanisms for cellular protection during the different conditions. These differences can be examined using SMF. Currently work is being done to explore Dps during starvation conditions. Notably, H_2O_2 acts rapidly on Dps expression, approximately 1 hour [8, 158]. Therefore, examining Dps diffusion changes during real-time oxidative damage from H_2O_2 additions is a great application of the new chitosan slide method.

In this chapter, I examine the changes in Dps-PAmCherry (Dps-PAmC) diffusion after addition of H_2O_2 at both the single-cell and single-molecule levels. Using the newly developed chitosan slide method, I explore the rapid stress response by *E. coli* cells in real time and determine Dps-PAmC response to oxidative damage must involve a major chemical response rather than binding to DNA.

6.2   Materials and Methods

6.2.1   Bacterial Strains and Growth Conditions

E. coli strains used here can be found in Table 6.1. Unless otherwise stated, experiments were performed with *E. coli* cells in mid-log /exponential phase (OD_{600} 0.5 − 0.6). *E. coli* strains were grown overnight at 37 ℃ on lysogeny broth (LB) plates containing appropriate antibiotics. Then, an individual colony was picked and grown overnight in Hi-Def Azure (HDA) (Teknova) medium at 250 rpm, at 37 ℃. Overnight *E. coli* cell cultures were diluted into HDA medium in a 125-mL flask and grown until they reached mid-log phase, OD_{600} 0.5 − 0.6 (3 hours). 10 mL of culture was centrifuged at 5000 rpm for 5 minutes. The supernatant was removed and syringe-filtered. This filtered spent medium was used for all sample preparation. The remaining culture was directly used for analysis without any concentration or centrifugation.

For Dps-PAmC experiments, overnight cultures of *E. coli* Dps-PAmC cells were diluted into HDA medium in a 125-mL flask and grown until they reached early-log phase, OD_{600} 0.2 − 0.3 (2 hours). Then, 400 mM isopropyl-β-D-thiogalactopyranoside (IPTG) was added to the culture to a final concentration of 0.5 mM and the culture was returned to the incubator until cells reached mid-log phase, OD_{600} 0.5 − 0.6 (1 hour).

For the late-stationary phase study, overnight *E. coli* cell cultures were diluted into HDA medium in a 125-mL flask and grown for 96 hours at 250 rpm at 37 ℃. 10 mL of culture was centrifuged at 5000 rpm for 5 minutes. The supernatant was removed and syringe-filtered. The filtered supernatant was centrifuged at 5000 rpm for 5 minutes. The new supernatant was removed and syringe-filtered using a new syringe and filter. This twice filtered spent medium was used for late-stationary phase sample preparation. The remaining culture was directly used for analysis without any concentration or centrifugation.

Table 6.1: *E. coli* Strain list.

Strain	Description	Reference
E. coli W3110	Wild type	ATCC collection.
E. coli mCherry	W3110 strain with mCherry integrated into the genome at the native *dps* promoter (*dpspro*)	Meyer lab collection.
E. coli dps-mCherry	W3110 strain with *dps-mCherry* fusion integrated into the genome at the native *dps* locus.	DeMartino, M., Meyer, A. S. et al. J. *Bacteriol*, 2016. *198* (11), 1662–1674.
E. coli dps-PAmCherry	W3110 strain expressing *dps-PAmCherry* from an IPTG-inducible promoter in a pMMB67EH plasmid	This study.

6.2.2 Live/Dead Cell Assay

Using the BacLight Bacterial Viability Kit L7007, 0.25 μL of Component A and 0.25 μL of Component B were added to 500 μL of concentrated wild-type *E. coli* cells in HDA medium. Cells were immobilized on chitosan-coated coverslips according to sample preparation protocol (section 6.2.8). Cells were imaged at room temperature using an Olympus IX71 inverted epifluorescence microscope with a 100X 1.40-numerical aperture (NA) oil-immersion objective, a 488-nm laser (Coherent-Sapphire 488-50; 2.5 W/cm^2) for fluorescence excitation of SYTO 9 (all cells), and a coaligned 561-nm laser (Coherent-Sapphire 561-50; 2.5 W/cm^2) for fluorescence excitation of Propidium iodide (dead cells). Fluorescence emission was filtered with appropriate filters and captured on a 512- by 512-pixel Photometrics Evolve electron multiplying charged-couple detector (EMCCD) camera. Manual shutters were used to block the lasers to image at one wavelength at a time. Images were collected continuously every 40 ms, and acquisitions lasted 2 min for each wavelength. Gridded coverslips (ibidi) were used to measure the same cells at each time point. Three biological replicates of at least 10 cells were performed. Image intensities were analyzed using Fiji Image J2. The same intensity thresholds were applied to every image regardless of sample preparation or collection day. Cells detected in the phase-

contrast, 561-nm, and 488-nm channels were counted as dead; cells appearing in only the phase-contrast and 488-nm channels were counted as alive. Cells appearing in the phase-contrast and/or 561-nm channels but not the 488-nm channels were not counted.

6.2.3   Staining and Imaging of Cell Nucleoid

For exponential phase cells (3 hours after back dilution), 10 μL of 50 μM SYTOX orange nucleic acid stain (Invitrogen) in DMSO was added to 1 mL of culture in a 15 mL culture tube. The culture was incubated at 37 ℃ and 250 rpm for 10 minutes. For late stationary phase cells (96 hours after back dilution), 10 μL of 50 μM SYTOX orange nucleic acid stain (Invitrogen) in DMSO was added to 1 mL of culture in a 15 mL culture tube. The culture was incubated at 37 ℃ and 250 rpm for 45 minutes. Then for both exponential and stationary phase cells, cells were centrifuged for 1.5 minutes at 5000 rpm and the supernatant was removed. 1 mL of filtered spent HDA media was added to the cell pellet. This wash step was repeated. Cells were immobilized on chitosan-coated coverslips according to the sample preparation protocol (section 6.2.8). Cells were imaged at room temperature using an Olympus IX71 inverted epifluorescence microscope with a 100X 1.40-NA oil-immersion objective and a 561-nm laser (Coherent-Sapphire 561-50; 10 W/cm2) for fluorescence excitation of SYTOX orange. Fluorescence emission was filtered with appropriate filters and captured on a 512 by 512-pixel Photometrics Evolve EMCCD camera. Images were collected continuously every 40 ms, and acquisitions lasted 10 s. Three biological replicates of at least 35 cells each were investigated. Home-built code was used to determine nucleoid area from images by measuring the area 50% of the max of the emission intensity. Cell area was determined from the phase contrast image using Cellpose [159]. The nucleoid occupancy was calculated by dividing the nucleoid area by the cell area.

6.2.4 Single-cell Microscopy

A minimum of 50 cells with three biological replicated per condition were imaged at room temperature using an Olympus IX71 inverted epifluorescence microscope with a 100X 1.40-NA oil-immersion objective and a 561-nm laser (Coherent-Sapphire 561-50; 10 W/cm2) for fluorescence excitation. Fluorescence emission was filtered with appropriate filters and captured on a 512 by 512-pixel Photometrics Evolve EMCCD camera. Images were collected continuously every 40 ms, and acquisitions lasted 10 s each. This protocol was used for imaging both mCherry and SYTOX orange in live cells.

6.2.5 Single-molecule Microscopy

A minimum of 50 cells per condition were imaged at room temperature using an Olympus IX71 inverted epifluorescence microscope with a 100X 1.40-NA oil-immersion objective, a 405-nm laser (Coherent Cube 405-100; 5 W/cm2) for photoactivation, and a coaligned 561-nm laser (Coherent-Sapphire 561-50; 310 W/cm2) for fluorescence excitation. Fluorescence emission was filtered with appropriate filters and captured on a 512 by 512-pixel Photometrics Evolve EMCCD camera. To prevent higher-order excitation during photoactivation, a pair of Uniblitz shutters controlled the laser beams such that samples were exposed to only one laser at a time. During imaging, the cells were given a 40-ms dose of 405-nm light every 90 s. Images were collected continuously with 40-ms imaging frames, and acquisitions lasted 5 - 7 min each.

6.2.6 Data Analysis

Recorded single-molecule positions were detected and localized based on point spread function fitting using our home-built code, Single-Molecule Accurate LocaLization by LocAl Background Subtraction (SMALL-LABS) [37]. This program reduces biases due to background subtraction, increasing the accuracy of each single-molecule localization. Subsequent localizations of the same molecule were then connected into trajectories us-

ing the Hungarian algorithm [118]. All trajectories from each movie for a given condition were combined and analyzed together using the NOnparametric Bayesian Inference for Anomalous diffusion in Single-molecule tracking (NOBIAS) algorithm [138]. This algorithm considers the collection of all the steps within all the trajectories and uses a Bayesian statistical framework to infer the parameters of interest including the number of mobility states and the diffusion coefficient and weight fraction of each state. A minimum of 25,000 steps were analyzed at each condition.

6.2.7 Chitosan Coverslip Coating

We applied a protocol previously published in Calkins et al. [2]. Briefly, chitosan powder (low molecular weight, deacetylated chitin, Sigma Aldrich) was added to a concentration of 2.5 % in 25 % v/v acetic acid in water and gently shaken overnight to fully dissolve. 500 μL of the solution was pipetted onto the center of an argon plasma-etched glass coverslip followed by spinning at 2000 rpm for 5 min to form a thin film of the chitosan solution on top of the coverslip. Coverslips dried overnight in an enclosed container and then washed with 1 % acetic acid in water then water and dried with air. Chitosan-coated coverslips were stored in an enclosed container for up to one month until use.

6.2.8 Chitosan-coated Coverslip Cell Sample Preparation

We applied a protocol previously published in Calkins et al. [2]. Briefly, *E. coli* cells in HDA media were pipetted into a hard plastic O-ring on a chitosan-coated coverslip and allowed to bind for 10 min. Media and unbound cells were removed without scratching the slide surface using a pipette. Fresh spent HDA media was immediately added to the O-ring (for the late-stationary study a maximum of 50 μL of solution was added to the ring to reduce background). The sample was placed on the microscope stage for single-molecule microscopy. To change the cell environment, media was pipetted out and a new media environment was immediately added to the O-ring. To induce oxidative damage in

cells, HDA media + 20 μM H_2O_2 was added.

6.3 Results

6.3.1 Dps Upregulation During Oxidative Damage in Live *E. coli* Cells on Chitosan-coated Coverslips

To establish the appropriate concentration of H_2O_2 to add to the *E. coli* cells and to confirm that Dps is upregulated in our sample preparation system as seen previously [158], I imaged a strain of *E. coli* that replaces Dps with mCherry at the *dpspro*. Therefore, mCherry expression is an indicator of expected Dps expression level: any condition that upregulates Dps expression will increase the mCherry fluorescence intensity. All experiments with H_2O_2 were performed in exponential phase cells. I found a significant increase in mCherry intensity after 1 hour at every concentration tested, and 20 μM H_2O_2 led to the highest intensity increase (Fig. 6.1a – h). The decrease in Dps expression at higher H_2O_2 concentrations could be due to declining cell health after exposure to higher concentrations. Previous work have seen a correlation between increasing concentrations of H_2O_2 and declining cell health including slowing of growth during exposure [8, 158]. Previous studies monitored the intensity of Dps-mCherry fusion proteins in *E. coli* cells immobilized on agarose pads and found increased Dps expression levels upon exposure to H_2O_2 that increased as H_2O_2 concentrations increases from 10 − 100 μM [158]. On the other hand, I found that the mCherry expression increased with H_2O_2 concentration until 20 μM and then decreased at higher concentrations (Fig. 6.1h). I attribute this non-monotonic trend in my experiments to the difference in strains monitored. In particular, I found that the Dps-mCherry fusion produces a non-functional copy of Dps which could lead to differences in cell response to peroxide. Fig. 6.2 shows aggregates of Dps-mCherry in cells rather than diffuse protein throughout the cell as would be typical of a functional protein. Therefore, I decided to monitor mCherry alone, unlike the previous study [158]. Addition-

ally, I believe the chitosan-coated coverslip method to be an improvement from previous studies due to the methods ability for consistency in H_2O_2 exposure. The previous study design produced high variability in H_2O_2 concentrations across the agarose pad and while this variability was accounted for in the calculation of intensity, it is more reliable to eliminate this problem all together. The chitosan-coated coverslips method allows all cells to be equally exposed to the environment condition and therefore does not add to cell-to-cell variability. I used a more functional reporter and a more reliable sample preparation method than previous studies; therefore, I have more confidence in this non-monotonic trend than in the previously reported results. Because 20 μM H_2O_2 induced the largest increase in Dps expression, I used that concentration for single-molecule studies.
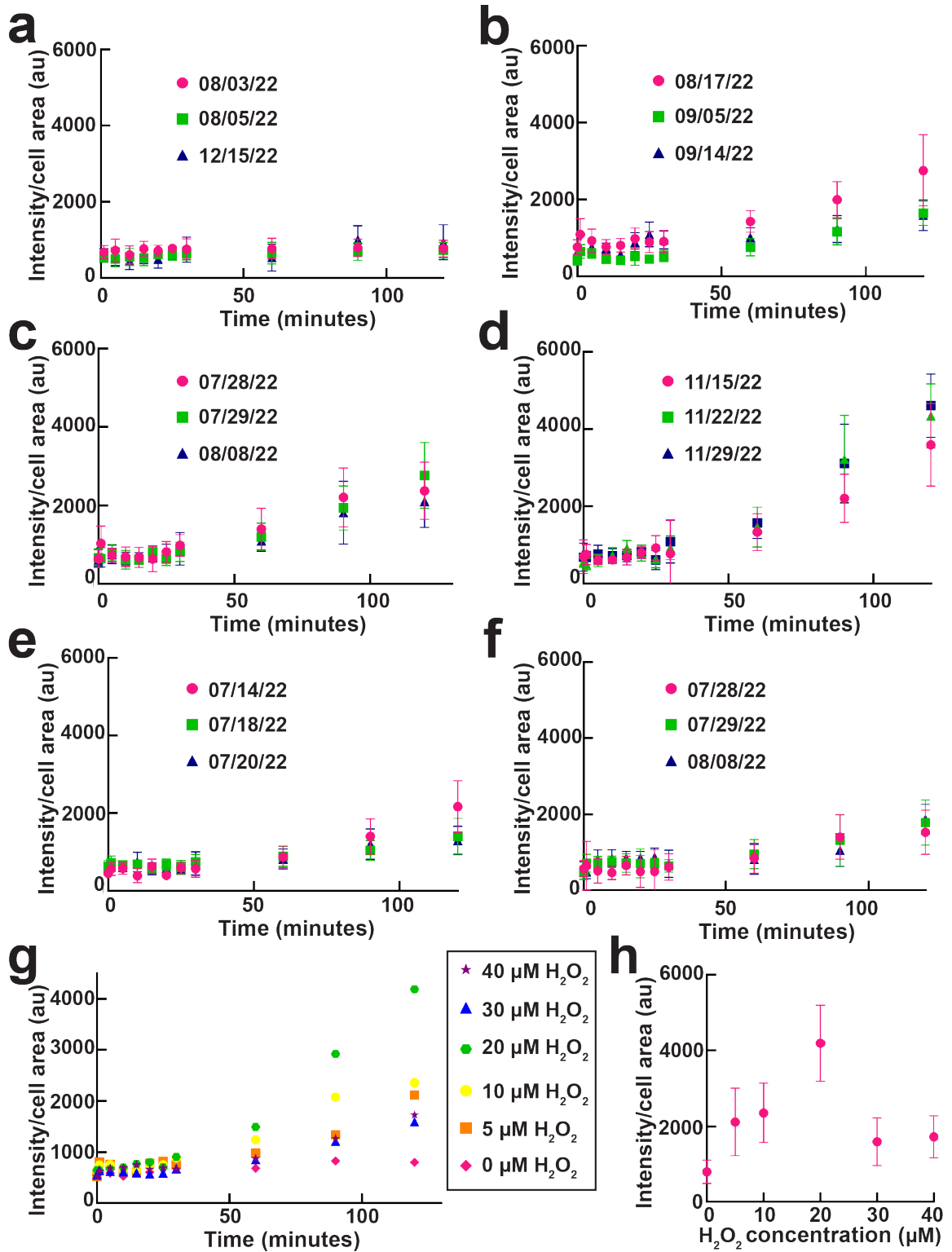
Figure 6.1: *Dps$_{pro}$* response to hydrogen peroxide. Caption on next page.

Figure 6.1: Average mCherry intensity per cell area for minimum $N = 50$ cells at each indicated time point after switching media to one containing the indicated concentration of H_2O_2. Samples were imaged constantly for 120 minutes and the average mCherry intensity was determined for each cell and then binned into 5-minute intervals. Cells imaged between 0 and 4.9 minutes after adding H_2O_2 were added to the 1-minute bin. Cells imaged between 5 and 9.9 minutes after adding H_2O_2 were added to the 5-minute bin and so on. Each data set includes 3 biological replicates. a) 0 μM H_2O_2, b) 5 μM H_2O_2, c) 10 μM H_2O_2, d) 20 μM H_2O_2, e) 30 μM H_2O_2, f) 40 μM H_2O_2. g) Average of 3 biological replicates from panels a-f. h) Average mCherry intensity per cell area for at least $N = 100$ cells at 120 min after switching media to one containing the indicated concentration of H_2O_2.
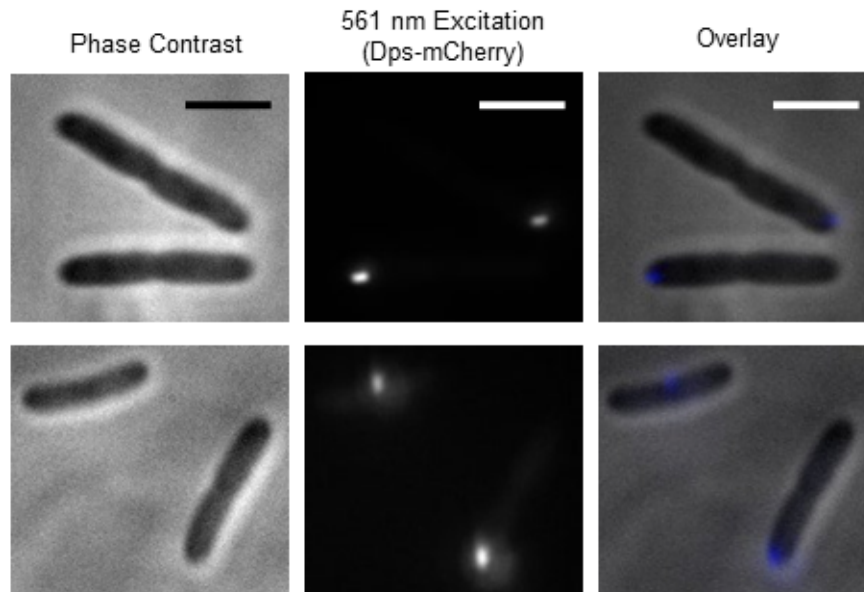
Figure 6.2: The Dps-mCherry fusion is non-functional when expressed as the only Dps copy. Examples of cells with Dps-mCherry fusion expressed at the native locus. Non-functional Dps-mCherry aggregates were observed in all cells. Scale bars: 2 μm.

6.3.2 The *E. coli* Nucleoid does not Compact After Exposure to Hydrogen Peroxide

Wild-type *E. coli* cells were stained with SYTOX orange and immobilized on a chitosan-coated coverslip. The fluorescence image of this nucleic acid-staining dye was used to measure the area of the nucleoid of the cell by measuring the area of 50% of the max of the emission intensity. The area of the whole cell was determined from the phase-contrast image using Cellpose [159]. By dividing the area of the nucleoid by the area of the cell,

I calculated the nucleoid occupancy (Fig. 6.3a). The nucleoid occupancy describes how compact the nucleoid is: as the value decreases, the nucleoid of the cell is more compact. After adding 10 μM H_2O_2 to the stained cells on the chitosan coverslip, I imaged cells for 2 hours and cells were binned in 5-minute intervals. This experiment was performed with three biological replicates and at least 100 cells per time point. The average nucleoid occupancy does not decrease over the course of 120 minutes after exposure to 10 μM H_2O_2 (Fig. 6.3b) despite increased Dps expression (Fig. 6.1c). It can be concluded from this result that Dps does not compact the nucleoid of exponential-phase *E. coli* cells during oxidative damage [160].

Using a Baclight live/dead assay, I found that despite the hollow appearance of the cells in the phase contrast images, a typical cell morphology marker for poor cell health or death, after exposure to 10 and 30 μM H_2O_2, most cells do not die after 120 min (Fig. 6.4). I measured the cell health by monitoring the fluorescence intensity from two dyes: SYTO 9, which permeates all bacterial cell membranes, was excited at 488 nm to indicate all cells in the blue channel, and propidium iodide, which permeates only bacteria with damaged membranes, was excited at 561-nm to indicate dead cells in the green channel. Based on the observed cell morphology and non-monotonic trend from the mCherry experiment (Fig. 6.1h), I hypothesized 60 - 80% of cells would be dead after H_2O_2 exposure. However, only 9 % of cells were dead after 120 min exposure to 10 μM H_2O_2 and only 19 % of cells were dead after 120 min exposure to 30 μM H_2O_2. Therefore, I expect both the increased Dps expression and lack of nucleoid compaction are due to a regulated stress response, not cell death. The lack of cell death has also been noted in the literature where growth while slowed continued for cells in $10 - 50$ μM H_2O_2 [158].
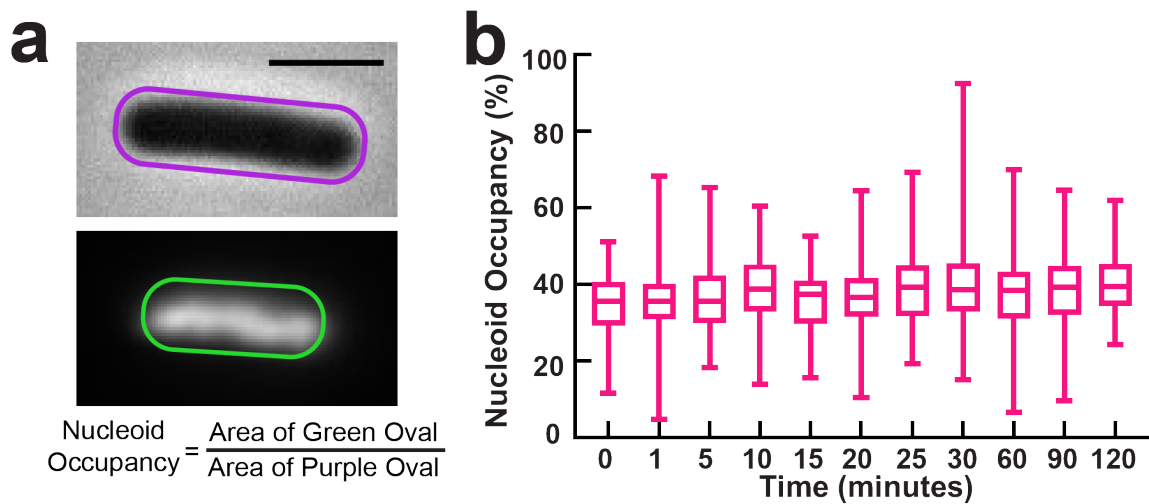
Figure 6.3: No nucleoid compaction in response to hydrogen peroxide. a) Nucleoid occupancy measurement. Brightfield phase-contrast image of a living *E. coli* cell (top) and fluorescence image (bottom) after SYTOX Orange DNA stain. Scale bar 2: μm. b) Nucleoid occupancy for N = 100 cells at each indicated time point after switching media to one containing 10 μM H_2O_2. Samples were imaged constantly for 120 minutes and the nucleoid occupancy was determined for each cell and then binned into 5-minute intervals. Cells imaged between 0 and 4.9 minutes after adding H_2O_2 were added to the 1-minute bin. Cells imaged between 5 and 9.9 minutes after adding H_2O_2 were added to the 5-minute bin and so on. The box indicates the middle 50 % of the data set and the middle line indicates the median. The horizontal lines indicate the minimum and maximum of each total data set.
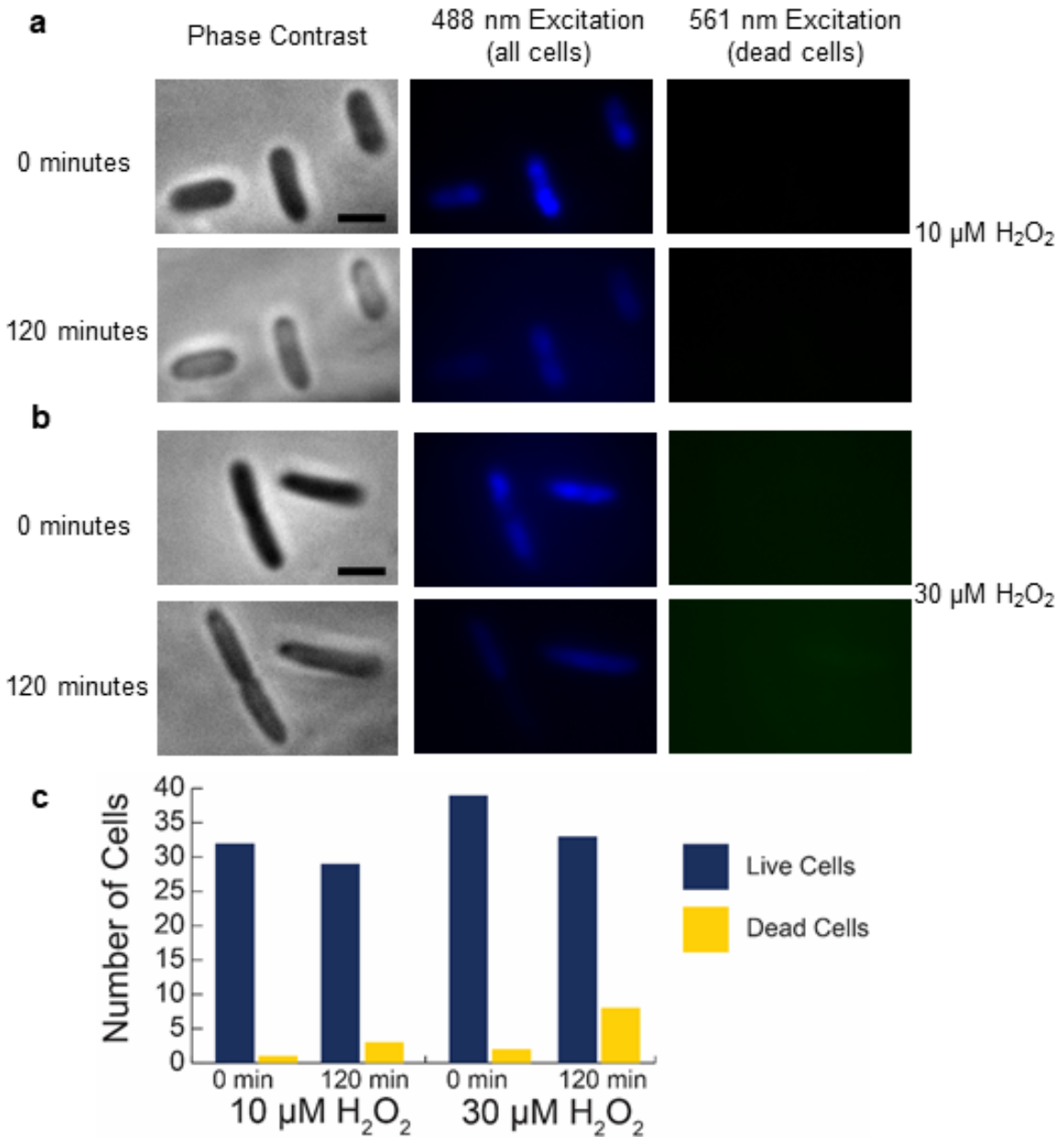
Figure 6.4: Live/dead cell assay of cells exposed to hydrogen peroxide. Comparing the health of *E. coli* cells immobilized on chitosan-coated coverslip before addition of H_2O_2 and 120 minutes after changing cell environment to H_2O_2 in HDA at the indicated concentration. 488-nm illumination: SYTO9 dye, which permeates all cells (false-colored blue). 561-nm illumination: propidium iodine dye, which permeates only dead cells (false-colored green). a) Examples of cells that are alive before and 120 minutes after exposure to 10 μM H_2O_2. b) Examples of cells that are alive before and 120 minutes after exposure to 30 μM H_2O_2. c) Cell viability before addition of H_2O_2 and 120 minutes after changing cell environment to H_2O_2 in HDA at the indicated concentration. Dead cells: all cells detected by in both the 488- and 561-nm channels. Live cells: all cells detected only in the 488-nm channel. Data for 10 μM H_2O_2 was previously published in part in Calkins et al. [2].

6.3.3 Effect of Hydrogen Peroxide on Dps-PAmCherry Dynamics in Living *Escherichia coli* Cells in Real Time

With cells mounted on chitosan-coated coverslips, I analyzed Dps-PAmC motion in *E. coli* cells containing a genomic copy of Dps. I found that the Dps-PAmC molecules move in three distinct diffusion states: most molecules diffuse rapidly and a small number move moderately or slowly (pink, navy, and green respectively, cross hairs in Fig. 6.5a). Average diffusion coefficients are shown in Table 6.2. We hypothesize the rapidly diffusing molecules correspond to freely diffusing Dps-PAmC due to the value of its average diffusion coefficient (0.514 μm^2/s). Based on our knowledge of the role of Dps, we attribute the moderately diffusing molecules to transient interactions with DNA and the slowly diffusing molecules to molecules bound to DNA. However, this hypothesis needs further investigation.

After 120 minutes of exposure to 20 μM H$_2$O$_2$, the fastest state (pink) decreases in weight fraction while the slower states (navy and green) increase (Fig. 6.5a). Additionally, I examined Dps-PAmC diffusion after 96 hours of starvation. I found that the fastest state dramatically decreases in weight fraction (Fig. 6.5b). The change in weight fraction from exposure to 20 μM H$_2$O$_2$ is small in comparison to the change in weight fraction from starvation (16% change vs 51% change). This indicates that Dps response to H$_2$O$_2$ differs from its response during starvation. To explore this further, I also examined the dynamics of Dps-PAmC every 5 minutes after changing the media to spent HDA with 20 μM H$_2$O$_2$. I found the small decrease in the weight fraction of the fast group (pink) occurs at 1 minute and oscillates throughout the 120-minute period (Fig. 6.6 and Fig. 6.7). This change in weight fraction was not due to changes in the solution (Fig. 6.8). This indicates that Dps must employ a rapid response, like acting as a catalyst for the chemical reduction of H$_2$O$_2$, rather than a slow response, such as binding DNA and compacting the nucleoid. We hypothesize the small reduction in weight fraction of the fast state could be due to a few proteins binding DNA, but not due to slowing from the catalytic action. Addition-

ally, since the decrease over the first few minutes does not continue for the 120-minute period studied, we believe that Dps chemically reduces and eliminates H_2O_2. If H_2O_2 was still present, we would expect a continued decrease in the fast state weight fraction. The oscillatory pattern (Fig. 6.7) could also point to chemical reaction of H_2O_2, but further studies measuring the change in H_2O_2 over the 120-minute period are necessary. All of these results lead us to believe Dps uses a chemical response to oxidative damage, not a physical shielding response. I also confirmed that the genomic copies of Dps are still functional in the Dps-PAmC *E. coli* strain. Dps is still able to compact the nucleoid after 96 hours of starvation (Fig. 6.9 purple, median nucleoid occupancy decreases from 31.8% to 24.1%) in the Dps-PAmC *E. coli* strain. I observe slightly less compaction in this strain than with the wild-type strain (Fig. 6.9 pink, median nucleoid occupancy decreases from 41.8% to 30.7%). I hypothesize this is due to the already increased compaction seen from the over-expression of Dps. This indicates the Dps-PAmC copy is also functional despite the fusion. However, further functionality tests are needed.
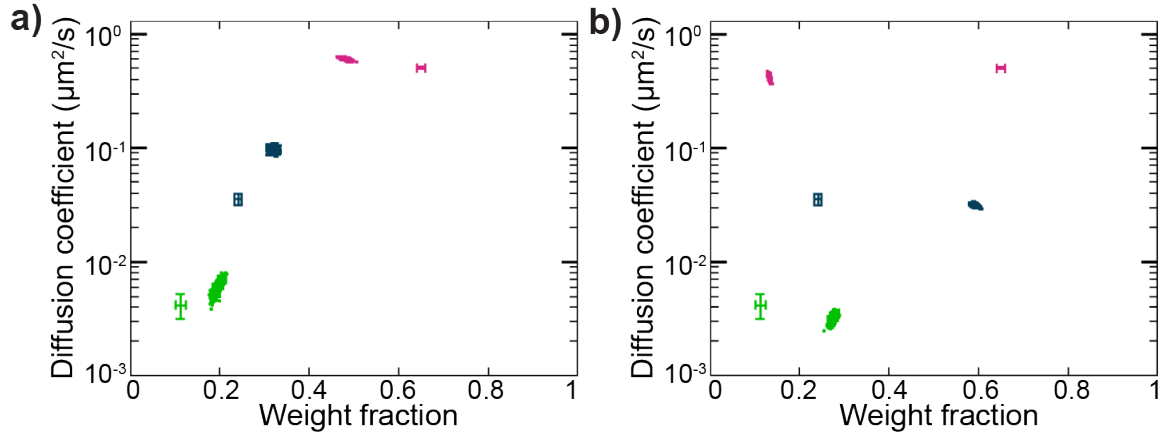
Figure 6.5: Dps-PAmCherry dynamics changes after oxidative damage vs. starvation. Average single-molecule diffusion coefficients and weight fraction estimates for Dps-PAmC in live *E. coli pMMB67EH-dps-PAmCherry* cells immobilized on chitosan-coated coverslips a) at 120 min after exchanging in situ to cell media containing 20 μM H_2O_2 at 0 min and b) after 96 hours of growth without added nutrients. The data for Dps-PAmC diffusion grown for 3 hours (exponential phase), immobilized on chitosan coverslips, and imaged prior to exposure to 20 μM H_2O_2 are shown as cross-hairs on both plots. Single-step analysis identifies three distinct diffusion states (fastest to slowest: pink, navy, and green). Each point represents the average single-molecule diffusion coefficient vs. weight fraction of Dps-PAmC molecules in each distinct mobility state at each saved iteration of the Bayesian algorithm after convergence. The data sets each contain a) 55,121 steps from 9,006 trajectories, b) 51,085 steps from 6927 trajectories, and cross-hairs) 63,852 steps from 10,580 trajectories.
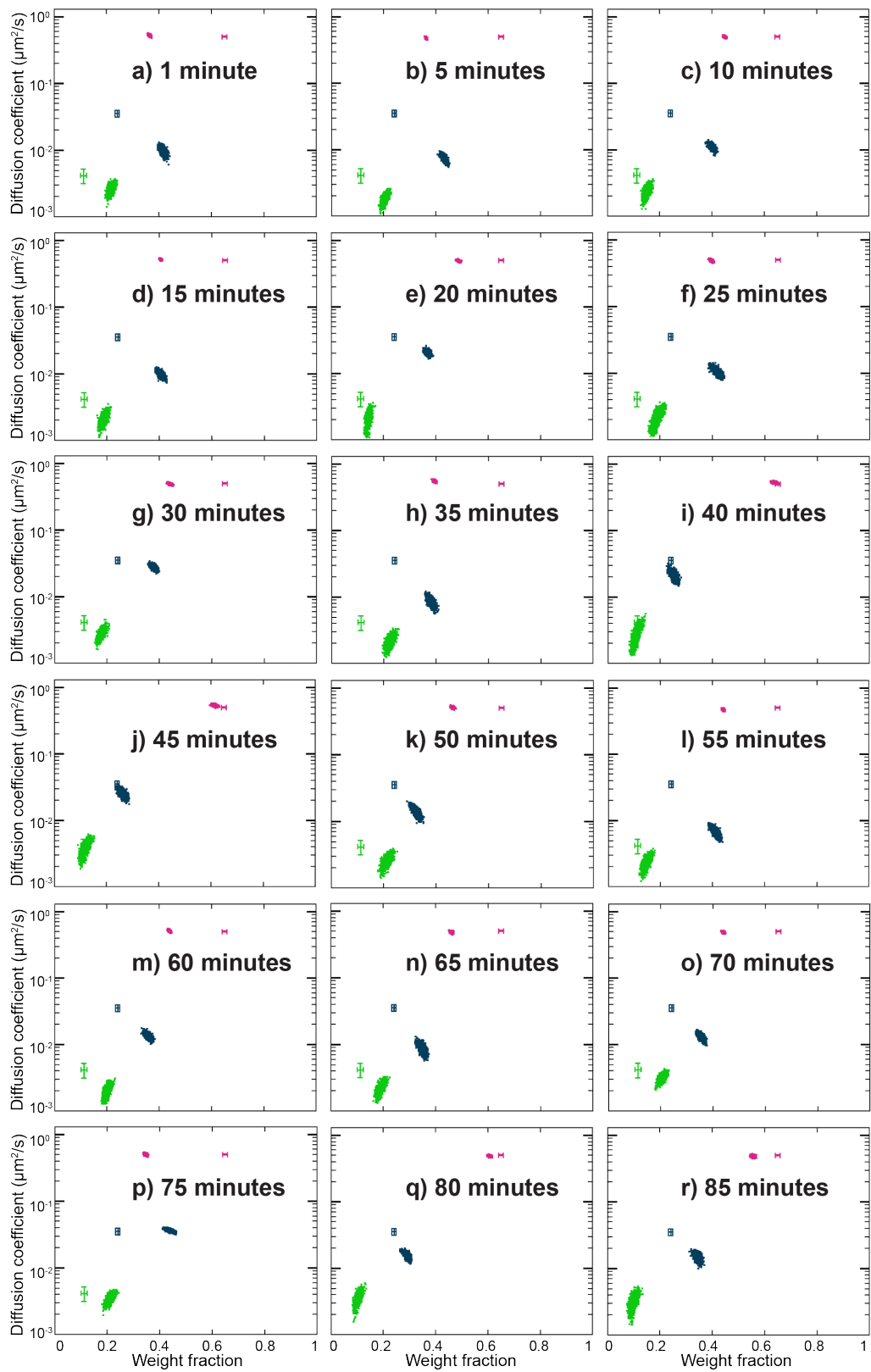
Figure 6.6: Dps-PAmCherry dynamics changes during real-time oxidative damage. Caption on next page.
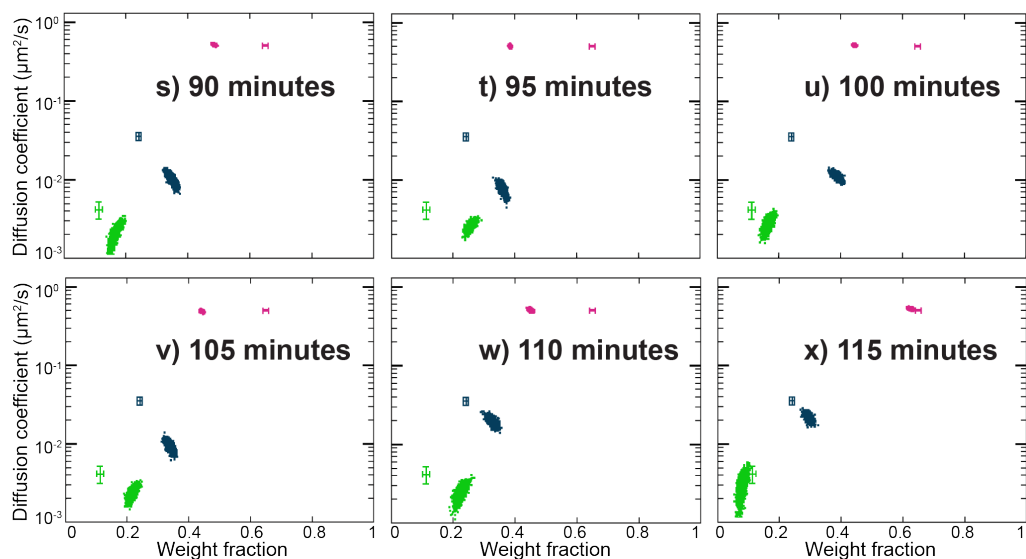
Figure 6.6: a-x) Average single-molecule diffusion coefficients and weight fraction estimates for Dps-PAmC in live *E. coli pMMB67EH-dps-PAmCherry* cells grown to exponential phase and immobilized on chitosan-coated coverslips. The cell media is exchanged to 20 μM H_2O_2 in HDA spent in situ at 0 min. Each time on the graph indicates the beginning time of data collection. Each data collection window is approximately 4 minutes after that indicated time. Single-step analysis identifies three distinct diffusion states (fastest to slowest: pink, navy, and green). Each point represents the average single-molecule diffusion coefficient vs. weight fraction of Dps-PAmC molecules in each distinct mobility state at each saved iteration of the Bayesian algorithm after convergence. The data sets each contain 6,566 – 20,857 steps from 1,107 – 2,971 trajectories. The data for Dps-PAmC diffusion grown to exponential phase, immobilized on chitosan coverslips, and imaged prior to exposure to 20 μM H_2O_2 are provided for reference (cross-hairs on all plots).
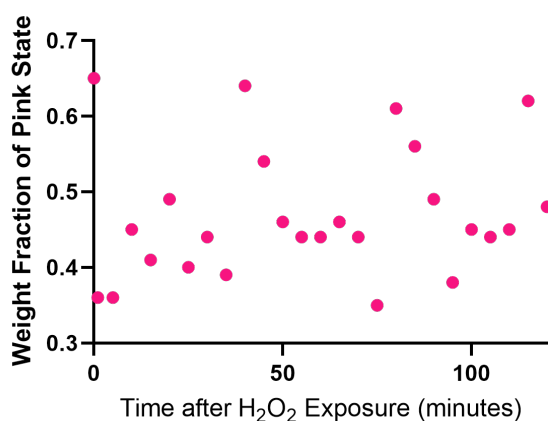
Figure 6.7: Dps-PAmCherry free moving molecules oscillate between binding and unbinding during oxidative damage. Weight fraction of the fast state (pink) at each time point in Fig. 6.6.
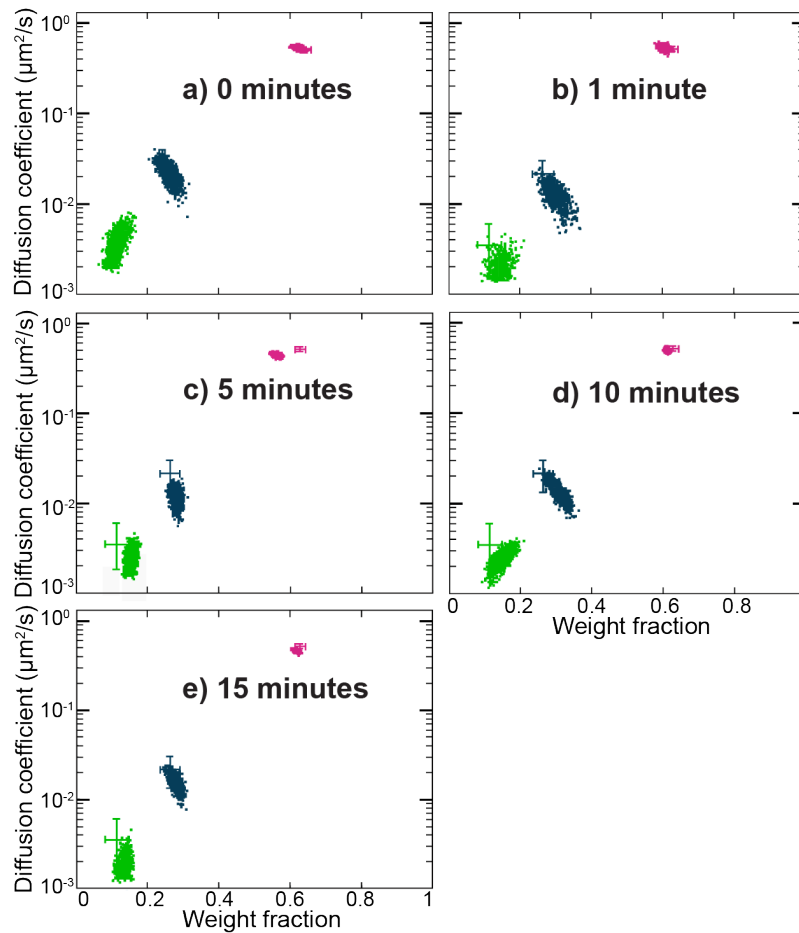
Figure 6.8: Dps-PAmCherry dynamics are unaffected by solution mixing. Average single-molecule diffusion coefficients and weight fraction estimates for Dps-PAmC in live *E. coli pMMB67EH-dps-PAmCherry* cells immobilized on chitosan-coated coverslips at a) 0 min b) 1 min c) 5 min d) 10 min and e) 15 min after exchanging media for fresh spent media with the same environment conditions. Each time on the graph indicates the beginning time of data collection. Each data collection window is approximately 4 minutes after that indicated time. Single-step analysis identifies three distinct diffusion states (fastest to slowest: pink, navy, and green). Each point represents the average single-molecule diffusion coefficient vs. weight fraction of Dps-PAmC molecules in each distinct mobility state at each saved iteration of the Bayesian algorithm after convergence. The data sets each contain between 10,791 - 19,364 steps from 1802 - 2685 trajectories. The data for Dps-PAmC diffusion grown to exponential phase, immobilized on chitosan coverslips, and imaged prior to exposure to 20 μM H_2O_2 are provided for reference (cross-hairs on all plots).
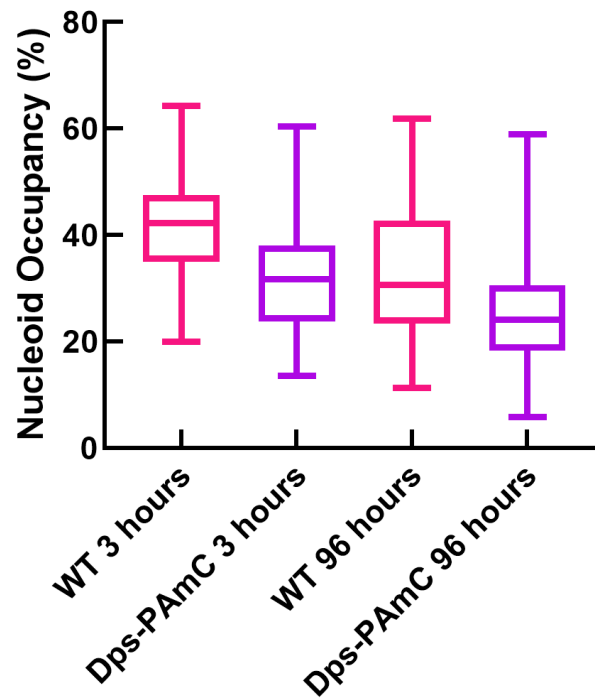
Figure 6.9: Dps-PAmCherry is a functional strain. Nucleoid occupancy for $N = 100$ cells under each indicated condition and strain (wild-type (WT), pink or *pMMB67EH-dps-PAmCherry*, purple). The box indicates the middle 50 % of the data set and the middle line indicates the median. The horizontal lines indicate the minimum and maximum of each total data set.

Table 6.2: Average diffusion coefficient and weight fraction for each diffusion state in this section's figures as indicated.

Figure	Condition	State Color	Diffusion Coefficient (μm^2)	Weight Fraction
6.5a (0 min)	Chitosan	pink	0.514 ± 0.010	0.65
6.5a (0 min)	Chitosan	navy	0.036 ± 0.002	0.24
6.5a (0 min)	Chitosan	green	0.004 ± 0.0005	0.11
6.5a (120 min)	Chitosan	pink	0.600 ± 0.001	0.48
6.5a (120 min)	Chitosan	navy	1.065 ± 0.004	0.32
6.5a (120 min)	Chitosan	green	0.043 ± 0.0006	0.20
6.5b (96 h)	Chitosan	pink	0.419 ± 0.016	0.13
6.5b (96 h)	Chitosan	navy	0.032 ± 0.001	0.59
6.5b (96 h)	Chitosan	green	0.003 ± 0.0001	0.28
6.6a (1 min)	Chitosan	pink	0.526 ± 0.012	0.36
6.6a (1 min)	Chitosan	navy	0.010 ± 0.001	0.42
6.6a (1 min)	Chitosan	green	0.003 ± 0.0003	0.22
6.6b (5 min)	Chitosan	pink	0.484 ± 0.009	0.36
6.6b (5 min)	Chitosan	navy	0.008 ± 0.0006	0.43
6.6b (5 min)	Chitosan	green	0.002 ± 0.0002	0.21
6.6c (10 min)	Chitosan	pink	0.503 ± 0.010	0.45
6.6c (10 min)	Chitosan	navy	0.011 ± 0.001	0.40
6.6c (10 min)	Chitosan	green	0.002 ± 0.0004	0.15
6.6d (15 min)	Chitosan	pink	0.521 ± 0.010	0.40
6.6d (15 min)	Chitosan	navy	0.010 ± 0.001	0.41
6.6d (15 min)	Chitosan	green	0.002 ± 0.0003	0.19
6.6e (20 min)	Chitosan	pink	0.495 ± 0.010	0.49
6.6e (20 min)	Chitosan	navy	0.021 ± 0.001	0.37
6.6e (20 min)	Chitosan	green	0.002 ± 0.0005	0.14
6.6f (25 min)	Chitosan	pink	0.493 ± 0.012	0.40
6.6f (25 min)	Chitosan	navy	0.011 ± 0.001	0.41
6.6f (25 min)	Chitosan	green	0.0004 ± 0.068	0.19
6.6g (30 min)	Chitosan	pink	0.498 ± 0.011	0.44
6.6g (30 min)	Chitosan	navy	0.028 ± 0.002	0.38
6.6g (30 min)	Chitosan	green	0.003 ± 0.0004	0.18
6.6m (60 min)	Chitosan	pink	0.517 ± 0.011	0.44
6.6m (60 min)	Chitosan	navy	0.013 ± 0.001	0.36
6.6m (60 min)	Chitosan	green	0.002 ± 0.0003	0.20
6.6s (90 min)	Chitosan	pink	0.516 ± 0.010	0.49
6.6s (90 min)	Chitosan	navy	0.010 ± 0.001	0.35
6.6s (90 min)	Chitosan	green	0.002 ± 0.0004	0.16

6.4 Conclusions

In this chapter, I describe the implementation of the new chitosan-coated coverslip method to study the effect of oxidative damage on Dps in live *E. coli* cells. I confirmed my sample preparation method can induce a response from additions of H_2O_2 by monitoring the intensity of mCherry on *dpspro* which can be correlated to Dps expression. I found that 20 μM H_2O_2 led to the greatest upregulation of the *dpspro* and all concentrations examined led to an upregulation starting at 30 minutes. I also found that despite this upregulation, Dps does not compact the nucleoid from WT conditions after 120 minutes of exposure to 10 μM H_2O_2. Both results agree with in vitro assays in the literature [8, 158] and confirm our ability to monitor changes in *E. coli* in response to oxidative damage using the new chitosan-coated coverslip method. It has been shown that oxidative damage triggers a different sigma factor than starvation in *E. coli* [155–157] and therefore, it was hypothesized that changes in Dps dynamics would differ following exposure to H_2O_2 relative to starvation. I found that changes in Dps-PAmC dynamics after 120 minutes of exposure to 20 μM H_2O_2 were slight in comparison to changes after 96 hours of starvation. Most notably, the fast state (pink, Fig. 6.5a) decreases in weight fraction from 65% to 48% after H_2O_2 exposure, but from 65% to 13% after starvation. Additionally, the change in dynamics after exposure to 20 μM H_2O_2 was immediate (observed at 1 minute). The rapidness of this change was surprising and would not be detectable with traditional sample preparation methods. These two results, the slight and immediate change in dynamics, indicate that Dps relies on a rapid chemical reaction to respond to oxidative stress rather than a binding mechanism. Many follow-up experiments are needed to investigate what biochemical function the two slower states correspond to and what the decrease in the fast state weight fraction corresponds to. These future experiments should include measuring the change in H_2O_2 concentration on the slide over the course of the 120-minute experiment, examining Dps-PAmC dynamics past the 120-minute time frame to determine if the 0-minute dynamics are recovered, and performing full Dps-PAmC functionality assays [146].

CHAPTER VII

Development of a Microfluidic Device for Single-molecule Fluorescence Imaging in Live Bacteria Cells

Some of the work presented in this chapter was previously published in Analytical Chemistry including Figures 7.6 and 7.7 and Table 1.

7.1 Introduction

As a second solution to the sample preparation limitations for fluorescence imaging in live bacteria, I developed a microfluidic device. Microfluidics describes an area of biotechnology that uses micron-sized channels to move small volumes of liquid in small devices. These devices have grown exponentially in the past two decades in biotechnology research because they cut costs and decrease experiment time. This ability is predominantly

due to their small volume requirements, low cost materials, and high-throughput capabilities [40, 41, 161]. Because of these benefits over the past two decades, microfluidic designs have been developed for imaging and single-cell manipulations, including trapping bacteria cells [41, 162–164]. Designs include use of u-shaped traps or restricted channels to immobilize bacteria cells for further analysis [43, 165–169]. Although many designs have aided single-cell fluorescence imaging experiments, none have been used for single-molecule fluorescence imaging. I believe these designs can be adapted for use with single-molecule imaging and add the ability to change cellular environment in real-time on the microscope to the toolbox of traditional sample preparation methods.

To match the features of the gold standard sample preparation for single-molecule imaging in live bacteria cells, there are several requirements for a microfluidic device. First, the device should allow cells to remain alive, so it must be made of non-toxic, breathable materials. Along similar lines, the cell immobilization process should not inhibit natural cell function. The goal is to understand biological mechanisms in functioning cells; therefore, we don't want any interference with those biological mechanisms. Additionally, considerations need to be made for the microscope elements, including the use of clear materials that won't interfere with fluorescent signal. The bottom of the device must be a 0.17 mm glass coverslip to maintain the focal length of the microscope objective. Finally, the design must include channels for media and air exchange to change the cell environment while on the microscope. This exchange should not disrupt the cell immobilization.

A device described by Baltekin et al. addresses all of these requirements: the "mother machine" shown in Fig. 7.1a monitors cell growth over long periods of time [43]. The device features large (20 − 40 μm) channels perpendicular to a cell trap area. The cell trap area is series of narrow (1.3 μm) channels partially blocked on one end. These channels can be adjusted in width according to the dimensions of the cells to be studied. Cells are flowed into the cell trap area through the large channels and pushed into the small channels. Cells are not able to leave the small channels because of the partially blocked end as shown in
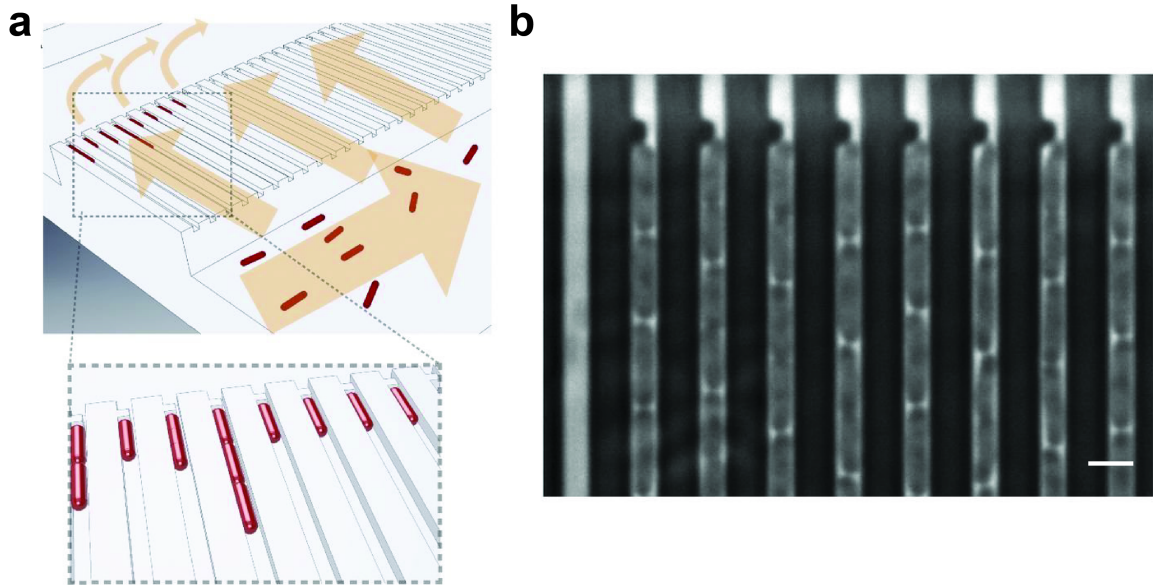
Figure 7.1: Microfluidic device design inspiration. a) Cartoon illustrating the loading of rod-shaped bacterial cells (red) into cell traps. Arrows indicate flow direction during loading. b) A small part of a phase-contrast image taken at 100x showing the back end of the cell trap, where the flow restriction region captures the cells during loading. Scale bar: 2 μm. Reproduced from Baltekin et al., reference [43].

Fig. 7.1b. The flow pattern is shown in Fig. 7.1a. I adapted this mother machine design to address the requirements of single-molecule imaging in *Vibrio cholerae* (*V. cholerae*) cells, which are smaller and more curved than the *Escherichia coli* (*E. coli*) cells for which the original device was designed, including decreasing the channel size and optimizing the connectivity between large and small channels. Other microfluidic device designs were considered, but never fabricated and tested [165, 166].

7.2 Materials and methods

7.2.1 Bacterial Strains and Growth Conditions

The two *V. cholerae* strains used here were all in the O395 classical biotype background. Strains used in this study were WT and *tcpP-PAmCherry*. All construct development was previously published [1]. *V. cholerae* strains were grown overnight at 37 °C on lysogeny broth (LB) plates containing streptomycin (strp) (100 μg mL^{-1}). Then, an individual colony

115

was picked and grown overnight in LB + strp medium under virulence-inducing conditions. 50 μL of overnight culture was added to 4 mL of LB + strp + pluronics (3 g/L, F127 Sigma Aldrich). This dilution was done three times and culture tubes were placed at appropriate temperature for 6 – 7 hours until cells reached mid-log phase. The entire 4-mL culture for all three tubes was centrifuged at 5000 rpm for 1.5 min. Cells were resuspended in 1 mL LB + strp + pluronics and combined. This concentrated cell stock was used on device.

7.2.2 Single-molecule Microscopy

A minimum of 50 cells per condition were imaged at room temperature using an Olympus IX71 inverted epifluorescence microscope with a 100X 1.40-NA oil-immersion objective, a 405-nm laser (Coherent Cube 405-100; 50 W/cm^2) for photoactivation, and a coaligned 561-nm laser (Coherent-Sapphire 561-50; 210 W/cm^2) for fluorescence excitation. Fluorescence emission was filtered with appropriate filters and captured on a 512-by 512-pixel Photometrics Evolve electron multiplying charged-couple detector (EMCCD) camera. To prevent higher-order excitation during photoactivation, a pair of Uniblitz shutters controlled the laser beams such that samples were exposed to only one laser at a time. During imaging, the cells were given a 40-ms dose of 405-nm light every 90 s. Images were collected continuously every 40 ms, and acquisitions lasted 5 – 7 min each.

For LB media imaging with both traditional sample preparation and microfluidic device sample preparation, a pre-bleach step was added to the single-molecule imaging protocol. The sample was simultaneously exposed to a 488-nm laser (Coherent-Sapphire 488-50; 210 W/cm^2) and a coaligned 561-nm laser (Coherent-Sapphire 561-50; 210 W/cm^2) for 7 min (traditional sample preparation) or 1 min (microfluidic device sample preparation) to reduce background fluorescence.

7.2.3 Data Analysis

Recorded single-molecule positions were detected and localized based on point spread function fitting using our home-built code, Single-Molecule Accurate LocaLization by LocAl Background Subtraction (SMALL-LABS) [37]. This program reduces biases due to background subtraction, increasing the accuracy of each single-molecule localization. Subsequent localizations of the same molecule were then connected into trajectories using the Hungarian algorithm [118]. All trajectories from each movie for a given condition were combined and analyzed together using the Single-Molecule Analysis by Unsupervised Gibbs sampling (SMAUG) algorithm [38]. This algorithm considers the collection of all the steps within all the trajectories and uses a Bayesian statistical framework to infer the parameters of interest including the number of mobility states and the diffusion coefficient and weight fraction of each state. A minimum of 25,000 steps were analyzed at each condition.

7.2.4 Traditional (Agarose Pad) Cell Sample Preparation

A 1.5-μL droplet of concentrated cells was placed onto an agarose pad (2% agarose (Fisher Bioreagents) in LB + strp at appropriate pH, spread and flattened on a microscope slide) and covered with an argon plasma-etched coverslip. Imaging was performed within 1 hour of making the agarose pad and assembling the sample.

7.2.5 Microfluidics Device Fabrication

The device master was formed with dual-layer fabrication on a 4-inch silicon wafer (University Wafer). The first layer was patterned in SPR 220 photoresist (Kayaku) and exposed for 50 ms with projection lithography. The wafer was then etched with Ar, HBr, Cl$_2$, and O$_2$, He gases using reactive ion etching for 285 s to a depth of 1.4 μm. The photoresist pattern was subsequently removed with acetone. The second layer was patterned in SU8 photoresist spun at 4000 rpm for 90 s to form a 40-μm deep layer and exposed for

70 s after alignment between the mask and the first layer. The fabricated master wafer was silanized using (TriDecaFluoro-1,1,2,2-TetraHydroOctyl)TriChloroSilane (Gelest) for 2 hours. Polydimethylsiloxane (PDMS) (RTV615) was made in a 10:1 ratio with the curing agent (Momentive), vacuumed for 15 min to remove air bubbles, poured over master wafer, and baked overnight at 70 ℃. Individual devices were cut from the wafer and bonded channel side down on a glass coverslip after 40 s exposure to an argon plasma. Bonded devices were left overnight at 70 ℃ to improve the quality of the bonds.

7.2.6   Microfluidic Device Microscopy Cell Sample Preparation

762-μm plastic tubing (Cole-Parmer) was inserted into the four inlets and outlets in the large channels. Two 10-mL syringes (BD) were filled with LB media + pluronics and inserted in the top and bottom left side inlets. 0.5 mL of media was manually injected into the inlets one at a time. The outlet lines were checked for media flow. A syringe was loaded with *V. cholerae* cells in LB media + pluronics. The cell-loaded syringe was inserted into the top left inlet, replacing the LB-filled syringe. The device was then placed on the microscope platform and the inlet syringes were placed in a syringe pump (Instech Pump 11 Elite). The contents of both syringes were injected by the syringe pump at 5 μL/min for 1 hour. The device was examined for cells in the small channels. Once over half of the channels had at least 5 cells, the device was placed overnight in a warm room at 30 ℃ with flow at 5 μL/min. After a minimum of 12 hours, the device flow was stopped while the syringes remained connected. 2 – 3 hours later, the device was removed from the warm room and placed on the microscope platform for inspection. If cells appeared immobilized, single-molecule imaging and tracking was performed.

7.3   Microfluidic Device Fabrication and Process Optimization

To fabricate the microfluidic device, masters were made using dual-layer photolithography on 4-inch silicon wafers (University Wafer). Fig. 7.2 shows a summary of the final
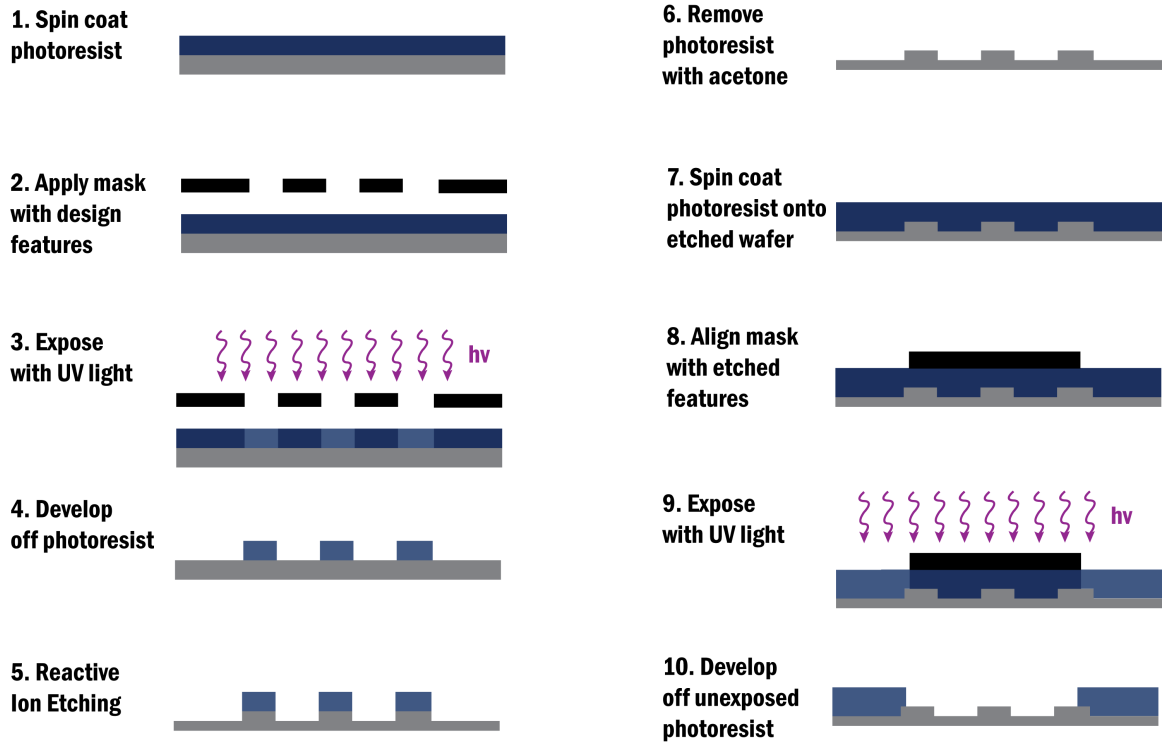
Figure 7.2: Microfluidic device fabrication procedure. Final fabrication process used to create master wafer for microfluidic devices.

fabrication process. First, a hexamethyldisilizane (HDMS) vapor prime was applied to a clean silicon wafer. This allows for better bonding between the photoresist and wafer forming cleaner channel edges. I found that masters made without the HDMS coating had large sections of photoresist removed after photoresist development not in areas intended in the design. Next, a thin 3-μm layer of SPR 220 (3.0) photoresist (Kayaku) was spun on the wafer. The photoresist was automatically dispensed using a CEE 200X spin coater (brewer science). The wafer was spun at 2000 rpm for 90 s to evenly distribute the photoresist. Then, the coated wafers were baked for 90 s at 115 °C. Wafers were subsequently cooled to room temperature.

For the final fabrication process, glass masks were used for both layer exposures; however, earlier device fabrications used a plastic printed mask for the second layer exposure and a glass mask for the first layer exposure. Glass masks were made using the Heidelberg mask maker by exposing the CAD file pattern onto a 5-inch square glass plate coated with

chromium and photoresist. Exposed masks were developed with AZ726 (MicroChemicals) for two 35 s periods using the CEE automated developer instrument (brewer science) (35-35DP recipe, Lurie Nanofabrication Facility (LNF) SOP). Developed masks were etched using the chrome etch bath on Mask Bench 13 (JST). Etched masks were stripped of photoresist using a heated nanostrip bath on Mask Bench 13. Masks were stored in the clean room until used for master fabrication.

To make small channel features, wafers were exposed to UV light using a AS200 AutoStep (GCA). This instrument uses projection lithography to expose features 5x smaller than the mask design. Therefore, a 5x mask was made with one set of small channels at 7 μm and funnels at 20 μm as well as alignment markers as described in Fig. 7.3b. The AutoStep instrument exposed for 0.50 s through this mask design onto the wafer by raster scanning, making 4 columns of 9 rows of sets of channels on the wafer. This exposure pattern method is currently installed as BITEEN1 on the instrument at the LNF. Exposed wafers were baked for 90 s at 115 ℃. Then, the wafers were developed in AZ726 for two 25 s periods using the CEE automated developer instrument (brewer science) (25-25DP recipe, LNF SOP). The revealed pattern has the small channels and alignment markers patterned in photoresist and the rest of the wafer was clean.

Developed wafers were mounted on a larger 6-inch silicon wafer using Santovac 5 sample mount solution. 80 μL of solution was pipetted in the center of a 6-inch wafer on a hotplate at 80 ℃. A patterned 4-inch wafer was placed on a movable mounting pin above the pipetted solution. The hotplate was sealed off using a vacuum pump. Once vacated of air, the movable mounting pin was removed, dropping the 4-inch wafer onto the mounting wafer, and the mounted wafer was left on the sealed hotplate for 5 minutes. The whole mounted wafer was removed from the hotplate. The bottom of the wafer was wiped clean with acetone. It is vitally important that the bottom of the mounting wafer is clean of all particulates before ion etching. This can be assessed by holding the back of the wafer parallel to your eyesight and tilting 5 ° up and down looking for white specs. Cleaned
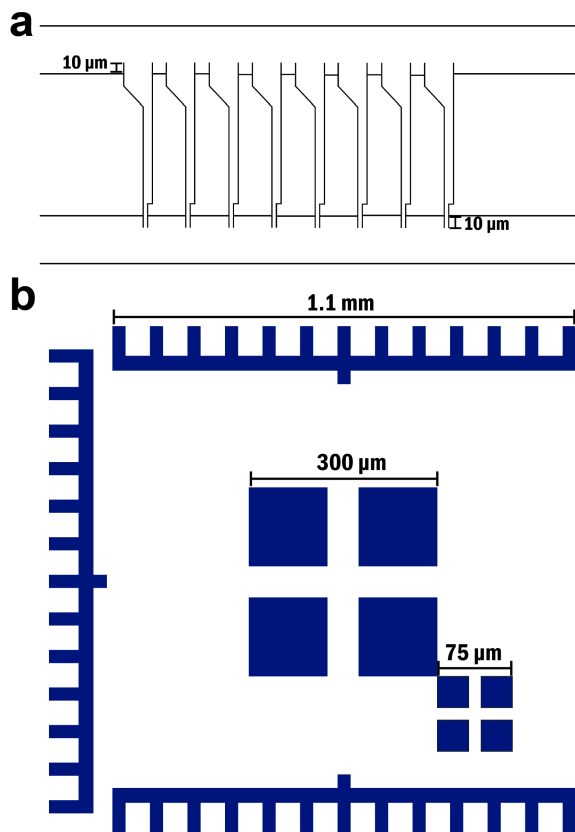
Figure 7.3: Alignment markers. a) Extension of small channel mask design into large channel mask design. b) Final design of alignment markers used in step 8 of the microfluidic device master fabrication process (Fig. 7.2).

wafers were placed in the P5000 RIE reactive ion etching instrument (Applied Materials) chamber C. Using the PolyPatBkm method (LNF SOP), Ar, HBr, Cl_2, and O_2He gases were used to etch exposed areas of the wafer (everywhere except the small channel design) for 285 s. Etched wafers were removed from the mounting wafer and the backs were cleaned with acetone to remove excess mounting solution. Then, wafers were washed with acetone thoroughly and placed in an acetone bath for 1 minute to remove any SPR 220 photoresist on the wafer. Immediately following the acetone bath, wafers were washed with isopropanol (IPA) and placed in an IPA bath for 1 minute. Subsequently, clean wafers were dried on a hotplate at 115 °C for 5 minutes and cooled to room temperature.

Next, a thin 40-μm layer of SU8 2050 photoresist was spun on the clean etched wafer. The photoresist was poured from a small bottle onto the wafer so a quarter-sized smooth drop forms in the middle. The wafer was spun at 4000 rpm for 90 s to evenly distribute the photoresist. Then, the coated wafers were baked for 5 minutes at 65 °C and 10 minutes at 95 °C. Wafers were subsequently cooled to room temperature. To make large channel features, wafers were aligned with the large channel mask (details on alignment procedure discussed in Section 7.4.1) and exposed to UV light using a MJB 45S Mask Aligner. This instrument uses contact lithography to expose features the same size as the mask design. Therefore, a mask was made with 4 rows of 9 sets of large 40 μm channels spaced precisely to match the AutoStep pattern. The instrument exposed the sample for 84 s according to lamp calibration set by the instrument technician. Exposed wafers were baked for 3 minutes at 65 °C and 7 minutes at 95 °C. Wafers were subsequently cooled to room temperature. Wafers were placed in a bath of the SU8 developer (1-Methoxy-2-propyl acetate) for 3 minutes and subsequently rinsed with SU8 developer. 2 – 3 drops of IPA were dropped on the edge of the developed wafer away from any features to test for any unexposed photoresist remaining. If the IPA drops turned cloudy, the wafer was placed in SU8 developer bath for an additional 45 s and then tested again. If the IPA drops stayed clear, the wafer was thoroughly rinsed with IPA. Finally, clean wafers were baked on a

hotplate at 115 ℃ for 5 minutes to dry out the wafer. These completed wafers serve as master molds for PDMS devices and were stored in the clean room in sterile petri dishes until used.

To form the actual device, the fabricated master wafer was silanized using (TriDeca Fluoro-1,1,2,2-TetraHydroOctyl)TriChloroSilane (Gelest) for 2 hours. PDMS was made in a 10:1 ratio with the curing agent (Momentive), vacuumed for 15 min to remove air bubbles, poured over the master wafer, and baked for 2 hours at 70 ℃. Glass coverslips were cleaned sequentially with acetone, IPA, then water and dried with pressurized air. Individual devices were cut from the wafer, and inlet and outlet plugs were punched with a 30-gauge flat tip needle. I found that small biopsy punches could also be used and provided cleaner, but larger punches. Punched holes were visually examined for PDMS punch removal. Cut devices were rinsed with IPA and dried with pressurized air. Once dry, devices were bonded channel side down on one of the cleaned glass coverslip after 40 s exposure to an argon plasma. Bonded devices were left overnight at 70 ℃ to improve the quality of the bonds. During the testing phase, devices were marked with a letter representing wafer used and a number representing the device in the column. Columns were numbered sequentially from the top down. Completed devices were stored in sterile petri dishes out of the clean room until used.

7.4 Microfluidic Device Fabrication Considerations

7.4.1 Alignment Markers

The most difficult step of the described master fabrication process is aligning the small channel layer etched onto the wafer with the large channel mask. I made several changes to the large channel mask design to make the process easier. First, I added large 20x1 mm boxes above and unconnected to each set of large channels. These boxes provide clear space on an otherwise black mask to look through during the initial alignment phase

instead of relying on the two 40-μm slits (large channels). Because they are unconnected to the channel design, they do not interfere with the physical device. Second, I extended the length of the small channels by 10 μm on either side (Fig. 7.3a). This added length increases the margin of error during the alignment step. This extension should not exceed the width of the large channel, so the small channel does not extend past the large channel after alignment. With the channel extension on the top, a bowl effect was created with the funnel and did not inhibit cell entrance. Finally, I added more complex alignment markers to aid the alignment process. Typically for alignment, a single simple cross is added to the mask of both layers in the exact same position [170]. The crosses are then matched up between the first layer on the wafer and the second layer mask before exposing the second layer. However, for such a small margin for error, this simple cross did not lead to a fully connected device after many attempts. Therefore, a more complex alignment marker was created following the design in Fig. 7.3b. The traditional cross is still used as the center feature of the design, but now instead of an identical cross on the large channel mask a set of 4 boxes are arranged in the shape of a cross of identical size. Therefore, the space for the cross is clear on the large channel mask, such that the cross etched on the wafer can be guided into the clear space and gaps in the overlap can be easily identified. A second smaller cross was added to the bottom right corner of the design to add more fine alignment. This cross was sized to within the margin of error set by the small channel length (10 μm). Lastly, a series of tick marks larger than both crosses were added on three sides of the crosses. These tick marks make the whole design non-symmetric, so the first layer and second layer are not 180° flipped from each other. Additionally, the ticks marks provide a larger-scale alignment before zooming into the crosses. The three marker sizes are used in sequence such that each additional marker provides finer alignment.

The whole alignment process is as follows. Secure the photoresist-coated wafer via vacuum on the adjustable wafer mount. Set the stage to "no contact" so the large channel mask does not interfere with the photoresist during alignment. Fit the large channel

mask on the mask holder and secure it above the wafer. Move the microscope, equipped with a 20x objective, to above the center of a clear box on the large channel mask for maximum visibility. Slowly adjust the knobs controlling the wafer stage to raster scan the area until a small channel alignment marker is in view. Move the microscope to the alignment markers on the large channel mask directly below the original clear box (note the mask does not move during the alignment process). Slowly move the wafer down until the alignment marks appear through the mask. If you are worried that you missed the alignment markers, return the microscope to the clear box and move up until a marker is found. Focusing on the tick marks, move the wafer into the correct position. It is OK if this alignment is not perfect, but this first round of positioning should provide a course alignment. Once the wafer tick marks align with the mask tick marks, refocus the objective so the middle cross-boxes are clear and move the wafer until there is no white space in the middle of the boxes. This alignment will make sure the large cross is as centered as possible. Repeat this process with the smaller cross. Finally, move the microscope to the area of the channels. The small channels can only be seen through the slits from the large channels on the mask and will appear as blurry dark features in the large channel area. Move the instrument into contact mode by pressing the contact button. The microscope will need to be refocused. Now, both the large channel mask and small channel features on the wafer are in the same focal plane and therefore should be clearly viewable in the microscope. You should be able to see both sides of the small channel ends in each of the large channels. If not, you can remove contact and move extremely slightly in the up or down direction as needed. Then, return contact and check for small channels again. Continue this process until you see channels in both sides. Do not move the sample while in contact mode because it will cause smudges in the photoresist and potentially stick the mask to the wafer surface, ruining both pieces. If you made more than one movement (in non-contact mode) after using the alignment markers, return the microscope to the small cross alignment marker and check for agreement. Once the alignment markers and small

channel position look good, check that the instrument is in contact mode and expose the wafer for 84 s. Follow the remainder of the fabrication procedure as described in Section 7.3.

After each alignment attempt, before and after perfecting the alignment procedure and markers as described above, the devices connections were visually inspected for connection. Fig. 7.4b-f displays the microscopy images of the PDMS devices made from the final master used to collect data as indicated in Fig. 7.4a. These images show the perspectives checked for visual inspection and confirmed alignment for this master. In addition to visual inspection, the final devices were checked for complete channel flow by adding 5 nM Cy5 dye in Phosphate Buffered Saline (PBS) to the top large channel inlet and PBS buffer with no dye to the bottom large channel inlet. Dye was detected using fluorescence excitation with a 561-nm laser. As shown in Fig. 7.4g, in successfully connected devices, dye was detected in the small channels; the fluorescence intensity and therefore the dye concentration is constant along the channel length. Therefore, there is successful connection between the small and large channels. Additionally, I did not observe a concentration gradient down the small channel, so the cells will only be exposed to one condition at a time.
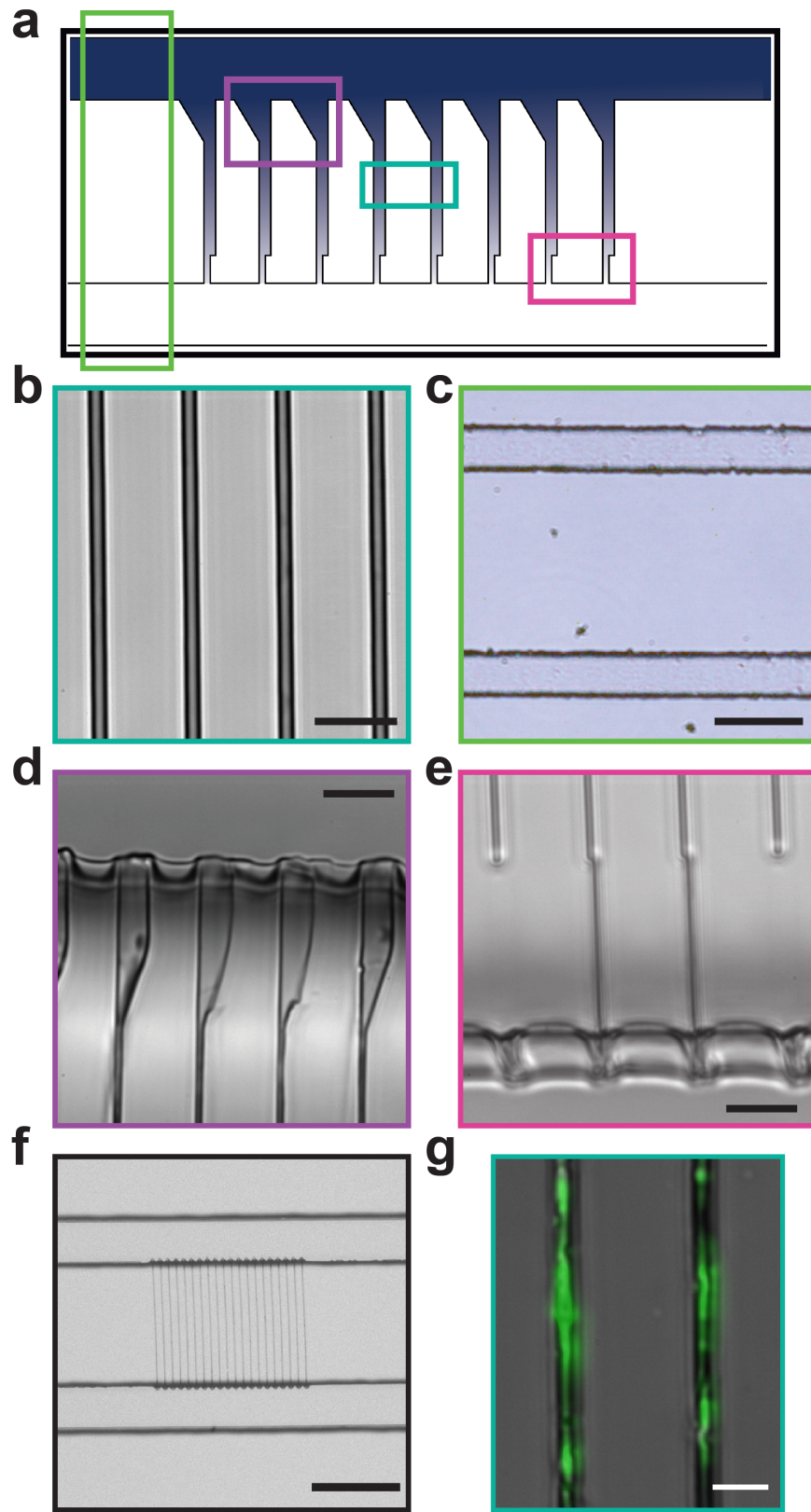
Figure 7.4: Microfluidic device images. Caption on next page.

Figure 7.4: a) Simplified microfluidic design schematic; not to scale. The boxes mark the regions of the device imaged in b-g; the colors of the boxes in b-g correspond to the color of the boxes in a. b) 100x magnification image of small (1.4-μm) channels. Scale bar: 10 μm. c) 10x magnification of large channels. Scale bar: 80 μm. d) 100x magnification image of connection between top large channel and small channel funnel. Scale bar: 10 μm. e) 100x magnification image of connection between bottom large channel and bottom of small channel including constriction of the small channel. Scale bar: 10 μm. f) 10x magnification image of device showing both large and small channels. Scale bar: 80 μm. G) 100x magnification of small channels. Fluorescence from 5 nM Cy5 dye (with 561-nm laser excitation) overlaid on the image of the channels. Scale bar: 5 μm.

7.4.2   Photoresist Exposure Time

The photoresist exposure time depends on the type and thickness of photoresist used. While manufacturers recommend an exposure time for each photoresist, this parameter may need to be adjusted for each exposure instrument used based on the voltage and lifetime of the bulb. Instrument technicians at LNF perform regular testing of bulb function and provide recommended exposure times. However, while the large channels are less affected by small imperfections from under- or over-exposure, the small channel size is very sensitive and channels that are too small can block the cells from entering into the small channels at all. Therefore, I found that more troubleshooting was necessary to improve channel quality when fabricating the small channels on the device master.

A 0.40-s exposure time was used for initial design testing based on technician recommendation. When generating a new design, wiggly small channels were observed in the device (Fig. 7.5a). To address this issue, wafers were exposed to the UV lamp for 0.40 s, 0.45 s, or 0.50 s when fabricating the small channels as described in Section 7.3. Wafers were developed and etched identically according to established protocol. After etching and before washing, wafers were examined with light microscopy at 20x magnification. As shown in Fig. 7.5, longer exposure times significantly improved the channel straightness. The 0.50-s exposure resulted in channels of similar quality to previous working channels and therefore that exposure time was used moving forward. It is believed that deterioration of the UV lamp used in the AutoStep instrument resulted in a need for longer exposures than

previously recommended.
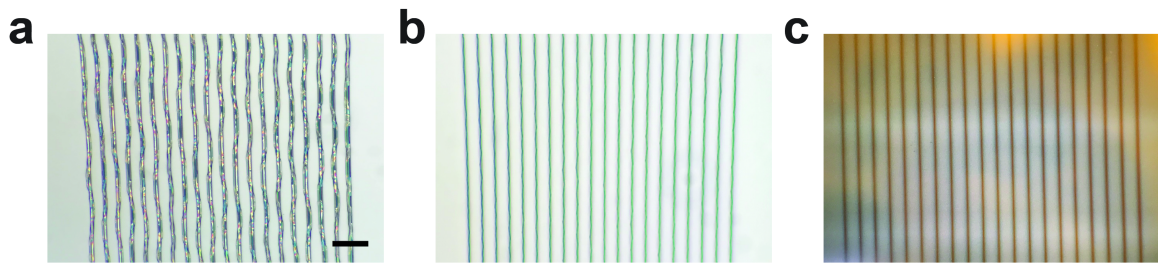
Figure 7.5: Microfluidic device small channel fabrication exposure time. 20x magnification image of small (1.4-μm) channels etched into a silicon wafer. The UV lamp exposure time was varied to reduce channel curvature. a) 0.40 s b) 0.45 s and c) 0.50 s. Scale bar: 30 μm.

7.4.3   Small Channel Size

Once I had troubleshooted all device fabrication issues, I moved on to improving the device design. Although a very similar device design had previously worked for *E. coli* cells, this device was not designed to be sensitive to cell health [42,43]: in previous studies, the protocol to load cells on the device requires either starving the cells to make them smaller or centrifuging the device to push cells into the channels by force. Both solutions have a profound impact on cell health and requires a long recovery period. Unfortunately, neither *E. coli* nor *V. cholerae* cells flow into 1.3-μm small channels from syringe pump-driven flow in the top large channels when they are in the exponential growth phase.

Since we care about the health of the cells at the time of loading in these single-molecule imaging experiments, I needed to adjust the channel design. Therefore, I increased the channel width from 1.3 μm to 1.5 μm, making the channel less constricting to *V. cholerae* cells. I was successfully able to flow *V. cholerae* cells from the large channel into the small channels and I detected single molecules in live bacteria cells; however, the cells were not well immobilized in these widened channels, and the cell wiggling decreased the accuracy of the single-molecule tracking data that I collected. Though this cell motion would not have been a concern for previous applications of this device, it is vital that the cells are stationary for single-molecule imaging and tracking. Therefore, I added

a 4-μm funnel to the top of the small channel and further constricted the small channel to 1.4 μm. The funnel created more open space at the large channel connection, increasing the likelihood of a bacteria cell entering the small channel and gradually guiding the cells into a smaller channel. The 1.4-μm channel decreased the movement of the cells, but they were not fully stationary. Therefore, I ultimately implemented a channel-filling protocol in which I grew cells on the device overnight to further fill the channel as the cells divide and to better immobilize them.

The device was filled in this ultimate protocol as follows: LB rich media was pushed through the top and bottom large channel until media was seen in both outlets and in a majority of the small channels as viewed through the eyepiece on the microscope using an 100x objective. Then, the top large channel syringe was switched to one containing 3 mL of concentrated exponential phase *V. cholerae* cells in LB media. Both channels were pumped at 5 μL/min for 2 hours using a syringe pump (Harvard Apparatus). The device was monitored on the microscope with a 100x objective using the camera (Photometrics Evolve). Cells appeared in the top large channel starting about 30 minutes into the pumping period. After two hours, pumping was stopped, but the syringes remained connected to the inlets. Once the flow in the channels slowed, about 15 minutes, cells were visible in the small channels. Once I saw cells in the small channels, the device (still connected to the syringe pump) was placed in the warm room at 30 ℃ overnight. The top channel syringe had 1 mL of cells remaining, and I added 4 mL of LB media to make a 5 mL dilute cell solution in the syringe. The bottom channel syringe was filled to 5 mL with LB media. Both channels were pumped overnight at 1 μL/min. In the morning, flow was stopped in both channels and the tubing was disconnected from both syringes. The device was left in the warm room for 2 hours. The device was examined on the microscope to look for cells filling the channels. If cells were stationary, cells were imaged using single-molecule imaging protocol detailed in section 7.2.2.

7.5 Single-molecule Fluorescence Imaging in Live *Vibrio cholerae* in a Microfluidic Device

After device design optimization, we could fill the small channels with *V. cholerae* cells via pumping, but the cells moved and wiggled in the channel. To address this issue, we grew cells in LB media on the device overnight to fill the channel space as the cells grew and divided. Still, cells grown in minimal media are thinner and fill the channel less well. We found that rich media was necessary to fill the channel densely enough for immobilization, and therefore all imaging on device was done in LB media. This overnight growth led to immobilized cells in the small channels (Video S1 in reference [2]). In the microfluidic device, we tracked fusions of the membrane-bound protein TcpP to the photoactivatable fluorescent protein PAmCherry (TcpP-PAmCherry (TcpP-PAmC)) in living *V. cholerae* cells in LB media at pH 6, and we found that the sensitivity required for single-molecule tracking was not inhibited by this sample preparation (Fig. 7.6c and Video S2 in reference [2]). We also found that, despite the microfluidic environment and the rich medium, the localization precision of molecules detected in cells in the device was comparable to that of single molecules in cells in minimal media mounted on agarose with a mean localization prevision of 45.2 ± 13.4 nm vs. 42.3 ± 12.3 nm for cells on device and on agarose, respectively (Fig. 7.7). The localization precision was calculated from the average 95% confidence interval on the Gaussian fit to the point spread function.
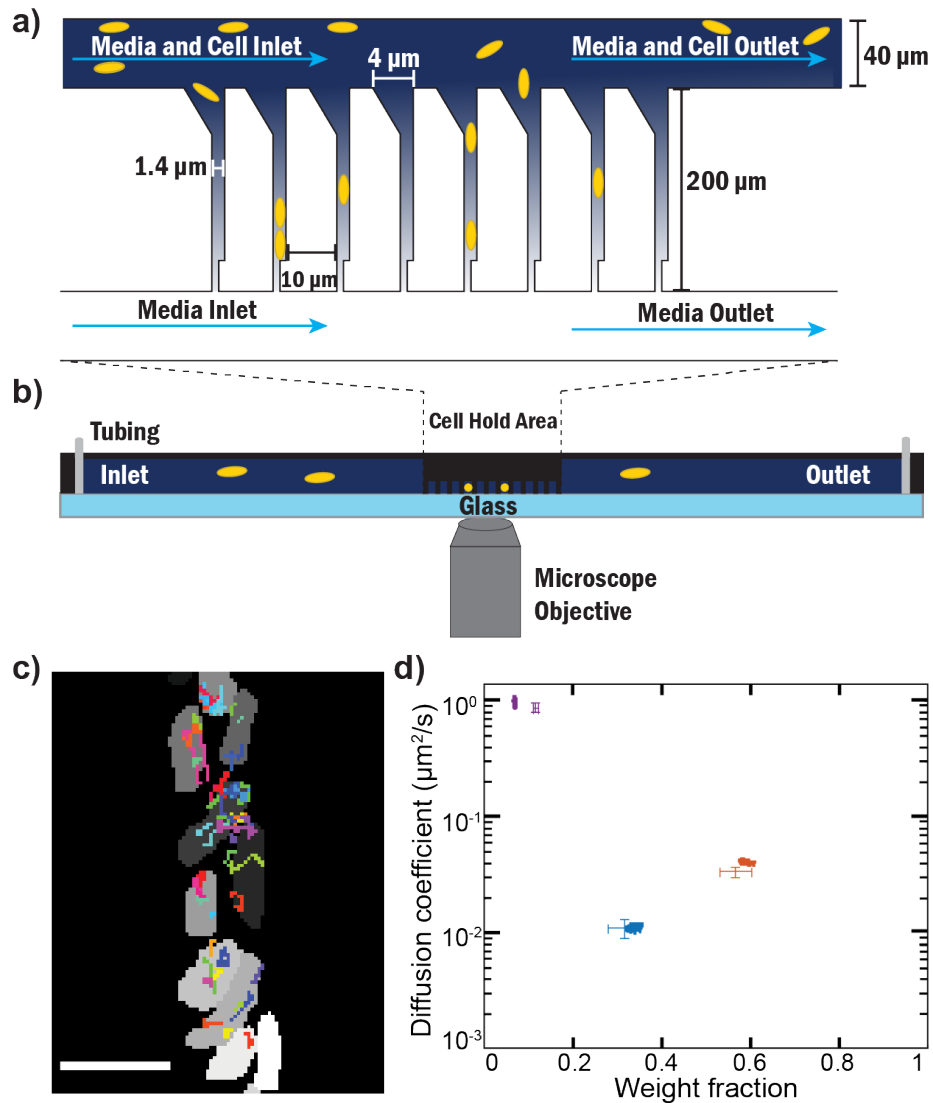
Figure 7.6: Single molecule detection in live *V. cholerae* cells in a microfluidic device. Caption on next page.

Figure 7.6: a) Microfluidic device design schematic (top view). The large top and bottom channels are 40 μm deep, the small channels are 1.4 μm deep. b) Microfluidic device design schematic (side view). The dashed lines between 'a' and 'b' represent where the top view in 'a' corresponds to the side view in 'b'. Measurements in 'a' and 'b' not to scale; dimensions indicated in the figure. c) Representative TcpP-PAmC single-molecule trajectories overlaid on *V. cholerae* cell outlines converted from the phase contrast image; each cell is false colored on a greyscale. The false-colored trajectories show the diversity of motion observed. Scale bar: 2 μm. d) Average single-molecule diffusion coefficients and weight fraction estimates for TcpP-PAmC in live *V. cholerae* cells grown under virulence-inducing conditions and immobilized in the microfluidic device. Single-step analysis identifies three distinct diffusion states (fastest to slowest: purple, orange, and blue). Each point represents the average single-molecule diffusion coefficient vs. weight fraction of TcpP-PAmC molecules in each distinct mobility state at each saved iteration of the Bayesian algorithm after convergence. The data set contains 109,060 steps from 24,580 trajectories. The data for TcpP-PAmC diffusion in living *V. cholerae* cells grown under virulence-inducing conditions and immobilized under an LB agarose pad (traditional sample preparation) are provided for reference (cross-hairs). The data set contains 19,254 steps from 6,643 trajectories.

To verify that the single-molecule dynamics are unaffected by the microfluidic device, we localized and tracked single TcpP-PAmC molecules [37]. We analyzed the heterogeneous motion in these trajectories with the SMAUG algorithm [38]. SMAUG assigns the single-molecule displacements that make up a collection of trajectories into the most probable diffusion states, and it quantifies the weight fraction and average diffusion coefficient of each state using Gibbs sampling in a Bayesian framework. We analyzed the tracking data and found that the TcpP-PAmC molecules in *V. cholerae* in the microfluidic devices (LB medium, pH 6) exhibit three distinct diffusion states: most molecules diffuse slowly or moderately, and a small number diffuse rapidly (blue, orange, and purple clusters, respectively, in Fig. 7.6d). Average diffusion coefficients for each state are listed in Table 7.1. These dynamics are similar to those we previously measured for TcpP-PAmC at pH 6 on agarose pads (Chapter III) [1]. Since the microfluidic device measurements were collected in cells in rich LB media, not minimal M9 media as previously published [1], we imaged cells mounted on an LB agarose pad for comparison and found that the dynamics in the microfluidic channels matched those on the LB agarose pad (Fig. 7.6d). To reduce the background from the surrounding LB media, the imaged area was pre-bleached with
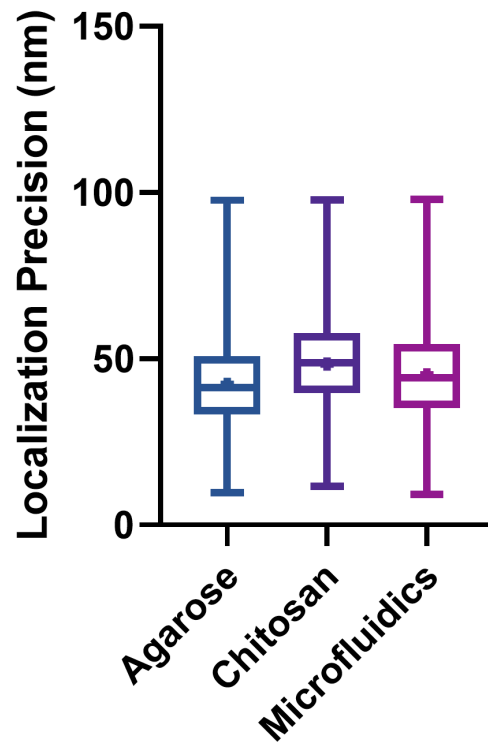
Figure 7.7: Comparing localization precision. Localization precision (95% confidence interval on localization position) for N = 100,000 single molecules each detected in cells immobilized on agarose pads (blue), on chitosan-coated coverslips (purple), or in a microfluidic device (pink). The box indicates the middle 50% of the data set and the middle line indicates the median. The single point represents the mean. The horizontal lines indicate the minimum and maximum of each total data set.

Table 7.1: Average diffusion coefficient and weight fraction for each diffusion state in this section's figures as indicated.

Figure	Condition	State Color	Diffusion Coefficient (μm^2)	Weight Fraction
7.6c	Microfluidics	purple	0.973 ± 0.038	0.07
7.6c	Microfluidics	orange	0.041 ± 0.002	0.59
7.6c	Microfluidics	blue	0.011 ± 0.001	0.34
7.6c	Agarose	purple	0.873 ± 0.039	0.12
7.6c	Agarose	orange	0.034 ± 0.002	0.56
7.6c	Agarose	blue	0.011 ± 0.001	0.32

the 488- and 561-nm lasers prior to photoactivating PAmC molecules for both preparation methods. Imaging cells in LB medium in a microfluidic device required less pre-bleaching time than for the traditional sample preparation (1 min vs. 7 min). Additionally, less background fluorescence remained after the pre-bleaching step for cells in the device relative to cells on agarose, giving us better sensitivity to single molecules in LB on device than on agarose: we detected 10 times more molecules per cell on device than on agarose. We attribute this improvement to the smaller volume of media above the cells, which contributes less out-of-focus fluorescent background.

Once cells were immobilized in the small channels, we attempted to change the surrounding media by injecting minimal media into both inlet channels. However, when the flowing media reaches the cells, they become more mobile, and ultimately over the course of several hours, the cells exit the small channels through the top. Currently, we are unable to implement single-molecule imaging during real-time environmental changes on the microfluidic device described above, though we can achieve single-molecule tracking in live bacteria cells on the microfluidic device. Given the developments, we reason that single-molecule imaging during real-time environmental changes on device is feasible and I describe some potential optimization approaches in the next section.

7.6   Conclusions and Future Work

I achieved single-molecule tracking in living *V. cholerae* bacteria cells immobilized on the microfluidic device and found that the dynamics matched those in similar conditions with traditional sample preparation. Unfortunately, upon restarting the flow, we found that cells became more mobile and ultimately exited the small channels due to pressure from the flow in the small channels. I believe that with more troubleshooting, including experimenting with the rates and patterns of the flow, this preparation could be suitable for undertaking single-molecule measurements during the course of environmental changes on device as originally hypothesized; however, I found that chitosan-coated coverslips provide a simpler solution [2].

I have some troubleshooting ideas for improving device function. First, you could use two separate syringe pumps—one on each inlet—to have two different flow rates, to establish more of a pressure gradient in the small channel. Second, you could return flow to the top channel from both sides and have no flow in the bottom channel to increase the pressure on the top end of the small channel. This change might cause too much pressure in the device and break the PDMS or glass coverslip, so I would test this flow method on a benchtop before attempting on a microscope. Third, you could try changing the shape of the funnel and continue to decrease the channel size. These geometric changes might improve cell flow into the channels while also constricting cell movement. Fourth, PDMS device coatings may improve cell stickiness in the channels; however, this could lead to clogging of the large channels if the coating is too sticky [171, 172]. Fifth, you could combine the chitosan slide coatings with a microfluidic flow channel, which could add to the capability of the chitosan slide coating technology. I have attempted to coat slides with chitosan slide coating solution prior to device bonding, but devices do not bond properly. I was unsuccessful in pumping the chitosan solution into the channels because the solution was too viscous to run through the device, so parameters need to be adjusted. Finally, you could use bacteria strains that are mutated to knock out the flagella. Less mobile cells

should be stationary in the channels. The downside of this solution is that there could be unknown adverse effects on cell function, which might change the biological conclusions without our knowledge. Previous studies have been done with similar cell manipulations to immobilize cells in a microfluidic device during flow [164], but no work has been done to evaluate the effect of flagella on TcpP or the toxin regulation pathway in *V. cholerae*. These ideas are a good starting place for anyone attempting to make a fully functional microfluidic device for bacteria cell immobilization in the future.

CHAPTER VIII

Conclusions

8.1 Introduction

Single-molecule fluorescence (SMF) imaging encompasses a variety of techniques to overcome the diffraction limit of light and can provide insight into biological mechanisms in live cells. However, sample preparation methods limit this ability to steady-state conditions. As I have described throughout this dissertation, chitosan-coated coverslips and microfluidics will enable new experiments to acquire important insight into bacteria function during real-time environment changes often a vital aspect of bacteria survival. In this final chapter, I will review the conclusions from the preceding chapters and present future directions for both new methodologies.

8.2 *Escherichia coli* Live-cell Imaging of Colicin E1

In Chapter II, I discussed the *Escherichia coli* (*E. coli*)-specific bacteriocin, colicin, and the unique properties of Colicin E1 to block a key efflux pump in the *E. coli* outer membrane. I used diffraction-limited single-molecule fluorescence microscopy in live *E. coli* cells to further probe the Colicin E1 mechanism in conjunction with biochemical assays performed by others. I found that ColE1TR-Cy3 forms a single punctum on the surface of *E. coli* cells when the TolC membrane protein is present. I demonstrated that these

puncta are immobile and contain 20 molecules. I also found that ColE1-TR-Cy3 puncta only form on cells that contain the TolC or ButB membrane proteins, confirming the need for both binding sites for Colicin E1 interaction with *E. coli* cells. Taken together with our collaborators' experiments [50], these discoveries helped to determine the structure and mechanism of ColE1 insertion and led to an alternative approach for targeting Outer Membrane Proteins (OMPs): the development of molecular plugs that block OMPs pores.

There are many directions to work on to better understand the Colicin E1 protein and its unique mechanism from other colicins. From a microscopy perspective, it would be interesting to monitor the rate and reversibility of binding using the new chitosan slide method I developed (Chapter IV). Using the chitosan slides, you could immobilize *E. coli* cells, begin to image, and then add the ColE1-Cy3 protein to the sample on the microscope. This would allow you to monitor for puncta formation in real time. You could also alter the environment conditions of cells already containing bound molecules and monitor for punctum deformation based on environment conditions, again using the chitosan slide method. Finally, single-molecule tracking was not rigorously performed on ColE1-Cy3 because initial tracking indicated an immobile group. However, if we could tag the TolC or BtuB protein without disrupting function, it could be interesting to track those proteins as a baseline to then track those proteins after ColE1-Cy3 addition to relate changes in dynamics to protein binding. In addition to better understandning Colicin E1 binding and unbinding, these experiments could open up new questions and would require extensive collaboration with the Slusky lab for complementary biochemical studies.

8.3 Independent Promoter Recognition by TcpP Precedes Cooperative Promoter Activation by TcpP and ToxR

In Chapter III, I introduced *Vibrio cholerae* (*V. cholerae*) and its toxin regulation pathway including the membrane-bound transcription factor TcpP. I implemented SMF imag-

ing to track TcpP-PAmCherry (TcpP-PAmC) in live *V. cholerae* cells grown in virulence-inducing conditions: pH 6 and 30 °C. I found that TcpP-PAmC has three biophysical diffusion states that we hypothesize correspond to three biochemical functions: free, searching, and bound. My biophysical measurements of mutated cells support the hypothesis that the slow diffusion state is occupied by TcpP-PAmC molecules interacting specifically with DNA at the *toxT* promoter (*toxTpro*). Additionally, I observed that ToxR is not required for TcpP binding since only a small reduction in the slow group occurred in *tcpP-PAmC* Δ*toxRS* cells. Finally, we found that under certain conditions, ToxR can decrease *toxT* expression by quickening TcpP-PAmC single-molecule dynamics. Taken together, these data support the modified promoter alteration model [88] and show that ToxR does not directly recruit TcpP to the *toxTpro*.

Two major observations from this study remain unclear: what precisely the intermediate state corresponds to and how overexpressed ToxR sequesters TcpP-PAmC away from the bound state. The intermediate states are certainly important, as TcpP molecules transition to the *toxTpro*-bound state only from them, but the difference in diffusion coefficient is too large to be explained by dimerization or ToxR interaction alone. One possibility is that TcpP-PAmC molecules undergo fast diffusion in less protein-dense areas of the cytoplasmic membrane relative to TcpP-PAmC molecules undergoing intermediate diffusion. It has been hypothesized that membrane-localized proteins have different preferences for lipid-ordered and lipid-disordered membrane domains leading to this difference in intermediate diffusion populations [131]. This theory could be investigated by analyzing TcpP-PAmC dynamics in cells with two chemical treatments: increasing the amount of lipid-ordered regions and increasing the amount of lipid-disordered regions. Alternatively, the diffusion coefficients of TcpP-PAmC molecules in the intermediate state may be undergoing nonspecific interactions with DNA whereas the slowest TcpP-PAmC molecules are specifically bound at *toxTpro*. This hypothesis is our leading theory and could be tested by studying TcpP-PAmC dynamics in cells with specific residue changes to the *toxTpro*

rather than a complete deletion. However, this hypothesis is harder to prove.

Secondly, it remains unclear how ToxR sequesters TcpP-PAmC molecules from the slow diffusion state. However, we hypothesize that ToxR promotes TcpP molecules to transition away from the slow diffusion state to prevent unwanted *toxT* expression. The sequestering mechanism is discussed more in Chapter IV

8.4 Development of Chitosan-coated Coverslips for Single-molecule Fluorescence Imaging in Live Bacteria Cells during Real-time Environment Perturbations

In Chapter IV, I described the limitation of SMF imaging sample preparation to not be amenable during real-time environment changes, and my first solution to this limitation, chitosan-coated coverslips. I expanded on previous work [45] and showed that chitosan-coated coverslips can be used as substrates for experiments tracking single molecules in live *V. cholerae* cells. I observed that the TcpP-PAmC dynamics are not changed on chitosan-coated coverslips, relative to their dynamics in cells mounted on agarose pads. Additionally, I demonstrated the ability to monitor real-time changes in single-molecule dynamics upon changes to cell environment by observing the transition in dynamics of TcpP-PAmC in cells expressing an isopropyl-β-D-thiogalactopyranoside (IPTG)-inducible copy of *toxR*, which encodes the TcpP-binding partner and coactivator of *toxT*. I observed these dynamics changes with a 5-min temporal resolution, which is not possible with traditional sample preparation technologies.

The chitosan-coated coverslip is robust to many environmental changes including pH and increased oxidative conditions and can immobilize a variety of bacteria. This cell immobilization methodology can be expanded to study other bacteria and impact our understanding of their biological functions in changing environments. In Chapter V, I applied this method to studying *V. cholerae* toxin regulation. In Chapter VI, I applied this method

to studying *E. coli* short-term stress response. There are many other examples of bacterial adaptation to changing environments, and this method can be applied to help elucidate more about them. Other applications of this method are already having an impact in the Biteen lab. Thorough studies of cell function on chitosan coverslips need to be performed. This should include exploring if there are differences between the protein makeup of cells grown on agarose and grown on chitosan slides. Additionally, *V. cholerae* has been shown to use chitin as a food source, so it should be explored if this is possible for cells on chitosan slides and if this affects cell function.

It was always a goal of mine to use the chitosan-coated coverslip method to study anaerobic gut microbiome bacteria. The challenge of course is finding a way to make the sample preparation, designed to be unencapsulated, anaerobic. I played around with designs that used a stronger ring epoxied to a glass coverslip with two small tubing-sized holes drilled in the glass coverslip in the center of the ring. The microfluidics tubing could be secured in the holes and sealed using epoxy. This cover could be secured to a new chitosan-coated coverslip and sealed in an anaerobic chamber with the desired cell sample immobilized. Syringes containing appropriate media would be attached to the tubing ends at which point the whole sample should be sealed off from the external environment. This is where I would start with an anaerobic sample design. The first test would have to be ensuring the sample remains oxygen free once removed from the chamber.

8.5   Regulation of Toxin Production in *Vibrio cholerae* in Response to Real-time Changes in Environment pH

In Chapter V, I described the implementation of the previously discussed chitosan-coated coverslip method to study the effects of changes in pH on TcpP-PAmC dynamics in live *V. cholerae* cells. I found that the slowest diffusion state, which is only found at non virulence-inducing conditions, pH 8, disappears between 30 and 55 min after exchang-

ing the cell media with pH 6 media, which establishes virulence-inducing conditions. I hypothesized that this slowest state corresponds to sequestering of TcpP away from its binding sight. The timescale of the disappearance of this slowest state, combined with the higher likelihood of molecules in this state localizing at the poles, confirms my hypothesis regarding the biophysical role: TcpP is sequestered from the *toxTpro* at pH 8 and gradually allowed to bind upon environmental signaling (pH 6). Prior to this work, there was no evidence that TcpP molecules are sequestered from the *toxTpro*. The work presented here has revealed a novel mechanism of post-translational regulation of TcpP that motivates further study. This result highlights the value of the chitosan slide coating technology to better understand the mechanism by which TcpP regulates *V. cholerae* toxin production as this conclusion can only be drawn based on the ability to monitor these single-molecule dynamics during changes in real time.

Further work is needed to better understand this sequestering mechanism. This should include complementary biochemical assays, exploring the role of ToxR during real-time changes in pH, and studies altering the components of the membrane as described in Section 8.3. Additional studies of interest with *V. cholerae* include exploring the dynamics of TcpP in response to the addition of bile salts or gut bacteria. *V. cholerae* proliferation occurs in the human gut system, so it can be hypothesized that a variety of conditions differentiating the gut from the native *V. cholerae* environment trigger higher virulence production and could alter TcpP dynamics. The literature contains mixed conclusions regarding bile salt effect on TcpP binding [24,30,32,126] and an in vivo study could resolve these discrepancies. Finally, the ultimate goal of this project was always to look at *V. cholerae* quorum sensing in real time. *V. cholerae* like many bacteria use small-molecule autoinducers to communicate cell to cell. This quorum sensing is vital during environment stress conditions and to begin bacteria biofilm growth. This method can be used to study TcpP and ToxR during high and low quorum-sensing conditions by adding various concentrations of autoinducers.

8.6 Regulation of a DNA-binding Protein in *Escherichia coli* in Response to Real-time Oxidative Damage.

In Chapter VI, I described the implementation of the chitosan slide coating method to study the effects of oxidative damage on Dps-PAmCherry (Dps-PAmC) dynamics in live *E. coli* cells. I confirmed previous results showing DNA-binding Protein from Starved cells (Dps) is upregulated during oxidative damage by imaging mCherry on the *dps* promoter (*dpspro*) in live *E. coli* cells immobilized on chitosan coverslips. Although, I found that this upregulation is maxed out at 20 μM hydrogen peroxide (H_2O_2) potentially due to cell deterioration. Additionally, I showed that Dps does not compact the cell nucleoid in response to oxidative damage unlike during starvation. Both results agree with in vitro assays in the literature [8, 158]. Tracking Dps-PAmC dynamics during real-time addition of 20 μM H_2O_2 revealed that Dps responds to oxidative damage almost immediately (less than 1 minute) and changes in dynamics oscillate over the 120-minute period. By comparing the changes in dynamics of Dps-PAmC after additions of H_2O_2 to after starvation, I determined that Dps response to oxidative damage relies on a chemical reduction of H_2O_2 rather than physically binding to DNA.

Further work is needed to verify the functionality of Dps-PAmC and the biophysical function of the intermediate and slow state (navy and green, Fig. 6.5a). Additionally, it would be interesting to explore the oscillatory pattern of the weight fraction of the fast state (pink) during real-time additions of H_2O_2. Looking at how long after adding H_2O_2 the fast group changes weight fraction would be one way to research this. If Dps is eliminating H_2O_2 in the cells through a chemical process we would expect less H_2O_2 in the environment over time and a return to dynamics seen at 0 min in Fig. 6.5a. Measuring how Dps-PAmC dynamics change after reapplication of H_2O_2 could also give insight to the chemical response of Dps. All of these results can be measured with the chitosan-coated coverslip method. Finally, there are many other proteins involved in *E. coli* stress

management including H-NS that would be of interest to explore using this new methodology and compare to changes in Dps dynamics.

8.7   Development of a Microfluidic Device for Single-molecule Fluorescence Imaging in Live Bacteria Cells

In Chapter VII, I described my second solution to the sample preparation limitation for fluorescence imaging in live bacteria, a microfluidic device. I designed, fabricated, and tested a microfluidic device to immobilize live bacteria cells and be compatible with SMF imaging. I found that immobilizing and imaging cells in the device did not alter cell function by matching the dynamics for TcpP-PAmC in live *V. cholerae* cells to those on traditional sample preparation. Unfortunately, upon restarting the flow, I found that cells became more mobile and ultimately exited the small channels due to pressure from the flow in the small channels. I believe that with more troubleshooting, including experimenting with the rates and patterns of the flow, this preparation could be suitable for undertaking single-molecule measurements during the course of environmental changes on device as originally hypothesized.

I proposed many directions for troubleshooting the current device to function as proposed in Chapter VII. These include altering the solution flow pattern, changing the funnel shape, adding a device coating, combining the device with the chitosan-coated coverslips, and using mutated bacteria. Here, I would like to discuss future directions for experiments on a functioning device. As mentioned in Section 8.4, there is a variety of bacteria that could be studied using the new sample preparation. The advantage of a microfluidic device over coated coverslips is the ability to make more regulated changes to the cell environment through controlled flow times and to gradually ramp up concentration. It would be interesting to understand how the dynamics of TcpP-PAmC change in response to gradual changes in pH. I found that pH 6 triggers a virulence response, but it is not

145

known if there is a gradual increase in response from pH 8 to 7 to 6. This experiment would be possible with the microfluidic device. Additionally, flowing in a new cell population would be easier on the microfluidic device. This would allow for studies with the gut microbiome bacteria and *V. cholerae* to see how TcpP-PAmC responds to signaling from non-*V. cholerae* cells. A completely operational microfluidic device opens the door for many additional experiments.

As discussed in Section 8.4, an ultimate goal of these novel sample preparation methods was to work with anaerobic bacteria. Making a microfluidic device anaerobic is potentially much easier than the chitosan-coated coverslip method. Polydimethylsiloxane (PDMS) used for this device is a breathable material. This was a conscious choice due to the need for oxygen in the channels to maintain the life and normal function of aerobic *V. cholerae*. However, a non-breathable plastic can be chosen to construct the microfluidic device and already in place tubing can be sealed off. This simple change would make the implementation with anaerobic bacteria much simpler than the slide coatings.

8.8   Overarching Conclusions

In this dissertation, I have added to the toolbox available for studying live bacteria cells. I have extended the sample preparation methods for SMF imaging and tracking experiments to enable the use of this technique during real-time environment changes. I demonstrated the use of both sample preparation methods, chitosan-coated coverslips and a microfluidic device, in live *V. cholerae* cells by tracking TcpP-PAmC and matching dynamics to those found in cells on traditional sample preparation. Using the chitosan-coated coverslips method, I proposed a new sequestering mechanism for toxin regulation in *V. cholerae* by tracking TcpP-PAmC dynamics during real-time changes in pH with 5-minute temporal resolution. Additionally, I determine Dps uses a chemical reduction mechanism during oxidative damage in *E. coli* by tracking Dps-PAmC dynamics during real-time additions of H_2O_2. I have shown that this chitosan-coated coverslip method de-

scribed in this dissertation is robust to many environment changes and can impact a diversity of bacteria studies. In a world with growing antibiotic resistance and changing climates, understanding bacteria during vital environmental changes can facilitate development of new treatments and vaccines, and the methods presented in this dissertation enable these studies.

BIBLIOGRAPHY

BIBLIOGRAPHY

[1] A. L. Calkins, *et al.*, "Independent Promoter Recognition by TcpP Precedes Cooperative Promoter Activation by TcpP and ToxR", *mBio* **12**, e02213 (2021). DOI: 10.1128/mBio.02213-21.

[2] A. L. Calkins, L. M. Demey, B. M. Rosenthal, V. J. DiRita, J. S. Biteen, "Achieving Single-Molecule Tracking of Subcellular Regulation in Bacteria during Real-Time Environmental Perturbations", *Analytical Chemistry* **95**, 774 (2023). DOI: 10.1021/acs.analchem.2c02899.

[3] M. Fernández-Suárez, A. Y. Ting, "Fluorescent probes for super-resolution imaging in living cells", *Nature Reviews Molecular Cell Biology* **9**, 929 (2008). DOI: 10.1038/nrm2531.

[4] H. H. Tuson, J. S. Biteen, "Unveiling the Inner Workings of Live Bacteria Using Super-Resolution Microscopy", *Analytical Chemistry* **87**, 42 (2015). DOI: 10.1021/ac5041346.

[5] C. S. Pereira, J. A. Thompson, K. B. Xavier, "AI-2-mediated signalling in bacteria", *FEMS Microbiology Reviews* **37**, 156 (2013). DOI: 10.1111/j.1574-6976.2012.00345.x.

[6] J. Zhu, *et al.*, "Quorum-sensing regulators control virulence gene expression in Vibrio cholerae", *Proceedings of the National Academy of Sciences* **99**, 3129 (2002). DOI: 10.1073/pnas.052694299.

[7] E. S. Krukonis, V. J. DiRita, "DNA binding and ToxR responsiveness by the wing domain of TcpP, an activator of virulence gene expression in Vibrio cholerae", *Molecular Cell* **12**, 157 (2003). DOI: 10.1016/s1097-2765(03)00222-3.

[8] V. O. Karas, I. Westerlaken, A. S. Meyer, "The DNA-Binding Protein from Starved Cells (Dps) Utilizes Dual Functions To Defend Cells against Multiple Stresses", *Journal of Bacteriology* **197**, 3206 (2015). DOI: 10.1128/JB.00475-15.

[9] F. Santos-Beneit, "The Pho regulon: a huge regulatory network in bacteria", *Frontiers in Microbiology* **6**, 402 (2015). DOI: 10.3389/fmicb.2015.00402.

[10] H. H. Tuson, M. H. Foley, N. M. Koropatkin, J. S. Biteen, "The Starch Utilization System Assembles around Stationary Starch-Binding Proteins", *Biophysical Journal* **115**, 242 (2018). DOI: 10.1016/j.bpj.2017.12.015.

[11] V. J. DiRita, C. Parsot, G. Jander, J. J. Mekalanos, "Regulatory cascade controls virulence in Vibrio cholerae", *Proceedings of the National Academy of Sciences* **88**, 5403 (1991). DOI: 10.1073/pnas.88.12.5403.

[12] J. N. Zuckerman, L. Rombo, A. Fisch, "The true burden and risk of cholera: implications for prevention and control", *The Lancet Infectious Diseases* **7**, 521 (2007). DOI: 10.1016/S1473-3099(07)70138-X.

[13] C. Baker-Austin, *et al.*, "Vibrio spp. infections", *Nature Reviews Disease Primers* **4**, 1 (2018). DOI: 10.1038/s41572-018-0005-8.

[14] T. Jelinek, H. Kollaritsch, "Vaccination with Dukoral® against travelers' diarrhea (ETEC) and cholera", *Expert Review of Vaccines* **7**, 561 (2008). DOI: 10.1586/14760584.7.5.561.

[15] A. Saha, *et al.*, "Safety and immunogenicity study of a killed bivalent (O1 and O139) whole-cell oral cholera vaccine Shanchol, in Bangladeshi adults and children as young as 1 year of age", *Vaccine* **29**, 8285 (2011). DOI: 10.1016/j.vaccine.2011.08.108.

[16] Cabrera, A., Lepange, J.E., Sullivan, K.M., Seed, S.M., "Vaxchora: A Single-Dose Oral Cholera Vaccine", *Annals of Pharmacotherapy* **51**, 584 (2017).

[17] H. B. Kim, *et al.*, "Transferable quinolone resistance in Vibrio cholerae", *Antimicrobial Agents and Chemotherapy* **54**, 799 (2010). DOI: 10.1128/AAC.01045-09.

[18] B. V. S. Krishna, A. B. Patil, M. R. Chandrasekhar, "Fluoroquinolone-resistant Vibrio cholerae isolated during a cholera outbreak in India", *Transactions of the Royal Society of Tropical Medicine and Hygiene* **100**, 224 (2006). DOI: 10.1016/j.trstmh.2005.07.007.

[19] R. I. Glass, *et al.*, "Plasmid-Borne Multiple Drug Resistance in Vibrio cholerae Serogroup O1, Biotype El Tor: Evidence for a Point-Source Outbreak in Bangladesh", *The Journal of Infectious Diseases* **147**, 204 (1983). DOI: 10.1093/infdis/147.2.204.

[20] B. Pang, *et al.*, "The Transmission and Antibiotic Resistance Variation in a Multiple Drug Resistance Clade of Vibrio cholerae Circulating in Multiple Countries in Asia", *PLOS ONE* **11**, e0149742 (2016). DOI: 10.1371/journal.pone.0149742.

[21] B. Ramakrishna, *et al.*, "Amylase-Resistant Starch plus Oral Rehydration Solution for Cholera", *New England Journal of Medicine* **342**, 308 (2000). DOI: 10.1056/NEJM200002033420502.

[22] F. R. Chowdhury, Z. Nur, N. Hassan, L. von Seidlein, S. Dunachie, "Pandemics, pathogenicity and changing molecular epidemiology of cholera in the era of global warming", *Annals of Clinical Microbiology and Antimicrobials* **16**, 10 (2017). DOI: 10.1186/s12941-017-0185-1.

[23] E. S. Krukonis, R. R. Yu, V. J. Dirita, "The Vibrio cholerae ToxR/TcpP/ToxT virulence cascade: distinct roles for two membrane-localized transcriptional activators on a single promoter", *Molecular Microbiology* **38**, 67 (2000). DOI: 10.1046/j.1365-2958.2000.02111.x.

[24] E. S. Krukonis, V. J. DiRita, "From motility to virulence: Sensing and responding to environmental signals in Vibrio cholerae", *Current Opinion in Microbiology* **6**, 186 (2003). DOI: 10.1016/s1369-5274(03)00032-8.

[25] J. S. Matson, J. H. Withey, V. J. DiRita, "Regulatory Networks Controlling Vibrio cholerae Virulence Gene Expression", *Infection and Immunity* **75**, 5542 (2007). DOI: 10.1128/IAI.01094-07.

[26] J. A. Crawford, E. S. Krukonis, V. J. DiRita, "Membrane localization of the ToxR winged-helix domain is required for TcpP-mediated virulence gene activation in Vibrio cholerae", *Molecular Microbiology* **47**, 1459 (2003).

[27] B. L. Haas, J. S. Matson, V. J. DiRita, J. S. Biteen, "Single-molecule tracking in live Vibrio cholerae reveals that ToxR recruits the membrane-bound virulence regulator TcpP to the toxT promoter", *Molecular microbiology* **96**, 4 (2015). DOI: 10.1111/mmi.12834.

[28] D. T. Hung, E. A. Shakhnovich, E. Pierson, J. J. Mekalanos, "Small-Molecule Inhibitor of Vibrio cholerae Virulence and Intestinal Colonization", *Science* **310**, 670 (2005). DOI: 10.1126/science.1116739.

[29] V. L. Miller, J. J. Mekalanos, "A novel suicide vector and its use in construction of insertion mutations: osmoregulation of outer membrane proteins and virulence determinants in Vibrio cholerae requires toxR", *Journal of Bacteriology* **170**, 2575 (1988). DOI: 10.1128/jb.170.6.2575-2583.1988.

[30] S. Gupta, R. Chowdhury, "Bile affects production of virulence factors and motility of Vibrio cholerae", *Infection and Immunity* **65**, 1131 (1997). DOI: 10.1128/iai.65.3.1131-1134.1997.

[31] K. Skorupski, R. K. Taylor, "Control of the ToxR virulence regulon in Vibrio cholerae by environmental stimuli", *Molecular Microbiology* **25**, 1003 (1997). DOI: 10.1046/j.1365-2958.1997.5481909.x.

[32] D. T. Hung, J. J. Mekalanos, "Bile acids induce cholera toxin expression in Vibrio cholerae in a ToxT-independent manner", *Proceedings of the National Academy of Sciences* **102**, 3028 (2005). DOI: 10.1073/pnas.0409559102.

[33] J. R. Lakowicz, ed., *Principles of Fluorescence Spectroscopy* (Springer US, Boston, MA, 2006).

[34] A. M. Sydor, K. J. Czymmek, E. M. Puchner, V. Mennella, "Super-Resolution Microscopy: From Single Molecules to Supramolecular Assemblies", *Trends in Cell Biology* **25**, 730 (2015). DOI: 10.1016/j.tcb.2015.10.004.

[35] E. Betzig, *et al.*, "Imaging Intracellular Fluorescent Proteins at Nanometer Resolution", *Science* **313**, 1642 (2006). DOI: 10.1126/science.1127344.

[36] O. M. Subach, *et al.*, "Conversion of Red Fluorescent Protein into a Bright Blue Probe", *Chemistry & Biology* **15**, 1116 (2008). DOI: 10.1016/j.chembiol.2008.08.006.

[37] B. P. Isaacoff, Y. Li, S. A. Lee, J. S. Biteen, "SMALL-LABS: Measuring Single-Molecule Intensity and Position in Obscuring Backgrounds", *Biophysical Journal* **116**, 975 (2019). DOI: 10.1016/j.bpj.2019.02.006.

[38] J. D. Karslake, *et al.*, "SMAUG: Analyzing single-molecule tracks with nonparametric Bayesian statistics", *Methods* **193**, 16 (2021). DOI: 10.1016/j.ymeth.2020.03.008.

[39] A. L. Bottomley, L. Turnbull, C. B. Whitchurch, E. J. Harry, "Immobilization Techniques of Bacteria for Live Super-resolution Imaging Using Structured Illumination Microscopy", *Bacterial Pathogenesis* **1535**, 197 (2017). DOI: 10.1007/978-1-4939-6673-8_12.

[40] G. M. Whitesides, "The origins and the future of microfluidics", *Nature* **442**, 368 (2006). DOI: 10.1038/nature05058.

[41] W. E. Moerner, "New directions in single-molecule imaging and analysis", *Proceedings of the National Academy of Sciences* **104**, 12596 (2007). DOI: 10.1073/pnas.0610081104.

[42] M. J. Lawson, *et al.*, "*In situ* genotyping of a pooled strain library after characterizing complex phenotypes", *Molecular Systems Biology* **13**, 947 (2017). DOI: 10.15252/msb.20177951.

[43] O. Baltekin, A. Boucharin, E. Tano, D. I. Andersson, J. Elf, "Antibiotic susceptibility testing in less than 30 min using direct single-cell imaging", *Proceedings of the National Academy of Sciences* **114**, 9170 (2017). DOI: 10.1073/pnas.1708558114.

[44] R. de Leeuw, *et al.*, *The Bacterial Nucleoid*, O. Espéli, ed. (Springer New York, New York, NY, 2017), vol. 1624, pp. 237–252.

[45] J. Tréguier, *et al.*, "Chitosan Films for Microfluidic Studies of Single Bacteria and Perspectives for Antibiotic Susceptibility Testing", *mBio* **10**, e01375 (2019). DOI: 10.1128/mBio.01375-19.

[46] D. Raafat, H.-G. Sahl, "Chitosan and its antimicrobial potential – a critical literature survey", *Microbial Biotechnology* **2**, 186 (2009). DOI: 10.1111/j.1751-7915.2008.00080.x.

[47] Y.-K. Wang, *et al.*, "Comparison of Escherichia coli surface attachment methods for single-cell microscopy", *Scientific Reports* **9**, 19418 (2019). DOI: 10.1038/s41598-019-55798-0.

[48] M. S. Liberio, M. C. Sadowski, C. Soekmadji, R. A. Davis, C. C. Nelson, "Differential Effects of Tissue Culture Coating Substrates on Prostate Cancer Cell Adherence, Morphology and Behavior", *PLOS ONE* **9**, e112122 (2014). DOI: 10.1371/journal.pone.0112122.

[49] K. Colville, N. Tompkins, A. D. Rutenberg, M. H. Jericho, "Effects of Poly(l-lysine) Substrates on Attached Escherichia coli Bacteria", *Langmuir* **26**, 2639 (2010). DOI: 10.1021/la902826n.

[50] S. J. Budiardjo, *et al.*, "Colicin E1 opens its hinge to plug TolC", *eLife* **11**, e73297 (2022). DOI: 10.7554/eLife.73297.

[51] C. Alexander, E. T. Rietschel, "Invited review: Bacterial lipopolysaccharides and innate immunity", *Journal of Endotoxin Research* **7**, 167 (2001). DOI: 10.1177/09680519010070030101.

[52] T. C. Freeman, Jr, W. C. Wimley, "TMBB-DB: a transmembrane β-barrel proteome database", *Bioinformatics* **28**, 2425 (2012). DOI: 10.1093/bioinformatics/bts478.

[53] R. N. de Zwaig, S. E. Luria, "Genetics and Physiology of Colicin-tolerant Mutants of Escherichia coli", *Journal of Bacteriology* **94**, 1112 (1967). DOI: 10.1128/jb.94.4.1112-1123.1967.

[54] W. A. Cramer, O. Sharma, S. Zakharov, "On mechanisms of colicin import: the outer membrane quandary", *Biochemical Journal* **475**, 3903 (2018). DOI: 10.1042/BCJ20180477.

[55] E. Cascales, *et al.*, "Colicin Biology", *Microbiology and Molecular Biology Reviews* **71**, 158 (2007). DOI: 10.1128/MMBR.00036-06.

[56] H. Benedetti, *et al.*, "Individual domains of colicins confer specificity in colicin uptake, in pore-properties and in immunity requirement", *Journal of Molecular Biology* **217**, 429 (1991). DOI: 10.1016/0022-2836(91)90747-T.

[57] H. Benedetti, *et al.*, "Comparison of the Uptake Systems for the Entry of Various BtuB Group Colicins into Escherichia coli", *Microbiology* **135**, 3413 (1989). DOI: 10.1099/00221287-135-12-3413.

[58] C. A. Plate, S. E. Luria, "Stages in Colicin K Action, as Revealed by the Action of Trypsin", *Proceedings of the National Academy of Sciences* **69**, 2030 (1972). DOI: 10.1073/pnas.69.8.2030.

[59] J. Dankert, S. M. Hammond, W. A. Cramer, "Reversal by trypsin of the inhibition of active transport by colicin E1", *Journal of Bacteriology* **143**, 594 (1980). DOI: 10.1128/jb.143.2.594-602.1980.

[60] J. R. Dankert, Y. Uratani, C. Grabau, W. A. Cramer, M. Hermodson, "On a domain structure of colicin E1. A COOH-terminal peptide fragment active in membrane depolarization", *The Journal of Biological Chemistry* **257**, 3857 (1982).

[61] H. Bénédetti, R. Lloubès, C. Lazdunski, L. Letellier, "Colicin A unfolds during its translocation in Escherichia coli cells and spans the whole cell envelope when its pore has formed", *The EMBO journal* **11**, 441 (1992). DOI: 10.1002/j.1460-2075.1992.tb05073.x.

[62] K. M. Storek, *et al.*, "Monoclonal antibody targeting the β-barrel assembly machine of Escherichia coli is bactericidal", *Proceedings of the National Academy of Sciences* **115**, 3692 (2018). DOI: 10.1073/pnas.1800043115.

[63] H. Kaur, *et al.*, "The antibiotic darobactin mimics a β-strand to inhibit outer membrane insertase", *Nature* **593**, 125 (2021). DOI: 10.1038/s41586-021-03455-w.

[64] N. Al-Husini, *et al.*, "BR-Bodies Provide Selectively Permeable Condensates that Stimulate mRNA Decay and Prevent Release of Decay Intermediates", *Molecular Cell* **78**, 670 (2020). DOI: 10.1016/j.molcel.2020.04.001.

[65] F. W. Studier, P. Daegelen, R. E. Lenski, S. Maslov, J. F. Kim, "Understanding the Differences between Genome Sequences of Escherichia coli B Strains REL606 and BL21(DE3) and Comparison of the E. coli B and K-12 Genomes", *Journal of Molecular Biology* **394**, 653 (2009). DOI: 10.1016/j.jmb.2009.09.021.

[66] S. Bakshi, A. Siryaporn, M. Goulian, J. C. Weisshaar, "Superresolution imaging of ribosomes and RNA polymerase in live Escherichia coli cells", *Molecular Microbiology* **85**, 21 (2012). DOI: 10.1111/j.1365-2958.2012.08081.x.

[67] M. Chavent, *et al.*, "How nanoscale protein interactions determine the mesoscale dynamic organisation of bacterial outer membrane proteins", *Nature Communications* **9**, 2846 (2018). DOI: 10.1038/s41467-018-05255-9.

[68] P. Rassam, *et al.*, "Supramolecular assemblies underpin turnover of outer membrane proteins in bacteria", *Nature* **523**, 333 (2015). DOI: 10.1038/nature14461.

[69] M.-L. R. Francis, *et al.*, "Porin threading drives receptor disengagement and establishes active colicin transport through Escherichia coli OmpF", *The EMBO journal* **40**, e108610 (2021). DOI: 10.15252/embj.2021108610.

[70] P. White, *et al.*, "Exploitation of an iron transporter for bacterial protein antibiotic import", *Proceedings of the National Academy of Sciences* **114**, 12051 (2017). DOI: 10.1073/pnas.1713741114.

[71] C. Kleanthous, P. Rassam, C. G. Baumann, "Protein–protein interactions and the spatiotemporal dynamics of bacterial outer membrane proteins", *Current Opinion in Structural Biology* **35**, 109 (2015). DOI: 10.1016/j.sbi.2015.10.007.

[72] H. Pilsl, V. Braun, "Novel colicin 10: assignment of four domains to TonB-and TolC dependent uptake via the Tsx receptor and to pore formation", *Molecular Microbiology* **16**, 57 (1995). DOI: 10.1111/j.1365-2958.1995.tb02391.x.

[73] S. R. Loftus, *et al.*, "Competitive recruitment of the periplasmic translocation portal TolB by a natively disordered domain of colicin E9", *Proceedings of the National Academy of Sciences* **103**, 12353 (2006). DOI: 10.1073/pnas.0603433103.

[74] C. G. Schneider, C. N. Penfold, G. R. Moore, C. Kleanthous, R. James, "Identification of residues in the putative TolA box which are essential for the toxicity of the endonuclease toxin colicin E9", *Microbiology* **143**, 2931 (1997). DOI: 10.1099/00221287-143-9-2931.

[75] V. Escuyer, M. Mock, "DNA sequence analysis of three missense mutations affecting colicin E3 bactericidal activity", *Molecular Microbiology* **1**, 82 (1987). DOI: 10.1111/j.1365-2958.1987.tb00530.x.

[76] M. J. Angelichio, J. Spector, M. K. Waldor, A. Camilli, "Vibrio cholerae intestinal population dynamics in the suckling mouse model of infection", *Infection and Immunity* **67**, 3733 (1999). DOI: 10.1128/IAI.67.8.3733-3739.1999.

[77] Y. A. Millet, *et al.*, "Insights into Vibrio cholerae Intestinal Colonization from Monitoring Fluorescently Labeled Bacteria", *PLOS Pathogens* **10**, e1004405 (2014). DOI: 10.1371/journal.ppat.1004405.

[78] R. K. Taylor, V. L. Miller, D. B. Furlong, J. J. Mekalanos, "Use of phoA gene fusions to identify a pilus colonization factor coordinately regulated with cholera toxin", *Proceedings of the National Academy of Sciences* **84**, 2833 (1987). DOI: 10.1073/pnas.84.9.2833.

[79] E. J. Nelson, J. B. Harris, J. G. Morris, S. B. Calderwood, A. Camilli, "Cholera transmission: the host, pathogen and bacteriophage dynamic", *Nature Reviews. Microbiology* **7**, 693 (2009). DOI: 10.1038/nrmicro2204.

[80] A. Camilli, D. T. Beattie, J. J. Mekalanos, "Use of genetic recombination as a reporter of gene expression", *Proceedings of the National Academy of Sciences* **91**, 2634 (1994). DOI: 10.1073/pnas.91.7.2634.

[81] A. T. Nielsen, *et al.*, "A Bistable Switch and Anatomical Site Control Vibrio cholerae Virulence Gene Expression in the Intestine", *PLOS Pathogens* **6**, e1001102 (2010). DOI: 10.1371/journal.ppat.1001102.

[82] D. E. Higgins, V. J. DiRita, "Transcriptional control of toxT, a regulatory gene in the ToxR regulon of Vibrio cholerae", *Molecular Microbiology* **14**, 17 (1994). DOI: 10.1111/j.1365-2958.1994.tb01263.x.

[83] D. E. Higgins, E. Nazareno, V. J. DiRita, "The virulence gene activator ToxT from Vibrio cholerae is a member of the AraC family of transcriptional activators", *Journal of Bacteriology* **174**, 6974 (1992). DOI: 10.1128/jb.174.21.6974-6980.1992.

[84] V. L. Miller, R. K. Taylor, J. J. Mekalanos, "Cholera toxin transcriptional activator ToxR is a transmembrane DNA binding protein", *Cell* **48**, 271 (1987). DOI: 10.1016/0092-8674(87)90430-2.

[85] T. J. Goss, C. P. Seaborn, M. D. Gray, E. S. Krukonis, "Identification of the TcpP-Binding Site in the toxT Promoter of Vibrio cholerae and the Role of ToxR in TcpP-Mediated Activation", *Infection and Immunity* **78**, 4122 (2010).   DOI: 10.1128/IAI.00566-10.

[86] P. A. Carroll, K. T. Tashima, M. B. Rogers, V. J. DiRita, S. B. Calderwood, "Phase variation in tcpH modulates expression of the ToxR regulon in Vibrio cholerae", *Molecular Microbiology* **25**, 1099 (1997). DOI: 10.1046/j.1365-2958.1997.5371901.x.

[87] C. C. Häse, J. J. Mekalanos, "TcpP protein is a positive regulator of virulence gene expression in Vibrio cholerae", *Proceedings of the National Academy of Sciences* **95**, 730 (1998). DOI: 10.1073/pnas.95.2.730.

[88] T. J. Goss, S. J. Morgan, E. L. French, E. S. Krukonis, "ToxR Recognizes a Direct Repeat Element in the toxT, ompU, ompT, and ctxA Promoters of Vibrio cholerae To Regulate Transcription", *Infection and Immunity* **81**, 884 (2013). DOI: 10.1128/IAI.00889-12.

[89] E. Martínez-Hackert, A. M. Stock, "Structural relationships in the OmpR family of winged-helix transcription factors", *Journal of Molecular Biology* **269**, 301 (1997). DOI: 10.1006/jmbi.1997.1065.

[90] L. E. Ulrich, E. V. Koonin, I. B. Zhulin, "One-component systems dominate signal transduction in prokaryotes", *Trends in Microbiology* **13**, 52 (2005).   DOI: 10.1016/j.tim.2004.12.006.

[91] J. S. Parkinson, E. C. Kofoid, "Communication Modules in Bacterial Signaling Proteins", *Annual Review of Genetics* **26**, 71 (1992).   DOI: 10.1146/annurev.ge.26.120192.000443.

[92] B. L. Haas, J. S. Matson, V. J. DiRita, J. S. Biteen, "Imaging live cells at the nanometer-scale with single-molecule microscopy: obstacles and achievements in experiment optimization for microbiology", *Molecules* **19**, 12116 (2014). DOI: 10.3390/molecules190812116.

[93] B. R. Hanson, B. A. Lowe, M. N. Neely, "Membrane topology and DNA-binding ability of the Streptococcal CpsA protein", *Journal of Bacteriology* **193**, 411 (2011). DOI: 10.1128/JB.01098-10.

[94] M. J. Cieslewicz, D. L. Kasper, Y. Wang, M. R. Wessels, "Functional analysis in type Ia group B Streptococcus of a cluster of genes involved in extracellular polysaccharide production by diverse species of streptococci", *The Journal of Biological Chemistry* **276**, 139 (2001). DOI: 10.1074/jbc.M005702200.

[95] S. Gebhard, A. Gaballa, J. D. Helmann, G. M. Cook, "Direct stimulus perception and transcription activation by a membrane-bound DNA binding protein", *Molecular Microbiology* **73**, 482 (2009). DOI: 10.1111/j.1365-2958.2009.06787.x.

[96] R. Matos, V. V. Pinto, M. Ruivo, M. d. F. S. Lopes, "Study on the dissemination of the bcrABDR cluster in Enterococcus spp. reveals that the BcrAB transporter is sufficient to confer high-level bacitracin resistance", *International Journal of Antimicrobial Agents* **34**, 142 (2009). DOI: 10.1016/j.ijantimicag.2009.02.008.

[97] A. B. Blanc-Potard, F. Solomon, J. Kayser, E. A. Groisman, "The SPI-3 pathogenicity island of Salmonella enterica", *Journal of Bacteriology* **181**, 998 (1999). DOI: 10.1128/JB.181.3.998-1004.1999.

[98] C. Tükel, *et al.*, "MarT activates expression of the MisL autotransporter protein of Salmonella enterica serotype Typhimurium", *Journal of Bacteriology* **189**, 3922 (2007). DOI: 10.1128/JB.01746-06.

[99] W.-S. Yeo, *et al.*, "A Membrane-Bound Transcription Factor is Proteolytically Regulated by the AAA+ Protease FtsH in Staphylococcus aureus", *Journal of Bacteriology* **202**, e00019 (2020). DOI: 10.1128/JB.00019-20.

[100] T. P. Hubbard, *et al.*, "Genetic analysis of Vibrio parahaemolyticus intestinal colonization", *Proceedings of the National Academy of Sciences* **113**, 6283 (2016). DOI: 10.1073/pnas.1601718113.

[101] C. Kuper, K. Jung, "CadC-mediated activation of the cadBA promoter in Escherichia coli", *Journal of Molecular Microbiology and Biotechnology* **10**, 26 (2005). DOI: 10.1159/000090346.

[102] A. B. Dalia, D. W. Lazinski, A. Camilli, "Identification of a membrane-bound transcriptional regulator that links chitin and natural competence in Vibrio cholerae", *mBio* **5**, e01028 (2014). DOI: 10.1128/mBio.01028-13.

[103] P. Sobetzko, A. Travers, G. Muskhelishvili, "Gene order and chromosome dynamics coordinate spatiotemporal gene expression during the bacterial growth cycle", *Proceedings of the National Academy of Sciences* **109**, E42 (2012). DOI: 10.1073/pnas.1108229109.

[104] D. F. Browning, D. C. Grainger, S. J. Busby, "Effects of nucleoid-associated proteins on bacterial chromosome structure and gene expression", *Current Opinion in Microbiology* **13**, 773 (2010). DOI: 10.1016/j.mib.2010.09.013.

[105] L. F. Liu, J. C. Wang, "Supercoiling of the DNA template during transcription", *Proceedings of the National Academy of Sciences* **84**, 7024 (1987). DOI: 10.1073/pnas.84.20.7024.

[106] E. W. Harrington, N. J. Trun, "Unfolding of the bacterial nucleoid both in vivo and in vitro as a result of exposure to camphor", *Journal of Bacteriology* **179**, 2435 (1997). DOI: 10.1128/jb.179.7.2435-2439.1997.

[107] C. J. Dorman, "DNA supercoiling and environmental regulation of gene expression in pathogenic bacteria", *Infection and Immunity* **59**, 745 (1991). DOI: 10.1128/iai.59.3.745-749.1991.

[108] A. Badrinarayanan, T. B. K. Le, M. T. Laub, "Bacterial chromosome organization and segregation", *Annual Review of Cell and Developmental Biology* **31**, 171 (2015). DOI: 10.1146/annurev-cellbio-100814-125211.

[109] S. Brameyer, *et al.*, "DNA-binding directs the localization of a membrane-integrated receptor of the ToxR family", *Communications Biology* **2**, 4 (2019). DOI: 10.1038/s42003-018-0248-7.

[110] M. Valens, S. Penaud, M. Rossignol, F. Cornet, F. Boccard, "Macrodomain organization of the Escherichia coli chromosome", *The EMBO journal* **23**, 4330 (2004). DOI: 10.1038/sj.emboj.7600434.

[111] C. Cagliero, R. S. Grand, M. B. Jones, D. J. Jin, J. M. O'Sullivan, "Genome conformation capture reveals that the Escherichia coli chromosome is organized by replication and transcription", *Nucleic Acids Research* **41**, 6058 (2013). DOI: 10.1093/nar/gkt325.

[112] T. B. K. Le, M. V. Imakaev, L. A. Mirny, M. T. Laub, "High-resolution mapping of the spatial organization of a bacterial chromosome", *Science* **342**, 731 (2013). DOI: 10.1126/science.1242059.

[113] "LB Solid or Liquid Medium", *Cold Spring Harbor Protocols* **2016**, pdb.rec088203 (2016). DOI: 10.1101/pdb.rec088203. Publisher: Cold Spring Harbor Laboratory Press.

[114] K. Skorupski, R. K. Taylor, "Positive selection vectors for allelic exchange", *Gene* **169**, 47 (1996). DOI: 10.1016/0378-1119(95)00793-8.

[115] S. M. Amin Marashi, *et al.*, "Determination of ctxAB expression in Vibrio cholerae Classical and El Tor strains using Real-Time PCR", *International Journal of Molecular and Cellular Medicine* **2**, 9 (2013).

[116] T. D. Schmittgen, K. J. Livak, "Analyzing real-time PCR data by the comparative C(T) method", *Nature Protocols* **3**, 1101 (2008). DOI: 10.1038/nprot.2008.73.

[117] Y. Liao, J. W. Schroeder, B. Gao, L. A. Simmons, J. S. Biteen, "Single-molecule motions and interactions in live cells reveal target search dynamics in mismatch repair", *Proceedings of the National Academy of Sciences* **112**, E6898 (2015). DOI: 10.1073/pnas.1507386112.

[118] J. Munkres, "Algorithms for the Assignment and Transportation Problems", *Journal of the Society for Industrial and Applied Mathematics* **5**, 32 (1957). DOI: 10.1137/0105003.

[119] N.-Y. Park, *et al.*, "Multi-Factor Regulation of the Master Modulator LeuO for the Cyclic-(Phe-Pro) Signaling Pathway in Vibrio vulnificus", *Scientific Reports* **9**, 20135 (2019). DOI: 10.1038/s41598-019-56855-4.

[120] X. R. Bina, D. L. Taylor, A. Vikram, V. M. Ante, J. E. Bina, "Vibrio cholerae ToxR downregulates virulence factor production in response to cyclo(Phe-Pro)", *mBio* **4**, e00366 (2013). DOI: 10.1128/mBio.00366-13.

[121] S. Ramadurai, *et al.*, "Lateral diffusion of membrane proteins", *Journal of the American Chemical Society* **131**, 12650 (2009). DOI: 10.1021/ja902853g.

[122] W. P. Teoh, J. S. Matson, V. J. DiRita, "Regulated intramembrane proteolysis of the virulence activator TcpP in Vibrio cholerae is initiated by the tail-specific protease (Tsp)", *Molecular Microbiology* **97**, 822 (2015). DOI: 10.1111/mmi.13069.

[123] J. S. Matson, V. J. DiRita, "Degradation of the membrane-localized virulence activator TcpP by the YaeL protease in Vibrio cholerae", *Proceedings of the National Academy of Sciences* **102**, 16403 (2005). DOI: 10.1073/pnas.0505818102.

[124] N. A. Beck, E. S. Krukonis, V. J. DiRita, "TcpH influences virulence gene expression in Vibrio cholerae by inhibiting degradation of the transcription activator TcpP", *Journal of Bacteriology* **186**, 8309 (2004). DOI: 10.1128/JB.186.24.8309-8316.2004.

[125] A. J. Hay, *et al.*, "Calcium Enhances Bile Salt-Dependent Virulence Activation in Vibrio cholerae", *Infection and Immunity* **85**, e00707 (2017). DOI: 10.1128/IAI.00707-16.

[126] M. Yang, *et al.*, "Bile salt–induced intermolecular disulfide bond formation activates Vibrio cholerae virulence", *Proceedings of the National Academy of Sciences* **110**, 2348 (2013). DOI: 10.1073/pnas.1218039110.

[127] F. Fan, *et al.*, "Enhanced interaction of Vibrio cholerae virulence regulators TcpP and ToxR under oxygen-limiting conditions", *Infection and Immunity* **82**, 1676 (2014). DOI: 10.1128/IAI.01377-13.

[128] M. I. Kazi, A. R. Conrado, A. R. Mey, S. M. Payne, B. W. Davies, "ToxR Antagonizes H-NS Regulation of Horizontally Acquired Genes to Drive Host Colonization", *PLoS pathogens* **12**, e1005570 (2016). DOI: 10.1371/journal.ppat.1005570.

[129] D. Lucena, M. Mauri, F. Schmidt, B. Eckhardt, P. L. Graumann, "Microdomain formation is a general property of bacterial membrane proteins and induces heterogeneity of diffusion patterns", *BMC biology* **16**, 97 (2018). DOI: 10.1186/s12915-018-0561-0.

[130] J. H. Lorent, *et al.*, "Author Correction: Structural determinants and functional consequences of protein affinity for membrane rafts", *Nature Communications* **9**, 1805 (2018). DOI: 10.1038/s41467-018-04164-1.

[131] J. Bina, *et al.*, "ToxR regulon of Vibrio cholerae and its expression in vibrios shed by cholera patients", *Proceedings of the National Academy of Sciences* **100**, 2801 (2003). DOI: 10.1073/pnas.2628026100.

[132] Z.-W. Lee, *et al.*, "Small-molecule inhibitor of HlyU attenuates virulence of Vibrio species", *Scientific Reports* **9**, 4346 (2019). DOI: 10.1038/s41598-019-39554-y.

[133] D. Ganesan, S. S. Gupta, D. Legros, "Cholera surveillance and estimation of burden of cholera", *Vaccine* **38**, A13 (2020). DOI: 10.1016/j.vaccine.2019.07.036.

[134] J. G. Conner, J. K. Teschler, C. J. Jones, F. H. Yildiz, "Staying alive: Vibrio cholerae's cycle of environmental survival, transmission, and dissemination", *Microbiology spectrum* **4**, 4.2.02 (2016). DOI: 10.1128/microbiolspec.VMBF-0015-2015.

[135] S. Thomas, S. G. Williams, P. A. Manning, "Regulation of tcp genes in classical and E1 Tor strains of Vibrio cholerae O1", *Gene* **166**, 43 (1995). DOI: 10.1016/0378-1119(95)00610-X.

[136] C. Lutz, M. Erken, P. Noorian, S. Sun, D. McDougald, "Environmental reservoirs and mechanisms of persistence of Vibrio cholerae", *Frontiers in Microbiology* **4**, 375 (2013). DOI: 10.3389/fmicb.2013.00375.

[137] S. M. Faruque, M. J. Albert, J. J. Mekalanos, "Epidemiology, Genetics, and Ecology of Toxigenic Vibrio cholerae", *Microbiology and Molecular Biology Reviews* **62**, 1301 (1998). DOI: 10.1128/MMBR.62.4.1301-1314.1998.

[138] Z. Chen, L. Geffroy, J. S. Biteen, "NOBIAS: Analyzing Anomalous Diffusion in Single-Molecule Tracks With Nonparametric Bayesian Inference", *Frontiers in Bioinformatics* **1**, 742073 (2021). DOI: 10.3389/fbinf.2021.742073.

[139] J. Yu, J. Xiao, X. Ren, K. Lao, X. S. Xie, "Probing Gene Expression in Live Cells, One Protein Molecule at a Time", *Science* **311**, 1600 (2006). DOI: 10.1126/science.1119623.

[140] M. Shamir, Y. Bar-On, R. Phillips, R. Milo, "SnapShot: Timescales in Cell Biology", *Cell* **164**, 1302 (2016). DOI: 10.1016/j.cell.2016.02.058.

[141] A. S. Meyer, D. C. Grainger, *Advances in Applied Microbiology*, S. Sariaslani, G. M. Gadd, eds. (Academic Press, 2013), vol. 83, pp. 69–86.

[142] R. Grant, D. Filman, S. Finkel, R. Kolter, J. Hogle, "The crystal structure of Dps, a ferritin homolog that binds and protects DNA | Nature Structural & Molecular Biology", *Nature Structural Biology* **5**, 294 (1988). DOI: nsb0498-294.

[143] M. Almirón, A. J. Link, D. Furlong, R. Kolter, "A novel DNA-binding protein with regulatory and protective roles in starved Escherichia coli.", *Genes & Development* **6**, 2646 (1992). DOI: 10.1101/gad.6.12b.2646.

[144] T. A. Azam, A. Ishihama, "Twelve Species of the Nucleoid-associated Protein from Escherichia coli: Sequence recognition specificty and DNA binding affinity", *Journal of Biological Chemistry* **274**, 33105 (1999). DOI: 10.1074/jbc.274.46.33105.

[145] T. Ali Azam, A. Iwata, A. Nishimura, S. Ueda, A. Ishihama, "Growth Phase-Dependent Variation in Protein Composition of the Escherichia coli Nucleoid", *Journal of Bacteriology* **181**, 6361 (1999).

[146] R. Janissen, *et al.*, "Global DNA Compaction in Stationary-Phase Bacteria Does Not Affect Transcription", *Cell* **174**, 1188 (2018). DOI: 10.1016/j.cell.2018.06.049.

[147] R. Hengge-Aronis, "Signal Transduction and Regulatory Mechanisms Involved in Control of the σS (RpoS) Subunit of RNA Polymerase", *Microbiology and Molecular Biology Reviews* **66**, 373 (2002). DOI: 10.1128/MMBR.66.3.373-395.2002.

[148] A. Battesti, N. Majdalani, S. Gottesman, "The RpoS-Mediated General Stress Response in Escherichia coli", *Annual Review of Microbiology* **65**, 189 (2011). DOI: 10.1146/annurev-micro-090110-102946.

[149] S. Korshunov, J. A. Imlay, "Two sources of endogenous hydrogen peroxide in Escherichia coli", *Molecular Microbiology* **75**, 1389 (2010). DOI: 10.1111/j.1365-2958.2010.07059.x.

[150] J. A. Imlay, "The molecular mechanisms and physiological consequences of oxidative stress: lessons from a model bacterium", *Nature Reviews Microbiology* **11**, 443 (2013). DOI: 10.1038/nrmicro3032. Number: 7 Publisher: Nature Publishing Group.

[151] J. A. Imlay, "Cellular Defenses against Superoxide and Hydrogen Peroxide", *Annual Review of Biochemistry* **77**, 755 (2008). DOI: 10.1146/annurev.biochem.77.061606.161055.

[152] X. He, *et al.*, "Oral-Derived Bacterial Flora Defends Its Domain by Recognizing and Killing Intruders—A Molecular Analysis Using Escherichia coli as a Model Intestinal Bacterium", *Microbial Ecology* **60**, 655 (2010). DOI: 10.1007/s00248-010-9708-4.

[153] A. Martinez, R. Kolter, "Protection of DNA during oxidative stress by the nonspecific DNA-binding protein Dps", *Journal of Bacteriology* **179**, 5188 (1997). DOI: 10.1128/jb.179.16.5188-5194.1997.

[154] G. Zhao, *et al.*, "Iron and Hydrogen Peroxide Detoxification Properties of DNA-binding Protein from Starved Cells. A ferritin-like DNA-binding protein of Escherichia coli.", *Journal of Biological Chemistry* **277**, 27689 (2002). DOI: 10.1074/jbc.M202094200.

[155] S. Altuvia, M. Almiron, G. Huisman, R. Kolter, G. Storz, "The dps promoter is activated by OxyR during growth and by IHF and σs in stationary phase", *Molecular Microbiology* **13**, 265 (1994). DOI: 10.1111/j.1365-2958.1994.tb00421.x.

[156] D. C. Grainger, M. D. Goldberg, D. J. Lee, S. J. W. Busby, "Selective repression by Fis and H-NS at the Escherichia coli dps promoter", *Molecular Microbiology* **68**, 1366 (2008). DOI: 10.1111/j.1365-2958.2008.06253.x.

[157] K. Yamamoto, A. Ishihama, S. J. W. Busby, D. C. Grainger, "The Escherichia coli K-12 MntR Miniregulon Includes dps, Which Encodes the Major Stationary-Phase DNA-Binding Protein", *Journal of Bacteriology* **193**, 1477 (2011). DOI: 10.1128/JB.01230-10.

[158] M. De Martino, D. Ershov, P. J. van den Berg, S. J. Tans, A. S. Meyer, "Single-Cell Analysis of the Dps Response to Oxidative Stress", *Journal of Bacteriology* **198**, 1662 (2016). DOI: 10.1128/JB.00239-16.

[159] C. Stringer, T. Wang, M. Michaelos, M. Pachitariu, "Cellpose: a generalist algorithm for cellular segmentation", *Nature Methods* **18**, 100 (2021). DOI: 10.1038/s41592-020-01018-x.

[160] R. L. Ohniwa, *et al.*, "Dynamic state of DNA topology is essential for genome condensation in bacteria", *The EMBO Journal* **25**, 5591 (2006). DOI: 10.1038/sj.emboj.7601414.

[161] L. Jiang, N. S. Korivi, *Nanolithography*, M. Feldman, ed. (Woodhead Publishing, 2014), pp. 424–443.

[162] U. Endesfelder, "From single bacterial cell imaging towards *in vivo* single-molecule biochemistry studies", *Essays In Biochemistry* **63**, 187 (2019). DOI: 10.1042/EBC20190002.

[163] J. Zhang, M. Zhang, Y. Wang, E. Donarski, A. Gahlmann, "Optically Accessible Microfluidic Flow Channels for Noninvasive High-Resolution Biofilm Imaging Using Lattice Light Sheet Microscopy", *The Journal of Physical Chemistry B* **125**, 12187 (2021). DOI: 10.1021/acs.jpcb.1c07759.

[164] S. Iyer-Biswas, *et al.*, "Scaling laws governing stochastic growth and division of single bacterial cells", *Proceedings of the National Academy of Sciences* **111**, 15912 (2014). DOI: 10.1073/pnas.1403232111.

[165] J. Y. Ryu, *et al.*, "Profiling protein–protein interactions of single cancer cells with in situ lysis and co-immunoprecipitation", *Lab on a Chip* **19**, 1922 (2019). DOI: 10.1039/C9LC00139E.

[166] R. J. Kimmerling, *et al.*, "A microfluidic platform enabling single-cell RNA-seq of multigenerational lineages", *Nature Communications* **7**, 10220 (2016). DOI: 10.1038/ncomms10220.

[167] N. Q. Balaban, J. Merrin, R. Chait, L. Kowalik, S. Leibler, "Bacterial Persistence as a Phenotypic Switch", *Science* **305**, 1622 (2004). DOI: 10.1126/science.1099390.

[168] J. Stricker, *et al.*, "A fast, robust, and tunable synthetic gene oscillator", *Nature* **456**, 516 (2008). DOI: 10.1038/nature07389.

[169] J. Ryley, O. M. Pereira-Smith, "Microfluidics device for single cell gene expression analysis in Saccharomyces cerevisiae", *Yeast* **23**, 1065 (2006). DOI: 10.1002/yea.1412.

[170] Y. Bey, "Notes for Troubleshooting Alignments", *U.C. Davis Research Engineering* pp. 1–11 (2014).

[171] J. Hanke, C. Ranke, E. Perego, S. Köster, "Human blood platelets contract in perpendicular direction to shear flow", *Soft Matter* **15**, 2009 (2019). DOI: 10.1039/C8SM02136H.

[172] Y. Taniguchi, *et al.*, "Quantifying E. coli proteome and transcriptome with single-molecule sensitivity in single cells", *Science* **329**, 533 (2010). DOI: 10.1126/science.1188308.